

Aus dem Max-Planck-Institut für Kolloid- und Grenzflächenforschung
Abteilung Grenzflächen, Arbeitsgruppe: PD Dr. Hans Riegler
und
International Max Planck Research School on Biomimetic Systems

**Transport mechanisms and wetting dynamics in
molecularly thin films of long-chain alkanes at solid/vapour
interface: relation to the solid-liquid phase transition**

Dissertation

zur Erlangung des akademischen Grades

Doktor der Naturwissenschaften

”doctor rerum naturalium”

(Dr. rer. nat.)

in der Wissenschaftsdisziplin Experimentalphysik

eingereicht an der

Mathematisch-Naturwissenschaftlichen Fakultät

der Universität Potsdam

von

Paul Lazăr

geboren am 17.09.1972 in Focşani-Vrancea, Rumänien

Potsdam, Februar 2005

To my sisters, Veronica and Gabriela

Surorilor mele, Veronica și Gabriela

Contents

1. Introduction	5
2. Theoretical background	7
2.1. Interfacial thermodynamics	7
2.1.1. Interfacial and surface energies	7
2.1.2. Statics of wetting, Young equation	7
2.1.3. Work of adhesion and cohesion	9
2.1.4. Laplace equation	9
2.1.5. Molecular and surface forces	10
2.1.6. Thin films and disjoining pressure	12
2.2. Wetting dynamics	14
2.2.1. Models describing the wetting dynamics	15
2.2.2. The hydrodynamic model	15
2.2.3. The molecular-kinetic model	18
2.2.4. Precursor films	19
2.3. Running Droplets	22
2.3.1. Passive drops on a chemically heterogeneous solid surface	22
2.3.2. Reactive wetting	23
2.3.3. Velocity of running drops	23
2.4. Physico-chemical properties of n-alkanes	26
2.4.1. Bulk, crystalline n-alkane structures at low temperatures	27
2.4.2. Bulk structural behaviour in the vicinity of the melting point	27
2.4.3. Interfacial behaviour, surface freezing	28
2.5. Theory of melting	30
2.5.1. Bulk melting mechanisms, surface premelting	30
2.5.2. Influence of size, dimensionality and confinement on the melting temperature	31
2.6. Classical nucleation theory, crystallization from melt	33
2.6.1. Homogeneous nucleation	33
2.6.2. Heterogeneous nucleation	35
3. Experimental methods and equipment	39
3.1. Specular X-ray reflectometry	39
3.1.1. Basic concepts	39
3.1.2. Kiessig fringes and Bragg peaks	40
3.2. Atomic force microscopy	41
3.3. Optical microscopy	42

4. Materials and sample preparation	47
4.0.1. Alkanes and substrates	47
5. Droplet solidification by growing molecularly thin terraces	49
5.1. Introduction	49
5.2. Nucleation of bulk solidification and terrace growth	51
5.3. Structure and thickness of the growing film	54
5.3.1. Optical microscopy and AFM	54
5.3.2. Small-angle X-ray reflectivity data	54
5.4. Equations describing the kinetics of terrace growth	58
5.5. Kinetics of sequential growth of monomolecular terraces at constant temperature	60
5.5.1. Growth of the second terrace on top of the first one	60
5.5.2. Kinetics of growth for first, second, and third monomolecular layer	62
5.6. Influence of temperature on the terrace growth kinetics	63
5.7. Behaviour of the solidified "drops"	63
5.8. Monolayer growth from a solid on the bare silicon substrate	65
5.9. Terrace behaviour above bulk melting point	68
5.10. Discussion and conclusions	69
6. Reversible running drops driven by the S-L phase transition	73
6.1. Introduction	73
6.2. Nucleation of the advancing running droplets	73
6.2.1. Instability of the wetting stripe at the terrace edge	75
6.2.2. Critical radius and free energy barrier	76
6.3. Kinetics of running droplets on melting	77
6.3.1. Dynamic contact angle of running droplets	80
6.3.2. Dependence of velocity on droplet size	82
6.3.3. Dependence of velocity on temperature and number of molecular layers	83
6.3.4. Generalized dependence of velocity versus terrace thickness and overheating	86
6.3.5. Driving force: Surface tension or melting free energy?	87
6.3.6. Calculation of the temperature slope of the driving force using the hydrodynamic model	91
6.3.7. Dewetting Kinetics of the all-liquid film	91
6.4. Running droplets driven by solidification	93
6.4.1. Temperature dependence of the velocity for solidification-driven running drops	93
6.4.2. Sequential initiation of solidifying running droplets	95
6.4.3. Mechanism of solidification-driven running drops when thin solid terraces are formed	95
6.5. Discussion and conclusions	98
7. Overheating aspects of solid alkane films of different thickness	101
7.1. Introduction	101
7.2. Thermodynamic considerations for melting of a monolayer thick solid terrace	102
7.2.1. The (absolute) thermodynamic limit of overheating, T^{MN}	106
7.2.2. Hierarchy of the melting mechanisms	106

7.3. Overheating of thick terraces	108
7.4. Conclusions	114
8. Conclusions	115
Bibliography	117
A. Appendix	iii
A.1. Definitions	iii
A.1.1. Useful relations between different parameters describing spherical-cap shaped drops	iii
A.2. Fresnel reflectivity	v
A.3. Home-made equipment, special set-up	viii
A.4. Mechanism-dependent equations describing the growth kinetics of a thin solid film	x
A.4.1. Release-limited, constant mass flux per unit length of contact line	x
A.4.2. Growth-limited, constant rate of solidification at the edge	xi
A.4.3. Transport-limited, "diffusion-like" transport	xi
A.5. Free energy gain upon spontaneous dewetting	xiv
A.6. Instability of a droplet wetting the step region	xvi
B. Acknowledgments	xix

1. Introduction

Surfaces and interfaces can be found everywhere around us. In the last decades, surface science and technology is subject of increasing interest due to the general trend of miniaturization. Many modern applications require a good control of the way small amounts of liquid are transported. Liquids in micro- or nanochannels must be pumped, distributed, mixed or forced to flow in jets (printing) in a controlled way. For the scale at which these processes occur, the classical methods of handling liquids (e.g. mechanical pumps or electrical valves) are either ineffective or it is technologically difficult to manufacture such microdevices.

In biological systems, many important processes occur at surfaces of cells and membranes. One may say that life itself developed in the early stages, and still develops at surfaces and interfaces. The interactions at interfaces are important when, for instance, viruses attach themselves to the surfaces of the cell. The properties of skin or leaf surfaces are also of tremendous importance; they represent a defense system whose properties preserve the integrity of the whole system. Hence, two-dimensional systems are essential for understanding the behaviour of biological interfaces.

Wetting and spreading phenomena have recently been the subject of renewed interest, both for fundamental science and technology. Processes like painting, coating, glueing, lithographic printing, lubrication, and many others cannot be understand and controlled without a good knowledge of the underlying conditions and laws which govern them.

Long chain alkanes are the basic units for more complex organic molecules like surfactants, liquid crystals, polymers and lipids. The properties of these molecules cannot be properly understood without a knowledge of those of the alkanes.

Molecularly thin coverages of long-chain alkanes (tetracosane, triacontane and hexatriacontane) on solid surfaces are excellently suited to study wetting, two-dimensional ordering and molecular transport phenomena at the planar solid-vapour interface. The phase behaviour is rich and complex.

In chapter 2 of this thesis, are presented some of the basic concepts of surface thermodynamics, molecular interactions, statics and dynamics of wetting, classical nucleation theory, and theory of melting. The basic bulk and surface properties of alkanes are presented in the same chapter.

In chapter 3, the theoretical aspects of the experimental methods used in this work (SAXR, AFM, and optical microscopy) are shortly presented. Chapter 4 describes the materials and sample preparation.

After a short description of the wetting properties of long-chain alkanes above and below their melting temperature, chapter 5 describes a two-dimensional mechanism of solidification (terrace growth). Undercooled (few degrees below the melting temperature, T_{mp}), partially wetting alkane drops can either solidify in bulk or start growing terraces on the silicon substrate. This is a nucleated process and drop-to-drop propagation of the solidification front can be observed. The kinetics of growth is "diffusive", i.e. $R \propto \sqrt{time}$. By analyzing the growth behaviour, the presence of a molecularly thin, "liquid-like" film on top of the solid terraces is deduced. An unexpected temperature dependence of the growth kinetic is found: below T_{mp} the "speed" of terrace growth decreases with increasing

temperature, at T_{mp} the growth stops, and slightly above T_{mp} the process is reversed ("terrace dissolution"). A model is proposed to explain the experimental findings.

Besides the "terrace dissolution" mechanism of melting, at higher overheating temperatures (up to $\approx 1^\circ\text{C}$ above T_{mp}), solid terraces can melt via "running" drops. This second mechanism is presented and discussed in chapter 6. Tiny drops (sub-micrometer in size) nucleate at the terrace edges and move subsequently on the surface "eating" the solid in their way. The direction of movement can be reversed, i.e. the drop moves solidifying at temperature below T_{mp} . The influence of temperature, chain length and droplet size on the drops velocity is analyzed in detail and two scenarios are considered in order to explain the observations.

Defining a proper thermodynamic potential which takes into account both *surface* and *bulk* energetical contributions, a theoretical analysis explains qualitatively and quantitatively the overheating aspects of melting/solidification for both "running" drops and terrace growth presented in chapters 5 and 6. It also predicts a third mechanism of melting, when melting "propagates" faster than all-liquid dewetting. This phenomenological approach is based only on experimentally accessible parameters (molar entropy of fusion, liquid surface tension, contact angle, etc.). In the second part of chapter 7, data related to the melting/solidification of thick terraces are presented and discussed.

2. Theoretical background

This chapter describes the fundamental concepts for understanding the behaviour of solid and liquid long-chain alkane molecules at planar solid-air interfaces. Statics and dynamics of wetting, transport phenomena, adsorption and ordering of molecules at interfaces can not be properly described without taking into account the forces acting at the microscopic scale.

2.1. Interfacial thermodynamics

2.1.1. Interfacial and surface energies

An interface is the zone separating two immiscible, condensed phases (L/S, L/L or S/S). If one of the phases is a gas, the limiting region is called surface. The interface (surface) region has a finite thickness (usually less than $0.1\mu\text{m}$) and composition and energy vary continuously from one phase to the other. Unlike in the bulk, the pressure (force field) in the interfacial zone is nonhomogeneous, having a gradient perpendicular to the interface. A consequence of this is that a net energy is required to create an interface by the reversible transport of matter from the bulk to the interfacial zone. The reversible work needed to create a unit interface (surface) area is the interfacial (surface) tension, γ :

$$\gamma \equiv \left(\frac{\partial G}{\partial A} \right)_{T, p, n} \quad (2.1)$$

where G is the total Gibbs free energy, A the interfacial area, T temperature, p pressure, and n the total number of moles of matter in the system. The term surface tension (force per unit length) is frequently used for liquids. It is numerically and dimensionally the same as surface energy (energy per unit area), the term commonly used for solids.

The surface entropy per unit area is given by the change in the surface tension with temperature [1]

$$s^\sigma \equiv \frac{S^\sigma}{A} = - \left(\frac{\partial \gamma}{\partial T} \right)_{p, A} \quad (2.2)$$

2.1.2. Statics of wetting, Young equation

When a small liquid droplet is put in contact with a flat solid surface, two distinct equilibrium configurations may be found (see figure 2.1 a, b): partial wetting, with a finite contact angle θ_e , and complete wetting for $\theta_e = 0$ (uniform liquid film). Brochard et al. [2] describe a third situation, a finite contact angle droplet in contact with a thin uniform liquid film, (2.1, c). In the case of partial wetting, the wetted portion of the surface is delimited by a certain contact line, where the three phases are in contact. Macroscopically, the angle between planes tangent to the L/V and S/V interfaces at the wetting line is defined as contact angle, θ_e . At microscopic (molecular) scale, the structure of the

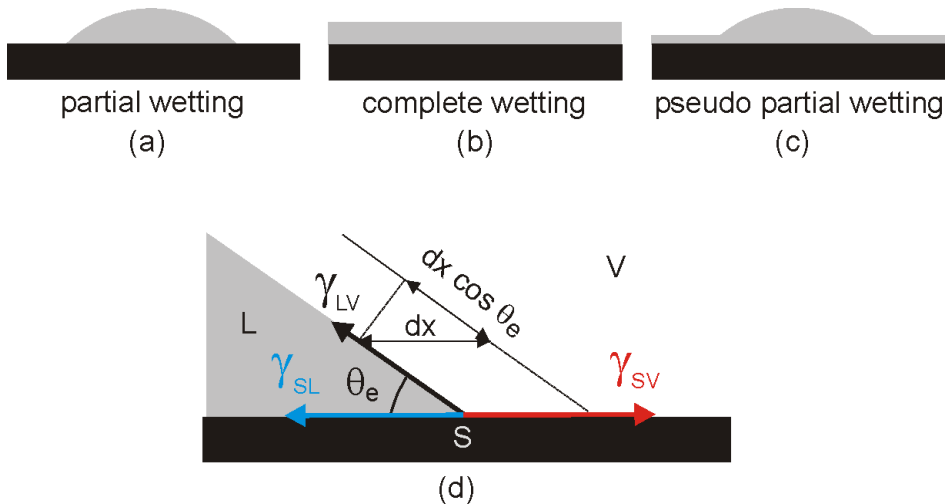


Figure 2.1. The three possible wetting regimes (a, b, and c), and the forces acting at the three phase contact line (d). The energy balance upon shifting the line position with dx gives the Young equation.

contact line region is much more complex. However, it is possible to relate θ_e to the far-field interfacial energies γ_{ij} without any knowledge of the molecular scale structure. In equilibrium, the energy must not change with respect to any shift dx of the line position. A horizontal shift dx generates, per unit length, the following interfacial area variations: $-dx$ for S/V , $+dx$ for S/L and $+\cos\theta_e dx$ for L/V . Setting to zero the sum of the three contributions one obtains the Young equation:

$$\gamma_{SV} = \gamma_{SL} + \gamma_{LV} \cos \theta_e \quad (2.3)$$

Determination of the thermodynamic contact angle requires very clean experimental conditions. In many practical situations the three phase contact line is pinned and immobile within a finite interval around θ_e ,

$$\theta_r < \theta_e < \theta_a \quad (2.4)$$

The angle θ_a (advancing angle) is measured when the solid/liquid contact area increases, while θ_r (receding angle) is measured when the contact area shrinks. The hysteresis value, $H \equiv \theta_a - \theta_r$, may be 10° or more for surfaces without special preparation but may be less than 1° for carefully prepared surfaces. The causes of this hysteresis are surface roughness, chemical contaminations or inhomogeneities of the solid surface, and solutes in the liquid which may deposit a film on the solid, altering the initial values of surface energies. The complete wetting situation corresponds to $\cos\theta_e = 1$ and $\gamma_{SV} - \gamma_{SL} = \gamma_{LV}$. At first sight, this situation appears rather exceptional. In fact, it is not, because in thermodynamic equilibrium $\gamma_{SV} - \gamma_{SL} - \gamma_{LV}$ can never be positive. If it were so, the free energy of a solid/vapour interface could be lowered by intercalating a liquid film of macroscopic thickness. In most practical applications the system is not in perfect thermodynamic equilibrium and we may have a solid/vapour interfacial energy γ_{S0} which is larger than $\gamma_{SL} + \gamma_{LV}$. The difference

$$S_i \equiv \gamma_{S0} - \gamma_{SL} - \gamma_{LV} \quad (2.5)$$

is called the initial spreading coefficient. Physically, γ_{S0} is associated with a "dry" solid surface, while γ_{SV} is associated with a "moist" surface. S_i can be positive indicating a free energy gain upon

spreading of the liquid onto the surface. In a similar way, one defines the equilibrium spreading coefficient,

$$S_e \equiv \gamma_{SV} - \gamma_{SL} - \gamma_{LV} \quad (2.6)$$

which is always negative. Adsorption of vapor on a bare solid substrate generally occurs if it leads to the decrease of the free energy of the system. This will happen when the condensed vapor has a surface tension similar or lower than that of the substrate. The equilibrium spreading pressure is defined as

$$\pi_e \equiv \gamma_{S0} - \gamma_{SV} = S_i - S_e \quad (2.7)$$

and can be measured by vapor adsorption,

$$\pi_e = \int_0^{p_0} \Gamma d\mu = RT \int_0^{p_0} \Gamma d(\ln p) \quad (2.8)$$

where p_0 is the saturated vapor pressure, Γ the number of moles of vapor adsorbed per unit area of the substrate, μ the chemical potential of the vapor and p the vapor pressure.

2.1.3. Work of adhesion and cohesion

Historically, the next development after Young was due to Dupré. He introduced the concepts of work of adhesion and cohesion. The work required to separate reversibly the interface between two bulk phases i and j from their equilibrium separation to infinity is the work of adhesion,

$$W_{adh} = \gamma_i + \gamma_j - \gamma_{ij} \quad (2.9)$$

When the two phases are identical, the reversible work is called the work of cohesion,

$$W_{coh} = 2\gamma_i \quad (2.10)$$

Combining the Young equation 2.3 with equation 2.9 we obtain the Young-Dupré equation

$$W_{adh}^{SL} = \gamma_{LV}(1 + \cos \theta_e) \quad (2.11)$$

2.1.4. Laplace equation

The Laplace equation governs the shape of all macroscopic liquid interfaces, drops, and bubbles and is the basis for all static measurements of interfacial and surface tensions. The pressure change across a curved interface, Δp , is balanced by the capillary force, giving

$$\Delta p = p_i - p_j = \gamma_{ij} \left(\frac{1}{R_1} + \frac{1}{R_2} \right) \quad (2.12)$$

where p_i , p_j are the pressures in the two phases, and R_1 and R_2 are the two principal radii of curvature. An important implication of the above equation is that for a static situation (no flow) and absence of external fields (e.g. gravity), the pressure is the same everywhere in the liquid and thus the interface (surface) has the same curvature everywhere.

2.1.5. Molecular and surface forces

Intermolecular forces can be classified roughly into three categories [3]. Purely electrostatic forces arising from the Coulomb force between charges form the first class. These forces act between charges, permanent dipoles or quadrupoles (charge–charge, charge–permanent dipole, two permanent dipoles). In the second category there are polarization forces arising from the dipole moments induced in atoms or molecules by the electric field of nearby charges and permanent dipoles. The third category are forces which are quantum mechanical in nature giving rise to covalent, chemical bonding and to the repulsive steric (exchange) interactions which are short range and balance the attractive forces at very short distances. Three types of forces described by the same power law variation with distance ($F \propto r^{-7}$) are usually denoted as van der Waals forces. They correspond to the interactions between two freely rotating dipoles, a freely rotating dipole and a non-polar molecule, and two non-polar molecules. Since our system does not contain charges, the main interactions considered are long range attractive van der Waals interaction and short range repulsive, steric interaction.

Van der Waals interactions

Three different types of forces contribute to the total long-range interaction between polar molecules, collectively known as the van der Waals force: induction (Debye), orientation (Keesom) and dispersion (London) force, each of which having an interaction Helmholtz free energy that varies with the inverse sixth power of the distance

$$W(r) = -\frac{C_{VDW}}{r^6} = -\frac{C_{ind} + C_{orient} + C_{disp}}{r^6} \quad (2.13)$$

The first contribution, corresponding to the interaction between a freely rotating dipole and a polarizable molecule (Debye, dipole–induced dipole interaction) is given by the equation

$$W(r) = -\frac{C_{ind}}{r^6} = -\frac{\mu^2 \alpha}{(4\pi\epsilon_0)^2 r^6} \quad (2.14)$$

where μ is the dipole moment, α the polarizability ($\mu_{ind} = \alpha E$), and ϵ_0 the vacuum dielectric constant.

The Keesom interaction, acting between two freely rotating permanent dipoles is described by

$$W(r) = -\frac{C_{orient}}{r^6} = -\frac{\mu_1^2 \mu_2^2}{3(4\pi\epsilon_0)^2 k_B T r^6} \quad (2.15)$$

where k_B is the Boltzmann constant and T the absolute temperature.

Even for polar molecules (except small highly polar molecules, e.g. water), the most important part of van der Waals forces are the London forces, known also as induced-dipole–induced-dipole or dispersion forces. They are always present because they do not request any special property of interacting atoms or molecules. For an atom, the origin of the dispersion force can be understood by considering the circulation of electrons with high frequencies of typically 10^{15} – 10^{16} Hz around the positively charged nucleus. This movement leads to the random, spontaneous formation of temporary dipoles. When two such oscillators approach each other, they start to influence each other. Attractive orientations have higher probabilities than repulsive ones, giving rise to an attractive force. If the ionization energies of the two molecules are $h\nu_1$ and $h\nu_2$, the interaction energy is given by

$$W(r) = -\frac{C_{disp}}{r^6} = -\frac{3h\nu_1\nu_2}{2(\nu_1 + \nu_2)} \frac{\alpha_1\alpha_2}{(4\pi\epsilon_0)^2 r^6} \quad (2.16)$$

The dispersion interaction can be described as follows: the electric field, generated by the spontaneous formation of a molecular dipole, travels with the speed of light (c) the distance r to polarize a second molecule. In turn, the electric field from the induced dipole moment in the second molecule needs the same time, $\Delta t = r/c$ to reach the first molecule. The equation 2.16 is valid under the assumption that the electric field has enough time to cover the distance r between the molecules before the dipole moment has changed. The time during which the dipole moment changes is in the order of $1/\nu$. The relevant frequencies ν are those corresponding to the ionization of the molecule (3×10^{15} Hz). Hence, if $D > c/\nu \approx 10\text{nm}$, the interacting electric field is "retarded" and the energy decreases more steeply with distance (i.e. $W(r) \propto 1/r^7$ for molecules).

Short range repulsive interaction

At very small interatomic distances the electron clouds of the atoms overlap generating a strong repulsive force. These forces are called steric or hard core repulsion and they are characterized by having very short range, increasing sharply with decreasing distance. There is no general equation for describing their distance dependence, and empirical potentials are considered. The three most commonly used potentials are the hard sphere potential, the inverse power-law potential, and the exponential potential. The equation

$$W(r) = + \left(\frac{\sigma}{r} \right)^n \quad (2.17)$$

where $\sigma/2$ is the molecular radius, describes the hard sphere potential for $n = \infty$ and the power-law potential for n being a finite integer, usually taken between 9 and 16. The exponential potential is $W(r) = ce^{-r/\sigma_0}$, where c and σ_0 are adjustable constants. A total intermolecular pair potential is obtained by summing the attractive and repulsive potentials. The best known of these is the *Lennard-Jones* ("6-12") potential, widely used for its simplicity:

$$W(r) = + \frac{A}{r^{12}} - \frac{B}{r^6} \quad (2.18)$$

where A and B are constants.

The van der Waals force between macroscopic bodies

Under the assumption that the van der Waals interactions are additive and non-retarded, one can calculate the vdW interaction energy between two macroscopic bodies with different geometry by integration of the interaction energy between all molecules which form the two bodies. For two semi-infinite planar bodies separated by the distance h in vacuum, made of molecules 1 and 2 respectively, integration of the 1-2 pair interaction energy $W(r) = -C_{12}/h^6$ gives,

$$W(r) = - \frac{\pi C_{12} \rho_1 \rho_2}{12h^2} = - \frac{A_H}{12\pi h^2} \quad (2.19)$$

where $A_H = \pi^2 C_{12} \rho_1 \rho_2$ is the so-called Hamaker constant, with ρ_1, ρ_2 being the number densities of molecules A and B in the two bodies [1, 3]. The Hamaker constant has typical values in the range of 10^{-19} to 10^{-20} J.

The assumption of simple pairwise additivity ignores the interfering influence of neighbouring molecules. In condensed media this influence can be important. Lifshitz theory avoids this problem

by ignoring the molecular structure and treating large bodies as continuous media, which are characterized by their bulk properties like dielectric constants and refractive indices. This leads to the same expressions as the simple 1-2 pair interaction approach, in particular the distance dependence turns out to be the same. Only the Hamaker constant is calculated in a different way. We need to know how the dielectric permittivity of the media varies with frequency. In the case of two bodies 1 and 2 interacting in a medium 3, under the assumption that all the three media have the same absorption frequencies, ν_e (typically around 3×10^{15} Hz), the Hamaker constant has the approximate expression

$$A_H = A_{132}(\varepsilon_i, n_i) \approx \frac{3k_B T}{4} \left(\frac{\varepsilon_1 - \varepsilon_3}{\varepsilon_1 + \varepsilon_3} \right) \left(\frac{\varepsilon_2 - \varepsilon_3}{\varepsilon_2 + \varepsilon_3} \right) + \frac{3h\nu_e}{8\sqrt{2}} \frac{(n_1^2 - n_3^2)(n_2^2 - n_3^2)}{\sqrt{(n_1^2 + n_3^2)(n_2^2 + n_3^2)} \left(\sqrt{n_1^2 + n_3^2} + \sqrt{n_2^2 + n_3^2} \right)} \quad (2.20)$$

where ε_1 , ε_2 and ε_3 are the static dielectric constants of the three media, and n_1 , n_2 and n_3 are the corresponding refractive indices, respectively. Equation 2.20 allows not only to calculate the Hamaker constant but also to predict whether the interaction is attractive (A_H positive) or repulsive (A_H negative). Van der Waals forces between identical materials are always attractive, irrespective of the nature of the intervening material ($A_{iji} > 0$). The same is valid if the medium 3 is vacuum. A repulsive¹ interaction arises whenever the dielectric properties of the intervening medium are intermediate between those of the two interacting media.

2.1.6. Thin films and disjoining pressure

In terms of interfacial energies, a thick film ($h > 100$ nm) on a solid substrate is described by considering only the two interfacial energies γ_{SL} and γ_{LV} . This is not correct anymore when the film becomes very thin ($h \rightarrow 0$), and we must recover the energy of the bare solid, γ_{S0} . For a correct description of a thin film, an additional energetical contribution (per unit area), $P(h)$, must be added

$$f(h) = \frac{F}{A} = \gamma_{SL} + \gamma_{LV} + P(h) \quad (2.21)$$

where $f(h)$ is the free energy of the film per unit area. The correction term $P(h)$ shall be 0 for very thick films, $P(\infty) = 0$. For the bare substrate it is per definition $P(0) = S_i = \gamma_{S0} - \gamma_{SL} - \gamma_{LV}$. The function $P(h)$ may contain different types of contributions like steric effects ($h \approx a$, where a is the size of the liquid molecule), long range van der Waals interactions, electrostatic interactions (charged interfaces) and hydrogen bonds.

Since for thin films $P(h)$ changes with the thickness, it is possible to relate this variation to the reversible work of a force per unit area, which is a pressure. This pressure, usually denoted by Π , is called "disjoining pressure",

$$\Pi = - \frac{dP(h)}{dh} \quad (2.22)$$

It was introduced in 1936 by Derjaguin [4], who defined it as the difference between the hydrostatic pressure in the film and the pressure in the bulk phase from which the film was formed.

¹Strictly speaking, the interaction is not repulsive, rather are the interactions between 1 and 3 and 2 and 3 more attractive than (the attractive) interaction between 1 and 2.

Overall stress in a film

When the spreading coefficient is positive, we expect that a non volatile droplet will spread on a solid surface. If the amount of liquid is limited to the initial volume of the droplet and the available surface area is large enough, the final (equilibrium) state should take into account the energetic contribution of the long range forces for the resulting very thin film. Constant liquid volume means that

$$d\Omega = d(Ah) = hdA + Adh = 0 \quad (2.23)$$

where Ω is the droplet volume and A is the area covered by the liquid having an uniform thickness h . By differentiating equation 2.21 we get the energy variation

$$dF = [\gamma_{LV} + \gamma_{SL} + P(h)]dA - A\Pi(h)dh \quad (2.24)$$

Combining the equations 2.23 and 2.24 we obtain the overall stress in the film

$$\gamma_{film}(h) = \gamma_{LV} + \gamma_{SL} + P(h) + h\Pi(h) \quad (2.25)$$

which is a useful parameter for discussing the equilibrium state between films of different thickness.

Thermodynamical stability of the film requires that [4, 5]

$$\frac{d\Pi}{dh} = -\frac{d^2P(h)}{dh^2} < 0 \quad (2.26)$$

meaning that the function $P(h)$ must be convex. Concave regions have to be eliminated by a double tangent (Maxwell) construction, i.e. a film with the thickness h splits into two films of thickness h_1 and h_2 occupying fractions α_1 and $\alpha_2 = 1 - \alpha_1$ of the surface. The energy becomes $\alpha_1 P(h_1) + \alpha_2 P(h_2)$, lower than the initial $P(h)$. For systems in which the long range van der Waals forces are dominant (when the film thickness is larger than the molecular size a), the function $P(h)$ has the expression

$$P(h) = -\frac{A_H}{12\pi h^2} \quad a \ll h \ll l \quad (2.27)$$

where l is the thickness above which the interaction becomes retarded.

When h is comparable to a , $P(h)$ may display an oscillatory behaviour due to the short range (hard sphere) interactions. Under the assumption that such oscillatory effects are not significant, three possible dependencies of the film free energy vs. thickness are presented in figure 2.2. The graph (a) corresponds to $S_i < 0$, $A_H > 0$ and partial wetting. Graph (b) corresponds to $S_i > 0$, $A_H > 0$ and pseudo-partial wetting. For h smaller than h_{min} , the film will split into regions with thickness h_s ("pancake") and regions of bare substrate. The tangent construction means that $f(0) = f(h_s) + h_s\Pi(h_s)$ i. e. according to 2.25, equal film tensions. For h larger than h_{min} , an uniform film of thickness h_{min} is in equilibrium with a residual droplet. The case of complete wetting, depicted in graph (c), characterized by $S_i > 0$ and $A_H < 0$, can be either a uniform macroscopic film ($h > h_s$) or a "pancake" in equilibrium with the bare substrate, for $h < h_s$.

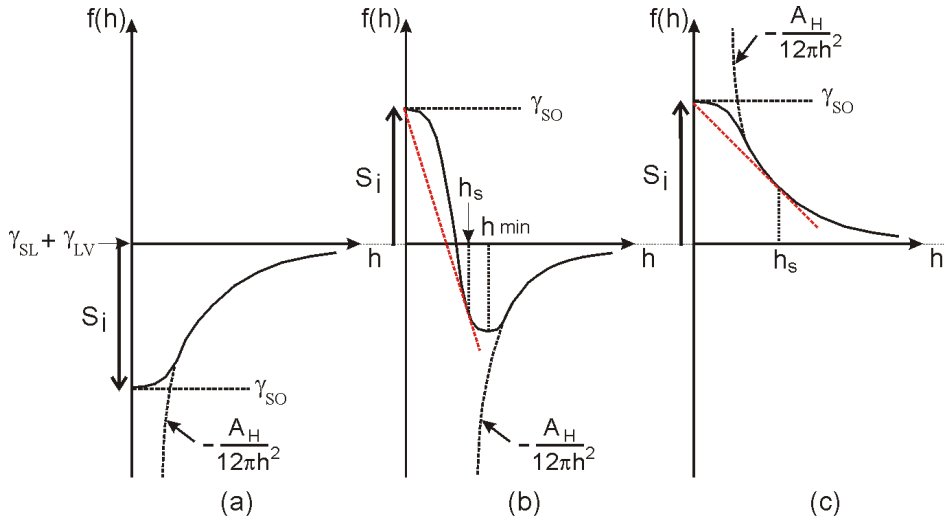


Figure 2.2. Possible variations of the liquid film free energy versus thickness for different values of S and A_H . Situation (a) corresponds to partial wetting, (b) to pseudopartial wetting and (c) to complete wetting. The Maxwell construction (red tangent) defines the stable film thickness.

2.2. Wetting dynamics

Based on thermodynamic arguments, the Young equation 2.3 relates the three interfacial energies via the equilibrium contact angle, θ_e . Moving contact lines can be described in a similar way by a dynamic contact angle θ_d . Although many authors consider the dynamic contact angle as "apparent", their caution derives from theoretical considerations, not experiment. Examined through an optical microscope, the liquid/vapour interface appears to meet the solid surface with a well-defined slope, for both static and dynamic cases. Observations made with a scanning electron microscope [6] have given important insight into the effects of surface roughness and heterogeneity on wetting behaviour. Nevertheless, on smooth and homogeneous surfaces the technique reveals no sudden changes in meniscus curvature down to distances as small as $0.5 \mu\text{m}$ from a moving wetting line. Some geometries used to study the dynamic contact angle are presented in figure 2.3. The sub-figure (e) shows the experimental velocity dependence of the contact angle. The hysteresis, $\theta_a - \theta_r$, can be as small as 1° for smooth and homogeneous surfaces. In this case, it is possible to relate the deviation of the dynamic contact angle from the equilibrium value to the velocity of the contact line. Experiments on forced wetting showed that, in general, the dynamic contact angle depends not only on the speed U but also on the viscosity η and the surface tension γ_{LV} of the liquid. Thus, a convenient way to relate the dynamic contact angle to the velocity is to use the capillary number $Ca \equiv \eta U / \gamma_{LV}$ instead of velocity. For $Ca \ll 1$ (low velocity limit) and complete wetting, the following relation was found experimentally [7]

$$Ca \propto \theta_{d,a}^m, \quad (U \propto \theta_{d,a}^m) \quad (2.28)$$

where $\theta_{d,a}$ is the dynamic advancing angle and $m = 3 \pm 0.5$. This law has a very interesting feature: it does not depend on the magnitude of the initial (positive) spreading coefficient.

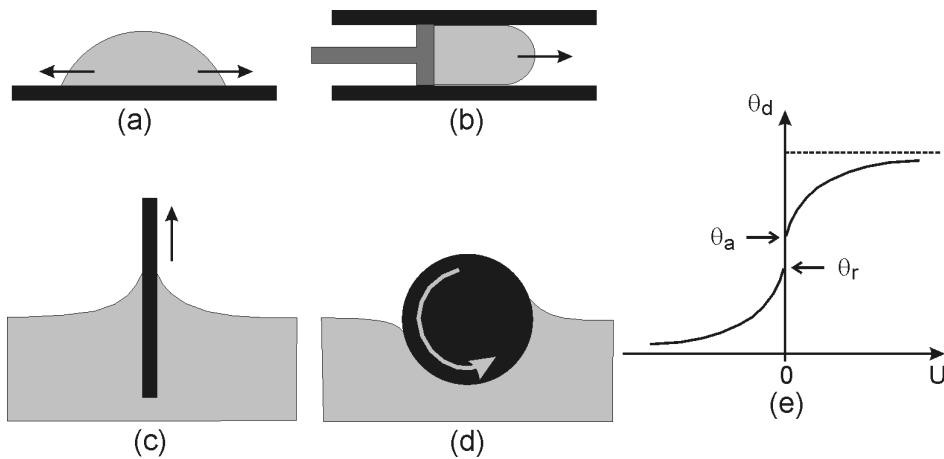


Figure 2.3. Geometries used to study the dynamic contact angle: (a) spreading drops; (b) forced flow in a capillary; (c) steady immersion or withdrawal of fibers, plates from a pool of liquid; (d) rotation of a horizontal cylinder in a pool of liquid. (e) - schematic velocity dependence of the experimentally determined contact angle, where θ_a and θ_r are the static advancing and receding limits.

2.2.1. Models describing the wetting dynamics

Two generally accepted approaches describing the wetting kinetics can be found in the literature. They differ in the relevance of the dissipation force. The hydrodynamic approach [8–10] is based on continuum hydrodynamics and assumes that the viscous friction is the only significant dissipative force in the dynamic meniscus. To remove the singularity (the dissipation diverges in the vicinity of the contact line) the theory operates with cutoff or slip lengths. The second model completely neglects the bulk viscous drag. Instead, the dependence of the dynamic contact angle θ_d on the contact line velocity U is derived from the balance between the driving force (i.e. nonequilibrium Young force), and the (local) friction force in the three-phase contact zone. This approach, based on Eyring's theory of reaction kinetics has been proposed by Blake and Haynes [11]. A combination of the two models was presented by Petrov [12].

2.2.2. The hydrodynamic model

Viscous dissipation, lubrication approximation

Let us consider a linear liquid front having the shape of a simple wedge which advances with constant velocity on a solid substrate. If the dynamic advancing contact angle $\theta_{d,a}$ is small, and the friction in the gas phase is negligible, the "lubrication approximation" of fluid mechanics [13] can be used to calculate the dissipation energy. The wedge is treated as a nearly flat film, with a velocity profile of Poiseuille type (unidirectional flow field, parallel to the interface, see figure 2.4)

$$u_x(z) = u(z) = \frac{1}{2\eta} \frac{\partial p}{\partial x} (z^2 - 2zh) \quad (2.29)$$

where h denotes the position of the liquid/vapour interface. This ensures $u(0) = 0$ at the solid surface and no stress at the liquid/vapor interface, i.e. $(\partial u / \partial z)_{(z=h)} = 0$. An explicit equation for the pressure

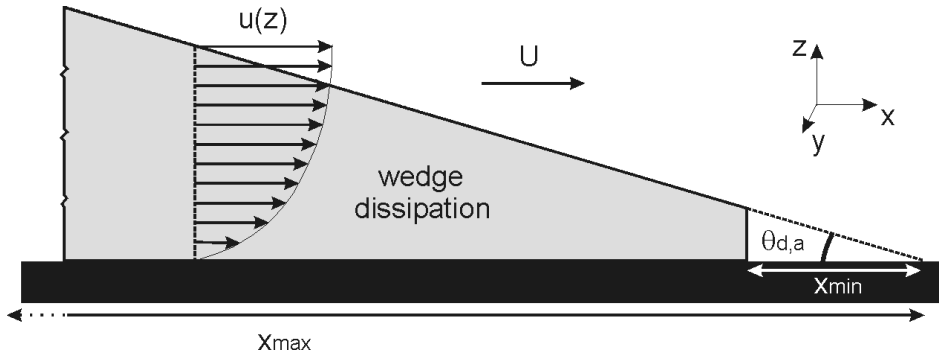


Figure 2.4. The flow field for a simple wedge in motion. For small contact angle the dissipated energy can be calculated using the "lubrication approximation".

gradient is not necessary since we can express the total matter flux as function of the wedge velocity U

$$Uh(x) = \int_0^h u(z) dz \quad (2.30)$$

One can then write

$$u(z) = \frac{3U}{2h^2} (-z^2 + 2hz) \quad (2.31)$$

The viscous dissipation integrated over the film depth is

$$\int_0^h \eta \left(\frac{du}{dz} \right)^2 dz = \frac{3\eta U^2}{h} \quad (2.32)$$

where η is the liquid viscosity. The total energy dissipation per unit length and time in the wedge is

$$T\dot{S} = \int_{x_{min}}^{x_{max}} \frac{3\eta U^2}{h} dx = \frac{3\eta U^2}{\tan \theta_{d,a}} \int_{x_{min}}^{x_{max}} \frac{dx}{x} \approx \frac{3\eta U^2}{\theta_{d,a}} \int_{x_{min}}^{x_{max}} \frac{dx}{x} \quad (2.33)$$

where $\dot{S} = dS/dt$ is the entropy creation during the irreversible process, $h(x) = x \tan \theta_{d,a} \approx x\theta_{d,a}$. The cutoff x_{max} is related to the macroscopic size of the liquid in motion, e.g. $x_{max} \approx R$, for the radius of a spreading drop. The microscopic cut-off x_{min} can be considered in the order of molecular size a , otherwise for $x_{min} \rightarrow 0$ the dissipation would diverge. If the wedge advances on a liquid film of thickness h_f , x_{min} can be approximated to $h_f/\theta_{d,a}$. Within these constrains, we can define a dimensionless coefficient, L

$$\int_{x_{min}}^{x_{max}} \frac{dx}{x} = \ln \left(\frac{x_{max}}{x_{min}} \right) \equiv L \quad (2.34)$$

which ranges from 10 to 15. Therefore, the viscous force per unit length (along the y direction) is given by

$$F_V = \frac{T\dot{S}}{U} = \frac{3\eta UL}{\tan \theta_{d,a}} \approx \frac{3\eta UL}{\theta_{d,a}} \quad (F_V \propto U) \quad (2.35)$$

The driving force

For a clean, ideally smooth surface, the equilibrium contact angle θ_e is defined by the Young equation. If the liquid wedge is set in motion, the dynamical contact angle, θ_d , will differ from its equilibrium value. This gives rise to an unbalanced (non-equilibrium) driving force which has the same direction as the direction of movement, as depicted in figure 2.5. For partial wetting situations, this force is

$$F_D(\theta_d) = \gamma_{SV} - \gamma_{SL} - \gamma_{LV} \cos \theta_d = \gamma_{LV} (\cos \theta_e - \cos \theta_d) \quad (2.36)$$

In terms of the equilibrium spreading coefficient, the equation 2.36 becomes

$$F_D(\theta_d) = S_e + \gamma_{LV}(1 - \cos \theta_d). \quad (2.37)$$

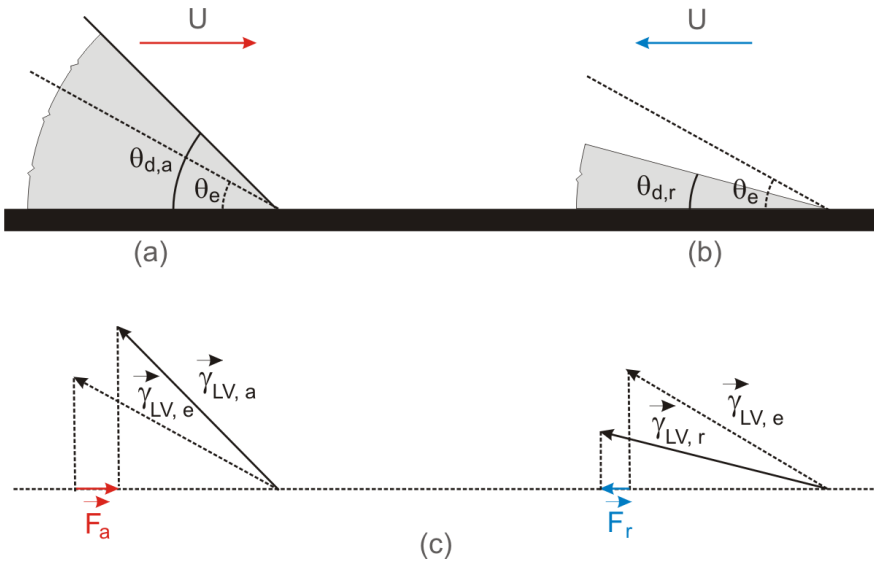


Figure 2.5. Wedge in motion and the deviation of contact angle from its equilibrium value for partial wetting: (a) advancing angle, $\theta_{d,a} > \theta_e$, and (b) receding angle $\theta_{d,r} < \theta_e$; (c) the unbalanced Young forces for the advancing and receding situations, having the same direction as the moving direction of the wedge.

If the initial spreading coefficient S_i is positive, the wedge will usually advance on a solid surface covered with a liquid film, the so-called precursor film. If this film is thick enough to ignore the contribution of long range S-L interactions (i.e. larger than $1 \mu\text{m}$), the driving force for the wedge movement will be given by equation 2.36 and 2.37 with $\cos \theta_e = 0$ and $S_e = 0$, respectively. This situation will be discussed in more detail in the section 2.2.4 of this chapter.

Balance of forces

Considering the dissipation in the wedge as the only force which opposes the capillary driving force, the condition $F_D = F_V$ (equations 2.36 and 2.35) will give

$$\gamma_{LV} (\cos \theta_e - \cos \theta_d) = \frac{3\eta UL}{\tan \theta_d} \quad (2.38)$$

This relation allows to calculate the velocity of the moving wedge

$$U = \frac{\gamma_{LV}(\cos \theta_e - \cos \theta_d) \tan \theta_d}{3\eta L} \quad (2.39)$$

Considering our first assumption that θ_d and θ_e are small, we can use the approximations $\tan \theta \approx \theta$ and $\cos \theta \approx 1 - \theta^2/2$. Therefore, the relation above becomes

$$U = \frac{\gamma_{LV}(\theta_d^2 - \theta_e^2)\theta_d}{6\eta L} \quad (2.40)$$

If θ_e is zero (complete wetting) this equation is consistent with the experimental measurements described by equation 2.28. The spreading dynamics of non-volatile droplets on a totally wettable surface can be also deduced from equation 2.40 which, together with volume conservation and the assumption that the droplet has a spherical cap shape, leads to $\theta_D \propto (\text{time})^{-3/10}$ or, in terms of radius of the liquid-substrate contact area, $R \propto (\text{time})^{1/10}$. These relations are known as Tanner's laws [8] and are remarkably universal.

2.2.3. The molecular-kinetic model

Blake and Haynes [11] and Cherry and Holmes [14] developed molecular-kinetic theories, postulating that the entire energy dissipation occurs at the moving contact line. The wetting kinetics is viewed as a process of desorption of the molecules of the receding fluid and adsorption of those of the advancing one onto adsorption centers of the solid surface. Their model is illustrated schematically in figure 2.6.

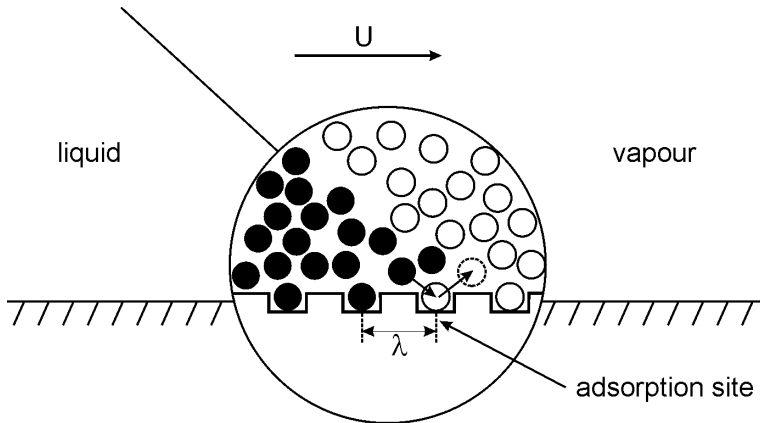


Figure 2.6. Adsorption/desorption model of molecular displacement within the three-phase zone according to [11]. If n is the number of adsorption sites per unit area, the average distance between sites is $\lambda = n^{-1/2}$.

At equilibrium the wetting line will appear to be stationary, but at molecular level, the three-phase zone will usually be in vigorous thermal motion. The molecules of one species constantly interchange with those of the other, either by surface migration or via the contiguous bulk phase. If the frequency of molecular displacements in the forward direction is k^+ and that in backward direction is k^- , then, at equilibrium

$$k^+ = k^- = k^0 \quad (2.41)$$

Application of Eyring's theory of absolute reaction rates allows to relate the equilibrium frequency of molecular displacements k^0 to the molar activation free energy of wetting ΔG_w ,

$$k^0 = \frac{k_B T}{h} \exp\left(-\frac{\Delta G_w}{N k_B T}\right) \quad (2.42)$$

where h is the Planck constant, k_B the Boltzmann constant and N is the Avogadro number. A forward-directed shear stress applied to the molecules within the three-phase zone modifies the profiles of the potential-energy barriers to molecular displacement, lowering barriers in the forward direction and rising those in the backward direction. The wetting line velocity which is related to the net frequency of molecular displacement will be given by $U = \lambda(k^+ - k^-)$. If the irreversible work done by the shear stress per unit displacement of unit length of the wetting line is w , then the work done on each site is w/n (n sites per unit area). If the energy barriers of molecular displacement are symmetrical, $w/2n$ is used to lower the barriers in forward direction while $w/2n$ is used to rise the barriers in the backward direction. Thus the expression of velocity will be

$$U = \lambda \frac{k_B T}{h} \left[\exp\left(-\frac{\Delta G_w/N - w/2n}{k_B T}\right) - \exp\left(-\frac{\Delta G_w/N + w/2n}{k_B T}\right) \right] \quad (2.43)$$

If the shear stress driving the wetting line is provided by the out-of-balance Young forces (equation 2.36), the equation 2.43 becomes

$$U = 2\lambda k_0 \sinh\left(\frac{w}{2n k_B T}\right) = 2\lambda k_0 \sinh\left[\frac{\gamma_{LV}(\cos \theta_e - \cos \theta_d)}{2n k_B T}\right] \quad (2.44)$$

For $\gamma_{LV}(\cos \theta_e - \cos \theta_d) \ll 2n k_B T$ and small angles, the velocity can be approximated by

$$U = k_0 \lambda \gamma_{LV} \frac{(\theta_d^2 - \theta_e^2)}{2n k_B T} \quad (2.45)$$

The merit of this model is that it provides a theoretical basis for the slip at the wetting line emphasizing the role of molecular events occurring within the three-phase zone. The molecular-kinetic model predicts a maximum wetting velocity U_{max} and a minimum dewetting velocity U_{min} . At speeds larger than U_{max} gas bubbles form, which was indeed observed (e.g. for water $U_{max} \approx 5 - 10$ m/s).

2.2.4. Precursor films

For systems in which the liquid spreads spontaneously (to give a nominally zero contact angle), a precursor or primary film of submicrometer to molecular scale thickness moves ahead of the main body of the liquid. Observed for the first time a long time ago by Hardy (1919), such behaviour was believed to be given by evaporation and subsequent condensation of volatile liquids in front of the macroscopic wetting line. More recent experiments involving techniques such as interferometry, ellipsometry or electron microscopy, suggest that the film is present even in the absence of any vapor fraction [15–21]. Precursor films form in case of positive initial spreading coefficients. The driving force of spreading is in such cases

$$F_D = S_i + \gamma_{LV}(1 - \cos \theta_d). \quad (2.46)$$

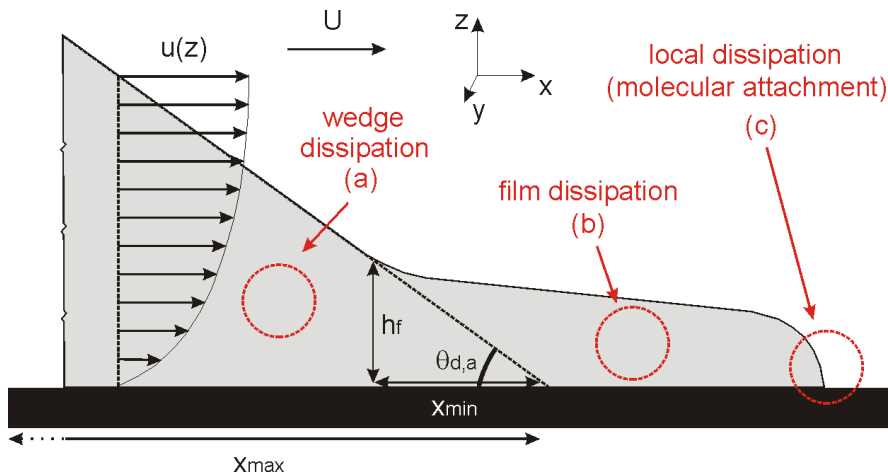


Figure 2.7. The three types of dissipation for systems forming precursor films: (a) in the macroscopic wedge, (b) in the prewetting film, for positive spreading coefficient (c) at the microscopic contact line. For small $\theta_{d,a}$, the velocity profile $u(z)$ in the wedge, can be considered of Poiseuille type.

De Gennes [9] describes three types of dissipation for the case of dry spreading (advancing) of a pure, non-polar liquid attracted towards the solid by long range van der Waals forces. These are schematically presented in figure 2.7. The first type occurs in the macroscopic wedge and, as it was shown, for small dynamic contact angles, it can be calculated by making use of the "lubrication approximation". The second is the viscous dissipation in the precursor film, which was found to be very strong. The third contribution occurs at the molecular scale. In the close vicinity of the contact line, a special loss due to attachment of liquid molecules to the solid may be considered. This third contribution is largely unknown. Thus, the total dissipation per unit time will be given by

$$F_D U = T \dot{S}_w + T \dot{S}_f + T \dot{S}_l \quad (2.47)$$

where w , f , and l stand for wedge, film and microscopic wetting line contributions. At this point we can explain why the kinetics of macroscopic spreading for systems with precursor films does not depend on the magnitude of the positive initial spreading coefficient. The motion of the macroscopic wedge is decoupled from that of the wetting line; hence, the liquid may be considered to spread across an already wetted surface. From the total available driving force, the free energy S_i is dissipated in the film region. What is left, $\gamma_{LV}(1 - \cos \theta_d)$, drives the macroscopic wedge which advances on top of the film. Regarding only the flow of the liquid within the precursor film, a common idea is to consider the driving force in terms of disjoining pressure. The disjoining pressure is a steep, inverse function of film thickness and therefore creates a correspondingly steep, negative pressure gradient between the bulk liquid and the thin periphery of the film. Hence, the liquid is drawn out of the bulk and into the film. A theory describing the dynamics of precursor films was developed by Joanny and de Gennes [22]. Based on continuum hydrodynamics, their approach takes into account the long-range van der Waals forces in terms of gradients of the disjoining pressure. However, this is justified only as long as the thickness of the film remains at least in the mesoscopic range ($\ll 20\text{\AA}$), and thus does not explain the growth of molecularly thin films.

Spreading at molecular scale

Refined ellipsometric and surface plasmon resonance measurements, carried out on different substrates and with various kinds of simple liquids, polymers, surfactant melts, and liquid-crystals, have investigated the growth of molecularly thin precursor films. They show that the length R of the film along the solid surface obeys an universal law $R \propto \sqrt{\text{time}}$ [21, 23–27], regardless of the nature of the species involved. Even in metallic systems like Pb, Bi, and Pb-Bi alloys spreading on a Cu(111) surface, the growth of the precursor film follows the same diffusional law [28]. This law is valid for spreading drops as well as for the capillary rise geometry, in which a vertical wall is placed in contact with a bath of liquid.

In some cases, depending on the nature of the substrate, a remarkable effect of "terraced spreading" takes place, several monolayers advance together stacked on top of one another and each growing as \sqrt{t} [21, 25, 26, 29]. The dynamic layering effect is believed to be generated by the structuring effect of the surface. For instance, thickness profiles of tetrakis (2-ethylhexoxy) silane (spherical molecule, 10 Å diameter) show well defined dynamic layering on uv-ozone cleaned, naturally oxidized (≈ 20 Å silica layer) silicon substrate [29], while the spreading of polydimethylsiloxane (PDMS) on the same substrate proceeds by a fast evolving precursor layer of one molecule thickness [24]. For the latter system, at intermediate stages of spreading, when the macroscopic droplet still supplies the growth of the molecular film, the profile resembles a "mexican hat" and the edge becomes more diffuse. Further away from the spreading drop, the profile develops into submolecular thickness, i. e. the layer compactness is lost by diffusion of molecules on the solid surface (two-dimensional evaporation). The increase of this edge width with time is due to molecular diffusion while the time evolution of the compact precursor film length is viewed as a pseudodiffusive process, in the sense that the diffusion coefficient is thickness dependent. In the case of squalane on bare silicon substrate the surface diffusion takes over liquid cohesion [23] and the profile approaches a Gaussian shape at late times.

Cazabat et. al. [30] present a veritable catalog of spreading morphologies at molecular scale. Following their treatment, for nonvolatile liquids which completely wet the surface and are well below the two-dimensional critical temperature¹ (T_{2C}), the final state of spreading is a pancake of thickness h_e with sharp edges. The value of h_e depends on the shape of the disjoining pressure $\Pi(h)$ and can be obtained from the implicit equation

$$S_i = P(h_e) + h_e \Pi(h_e). \quad (2.48)$$

In the molecular range of thicknesses the short range interaction comes into play: steric interactions lead to an oscillating behaviour of the disjoining pressure. The period is h_0 , the size of the molecules in the liquid film. In experiments, the regions for which $\Pi(h)$ has a positive slope are unstable and lead to transitions between films of different thickness at constant Π . Thus, if only steric interactions play a role in the short range part, the allowed thicknesses are multiples of h_0 (terrace spreading). If the spreading occurs on surfaces with a grafted layer, this will introduce a negative contribution to the short range part of the disjoining pressure and the smallest thickness can be significantly larger than h_0 .

¹Thermodynamically, a liquid is nonvolatile in three dimensions if the temperature is well below the T_{3C} . However, this bulk property does not fully characterize the behaviour of molecularly thin films with respect to evaporation. Two-dimensional evaporation will occur if the temperature is above the two-dimensional critical temperature T_{2C} , which is usually $\approx 0.5T_{3C}$.

Several approaches have been considered in order to explain why the molecularly thin precursor layers spread following the \sqrt{t} law. The "stratified droplet" model proposed by de Gennes and Cazabat [31] describes the evolution of the drops structured in terraces of equal thickness assuming that the molecules evolve as a two dimensional incompressible fluid in each terrace. The fluid permeates from the upper terrace to the lower terrace only in a thin annulus at the borders of each terrace. Although this model does not explain the terraced structure, it recovers the \sqrt{t} law from the competition between the liquid-solid attractions, which represent the driving force of spreading, and viscous-type frictional forces, which control particle dynamics on the solid surface.

A microscopic, analytically solvable model [27, 32] considers the precursor film as a lattice gas of hard-sphere interacting particles connected to a reservoir (droplet). The fluid particles move under the action of random thermal forces and attractive van der Waals forces exerted by the solid. Particles at the tip of the film (boundary particles), which are in contact with the interface, are the subject of the "restoring" force exerted by the interface. This model establishes analytically the square root behaviour and explains the growth mechanism by a diffusional transport of vacancies from the tip of the film to the edge of the macroscopic meniscus. In another analytical study [33], depending on the value of a dimensionless parameter describing the lateral liquid-liquid interaction, it is found that the film can be either (i) an ideal surface gas which advances according to the $\sqrt{t \ln(t)}$ law, or (ii) a liquid-like phase growing as $A\sqrt{t}$. A can be positive, zero or negative thus describing at molecular scale the wetting, the partial wetting and dewetting, respectively. Molecular dynamics and Monte Carlo simulations [34–36] also reproduce the square root behaviour.

2.3. Running Droplets

Spreading of droplets on a homogeneous solid surface is driven by a symmetrical field of unbalanced Young forces acting at the contact line. As a consequence, the droplet center of mass does not change. If the force field is asymmetrical, the drop will either be distorted and pinned, or it will move on the surface.

Chemical inhomogeneities or temperature gradients can generate a spatial variation of the surface tension of a liquid/vapour interface. In such cases, the liquid surface is subject to a stress given by the surface tension gradient, and flow patterns in the liquid can be observed. This phenomenon is known as Marangoni effect. An example of the Marangoni effect is the formation of "wine tears" on the walls of a glass of wine (mixture of water and alcohol). The alcohol evaporates faster than water. This leads to an increase of the surface tension ($\gamma_{H_2O} > \gamma_{ethanol}$) in the film compared with the bulk mixture, which generate an upwards flow in the film zone. A similar example is when two dissimilar droplets chase each other like the case of PDMS and a solvent (transdecane) [5]. The solvent evaporates faster and condenses preferentially on the nearest region of the PDMS drop, leading to an increase of surface tension which drives the PDMS towards the solvent drop.

2.3.1. Passive drops on a chemically heterogeneous solid surface

A droplet or a liquid ridge deposited on a solid surface at the boundary between two regions of different wettability is not stable. In such a case, the droplet will move towards the more wettable surface until the contact with the boundary between the two regions is lost. Based on theoretical analysis proposed by Raphaël [37], this effect was studied experimentally by Ondarçuhu and Veyssié

[38]. A similar behaviour can be observed when the solid surface energy varies in a continuous way. Such substrates have been developed in biotechnology to separate proteins according to their degree of hydrophobicity. Chaudhury and Whitesides succeeded to prepare hysteresis-free slides with a wettability gradient by exposing a silicon wafer to the diffusion front of decyltrichlorosilane vapor [39]. By this technique, they created a concentration gradient on the surface and, accordingly, a hydrophobicity gradient. This leads to a contact angle with water varying from 10° to 25° over a distance of one centimeter. Even when the wafer is tilted with the hydrophobic part at the bottom, a small drop of water is able to run uphill at speeds of the order of mm/s. Coatings with wettability gradients can be used in heat exchangers for increasing the efficiency of cooling as suggested by Daniel et al. [40]. In their experiments they observe small drops (0.1 to 0.3 mm) driven by energies of coalescence and collimated by the forces of the chemical gradient, moving with speeds that are hundred to thousand times faster than those of typical Marangoni flows.

2.3.2. Reactive wetting

Drops may also move on initially homogeneous surfaces. This is the case for instance of "active" drops which are solutions of chemicals that can deposit a layer on the surface or react with it (e. g. nitric acid on a copper plate). The mechanism is based on the physisorption of a dissolved surfactant at the solid/liquid interface or a chemical reaction between a dissolved reagent with the solid surface. In both cases the wettability underneath the droplet is altered. Fluctuations eventually brake the symmetry leading to the motion of the droplet. By moving, the droplets leave behind a less wettable trail. A moving drop will avoid such regions on the substrate (self-avoiding movement). Not only solutions, also pure liquids (so-called *autophobic* liquids) can behave in this way [41].

The effect of chemical reactions has been studied notably by Bain and coworkers [42] using fatty acids in solution, which react with OH- groups of silica or glass rendering the surface hydrophobic. The effect can be enhanced by using acids containing fluorinated chains, generating surfaces with poor wettability for water. Another example has been studied by dos Santos and Ondarçuhu [43]. They used droplets of n-alkane containing chlorosilane which reacts with the glass or silicon substrate forming dense grafted monolayers. In order to analyze the droplet velocity vs. size and reagent concentration, they used patterned substrates (glass surfaces with hydrophilic stripes). Without this precaution, the movement may be erratic due to very high sensitivity of the reaction to chemical heterogeneity of the substrate. Similar dynamic phenomena have been observed in systems consisting of metals like reactive wetting and dewetting of an eutectic SnPb alloy on a Au/Cu/Cr thin multi-layer structure [44], and alloying propelled migration of Sn islands on a Cu(111) surface at room temperature [45].

2.3.3. Velocity of running drops

In order to analyze quantitatively the movement of drops on solid surfaces with a surface energy gradient, we can ignore gravity and assume two simple geometries, circular ridges (2D) and spherical cap (3D) drops. These geometries are valid if the lateral size of the region covered with liquid is smaller than the capillary length, $k^{-1} = \sqrt{\frac{\gamma}{\rho g}}$, otherwise the drop will be flattened by gravity.

In figure 2.8 (a), a small drop sits on a solid surface characterized by a small surface energy gradient. If the drop does not move, the contact angles in A and B have their equilibrium values, $\theta_{e,A}$

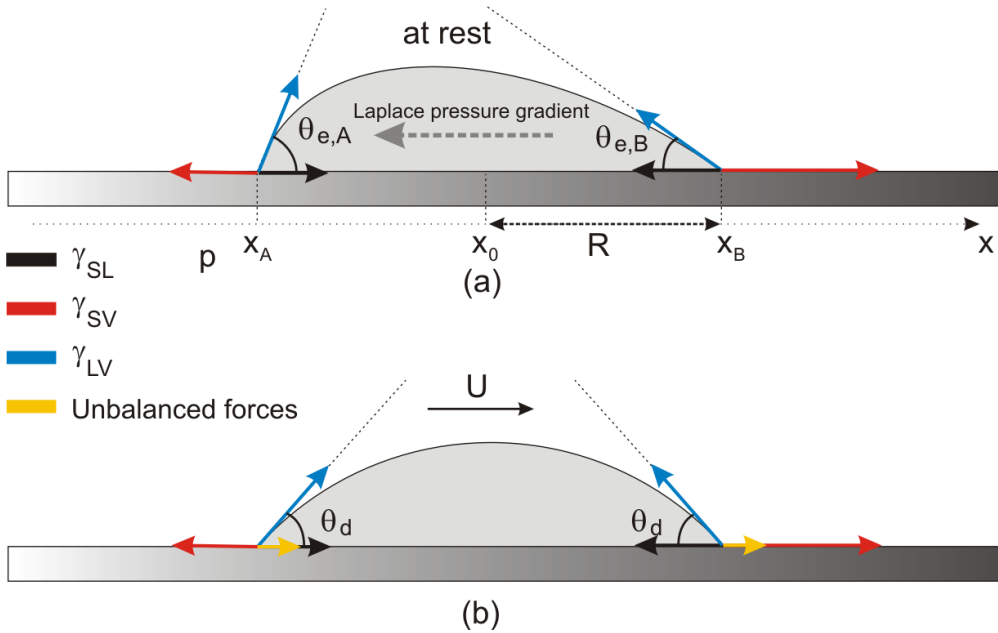


Figure 2.8. Drop on a surface with wettability gradient (solid surface energy increases from left to right). The "static" situation (a) is not stable due to the Laplace pressure gradient. The asymmetry sets the drop in motion (b), with a shape close to spherical cap.

and $\theta_{e,B}$. Since the equilibrium contact angle decreases with increasing solid surface energy, the curvature in A will be larger than in B and the corresponding (local) Laplace pressure will be greater in the vicinity of A than close to B. This Laplace pressure gradient will set the drop in motion. When the droplet moves (2.8 (b)), its shape can be approximated by a spherical cap. The contact angles are the same at both, trailing and leading edges, $\theta_{d,a} \approx \theta_{d,r} \approx \theta_d$. The value of the dynamic contact angle can be obtained by writing the equation 2.39 for both edges which move with the same speed [46]. The result is

$$\theta_d = \arccos \left(\frac{\cos \theta_{e,A} + \cos \theta_{e,B}}{2} \right) = \sqrt{\frac{\theta_{e,A}^2 + \theta_{e,B}^2}{2}} \quad (2.49)$$

For the simplest case of a ridge (2D problem), the velocity can be calculated from the balance between the driving force, in this case

$$F_D = (\gamma_{SV} - \gamma_{SL})_B - (\gamma_{SV} - \gamma_{SL})_A = 2R \frac{dS}{dx} \quad (2.50)$$

and the dissipation force, dominated by the two wedges,

$$F_V = 3\eta U \int_{x_A}^{x_B} \frac{dx}{h(x)} \approx 6\eta U \int_{x_A}^{x_0} \frac{dx}{(x-x_A)\theta_d} = 6\eta \frac{UL}{\theta_d} \quad (2.51)$$

Hence, the velocity is

$$U = \frac{2R\theta_d dS}{6\eta L dx} = \frac{2h_{max} dS}{3\eta L dx} \quad (2.52)$$

Note that, according to the equation above, the velocity increases linearly with R because the absolute difference of unbalanced Young forces increases linearly with size. The same equation is also valid

for the spherical cap geometry but the derivation [46] is more complicated. To ensure the balance between the viscous and unbalanced Young forces, the flow lines within the droplet must be normal to the contact line in any point.

Raphaël [37] analyzed theoretically a different situation: instead of the *surface energy gradient*, he considered that the drop experiences a *constant difference in wettability*, i.e. half of the drop is in contact with a solid surface which gives an equilibrium contact angle $\theta_{e,A}$, while the other half contacts a surface characterized by the equilibrium contact angle $\theta_{e,B}$. As expected, he found a slightly different equation for the droplet velocity,

$$U = \frac{\gamma_{LV}}{6L\eta} \tan \theta_d (\cos \theta_{e,B} - \cos \theta_{e,A}) \quad (2.53)$$

indicates that the droplet velocity does not depend on its size.

2.4. Physico-chemical properties of n-alkanes

Normal alkanes are linear hydrocarbon chains, $CH_3 - (CH_2)_{n-2} - CH_3$ (in the following abbreviated C_n , n is the number of carbon atoms in the molecule), some of the simplest organic compounds. The alkane molecules are non-polar and their (long range) intermolecular interactions are only of van der Waals type. They are the main building blocks of lipids, liquid crystals, polymers, surfactants, and many other, more complex organic compounds. Thus, the alkane properties influence the properties of these complex molecules, and a good knowledge of them can be helpful in understanding those of more complex organic molecules [47]. Under normal conditions (room temperature, atmospheric pressure), alkanes are gases from C_1 to C_4 , from C_5 to C_{16} they are liquids, and from C_{17} on they are solids.

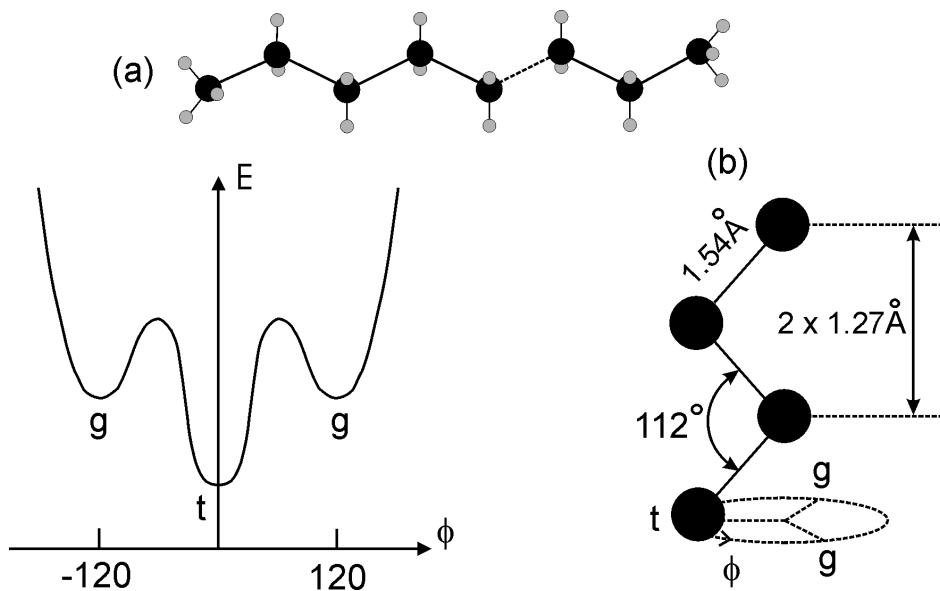


Figure 2.9. (a) The structure of the n-alkane molecule. (b) The bond conformations and structural parameters, showing the positions for *trans* (t) and *gauche* (g) conformations. The corresponding energy has two local minima for the g positions and a global one for t.

As shown in Fig. 2.9, the C–C bond length is 1.54 \AA and the angle between two C–C bonds is 112° [47]. Any three neighboring carbons (two neighboring bonds) define therefore a plane, relative to which a fourth carbon can assume one of three orientational positions, (shown in fig.2.9(b)). The global energy minimum position for the fourth carbon is in the plane defined by the other three carbons (a *trans* bond). Two local energy minima are obtained for the fourth carbon rotated by 120° out of that plane (*gauche* bonds). The energy difference between the *trans* and the *gauche* bonds depends on the intra- and interchain interactions. In the bulk crystalline phases at low temperatures, the energy difference is significantly higher than $k_B T$. Therefore almost all bonds remain in the lowest, *trans*, conformation. The molecule is straight, with a length of $(n-1)1.27 \text{ \AA}$ between the terminal carbon atoms, where $1.27 \text{ \AA} = 1.54 \text{ \AA} \sin(112^\circ/2)$ is the projection of the bond length on the chain axis. The *all-trans* length H_0 of an n-alkane molecule is [48]

$$H_0 = 4.7 + 1.27(n - 2) \quad (2.54)$$

where the first term accounts for the two methyl groups.

The bulk solid structures of n-alkanes are well described in literature. For example, the recent comprehensive review of Dirand et al. [49] presents the crystallographic structures, thermodynamic properties, and crystallization behaviour for pure n-alkanes as well as for synthetic and real petroleum mixtures.

In the liquid phase, at high temperatures, the energy difference between *trans* and *gauche* bonds becomes smaller than $k_B T$. The chain becomes flexible and bonds are excited into *gauche* conformations, rendering the molecule nonlinear and planar.

2.4.1. Bulk, crystalline n-alkane structures at low temperatures

In the crystal, the molecules have the form of plane-zigzag chains of carbon atoms and their axes are parallel, forming a layered structure. The low temperature structure as well as other physicochemical parameters of n-alkanes show an "even-odd effect" which is a consequence of the structure of the chain itself. The structural difference lies in the symmetries of even- and odd-numbered molecules. By moving along the long, c crystallographic axis, every second molecule in an odd n-paraffin crystal will be translationally identical (structure composed of layers), while in an even n-paraffin crystal all molecules are successively related by simple translation (one layer structure).

For the homologous series C_{13} – C_{60} , the lattice types, X-ray first long spacing, tilting angles, and *key structures* (according to classification defined by Nyburg and Potworowski [50]) are presented in table 2.1. All odd-numbered n-paraffins are packed in an orthorhombic ($a \neq b \neq c$, $\alpha = \beta = \gamma = 90^\circ$) structure. For the even numbered n-alkanes the packing can be triclinic ($a \neq b \neq c$, $\alpha \neq \beta \neq \gamma \neq 90^\circ$), monoclinic ($a \neq b \neq c$, $\alpha = \gamma = 90^\circ$, $\beta \neq 90^\circ$) or orthorhombic, with two different key structures.

Table 2.1. Low temperature n-alkane structures, X-ray first long spacing, tilting angles, and key structures as function of the number of carbon atoms.

Alkane, C_n	Lattice	X-ray first long spacing, [Å]	tilt [°]	Key structure
odd, $13 \leq n \leq 41$	orthorhombic	$d_{002}=1.2724n + 1.8752$	0	" C_{23} - $Pbcm$ "
even, $14 \leq n \leq 26$	triclinic	$d_{001}=1.2085n + 1.2868$	18.23	" C_{18} - $P1$ "
even, $28 \leq n \leq 36$	monoclinic	$d_{001}=1.1329n + 1.4962$	27	" C_{36} - $P2_1/a$ "
even, $n=38, 40, \text{ and } 44$	orthorhombic	$c/2=1.1308n + 1.6137$	27	" $Pbca$ "
even, $n=46, 50, \text{ and } 60$	orthorhombic	-	-	" C_{36} - $Pca2_1$ "

2.4.2. Bulk structural behaviour in the vicinity of the melting point

With increasing temperature, bulk n-alkanes can display solid-solid transitions which can be observed by X-ray diffraction or by differential scanning calorimetry (DSC). It is possible to distinguish two categories of polymorphous phases: crystal phases at low temperatures, and the so-called *rotator phases* at high temperatures (also denoted as *plastic crystals* or *highly ordered smectics*). The rotator phases are layered structures, characterized by long range positional order of the molecules in three dimensions but no long-range order in the rotational degree of freedom of the molecules about their long axis. They can be distinguished from the crystal phases by the area per molecule (as viewed

along the chain axis) which is above $\approx 19.5 \text{ \AA}^2$ in the rotator phases and below $\approx 18.5 \text{ \AA}^2$ in the crystal phases, respectively.

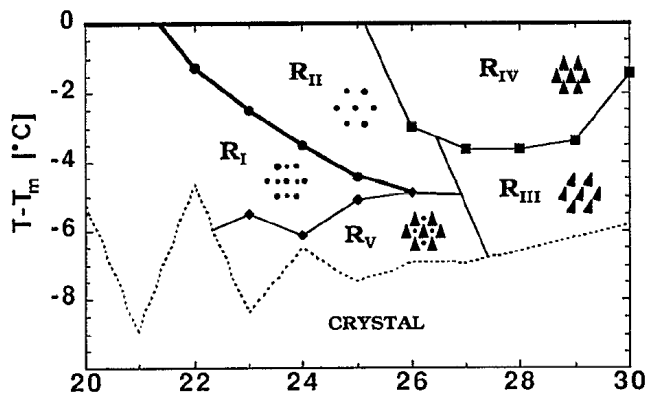


Figure 2.10. Temperature-chain length phase diagram plotted with respect to melting temperature, according to reference [51].

Below the melting point, there are two possible types of transitions: (i) crystal-crystal and rotator-rotator transitions (appearing in each category of polymorphous phases, especially for the odd-numbered C_n 's), and (ii) crystal-rotator transitions, characterized by a higher transition enthalpy than the one associated to crystal-crystal and rotator-rotator transitions. All crystal-crystal transitions lead to phases whose structures display differences in the stacking modes of molecular layers along the long crystalline c -axis and molecular conformation defects, especially of the end-*gauche* type. Despite this, any important modification of the molecule orientation around the c -axis is not observed in the crystalline phases of odd-numbered C_n 's [49].

The rotator phases have been known for quite some time in part due to the early work of Müller [52]. Since then, clear distinctions between the rotator phases were made (Doucet et al. [53–58], Ungar et al. [59, 60], Dorset et al. [61–63] and Sirota et al. [51, 64–66]). Initially four rotator phases have been identified. The R_{II} phase has the molecules untilted with respect to the layers which are packed in a hexagonal lattice with a trilayer stacking sequence (also referred to as rhombohedral, RH). R_I phase is also untilted and contains a rectangularly distorted hexagonal lattice and a bilayer stacking sequence (also referred to as face centered orthorhombic, FCO). The R_{IV} phase is tilted and monoclinic, and the R_{III} is tilted and triclinic. Sirota et al. [64] found a fifth rotator phase, R_V , similar to the R_I phase with the molecules tilted towards the next nearest neighbour. When any combination of the five rotator phases occurs, it is always in the following order on reducing temperature: $R_{IV} \rightarrow R_{III} \rightarrow R_{II} \rightarrow R_I \rightarrow R_V$ [64]. In figure 2.10 is plotted the temperature-chain length phase diagram, according to [51]. The temperature values are relative to the melting point.

2.4.3. Interfacial behaviour, surface freezing

Both theory and experiment show that with very few exceptions it is the *less ordered surface* phase which coexists with the *more ordered bulk* phase, i.e. the surface melts at lower temperature than the bulk. This phenomenon, called surface melting (shown schematically in figure 2.11, (a)) has been discovered in almost all solids studied. The behaviour of long-chain alkanes is quite unique. They show the rare phenomenon of *surface freezing* (SF), i.e. the melting temperature of the of the alkane

molecules at interfaces is higher than in bulk, cartoon (b) in figure 2.11. This was observed for the first time at liquid/vapour interface [67]. It has meanwhile also been observed at the solid(SiO_2)/vapour interface [68] where the surface freezing is correlated to a wetting transition. Surface freezing has been explained by a fluctuation-based theory [69].

The sequence of images in figure 2.12 shows a morphological transition of an undecooled, partially wetting, hexatriacontane drop from a spherical cap shape to a distorted shape. This transition may be a consequence of surface freezing at the liquid/vapour interface. The rare occurrence of such a process suggests that small size alkane drops do not usually freeze at the liquid/vapour interface even when the temperature is a few degrees below the bulk melting temperature.

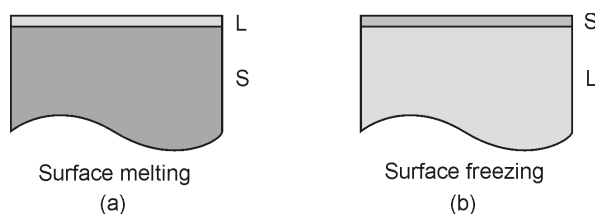


Figure 2.11. Schematic drawing of surface induced melting (a) of a semi-infinite solid and (b) of the surface induced freezing of a semi-infinite liquid.

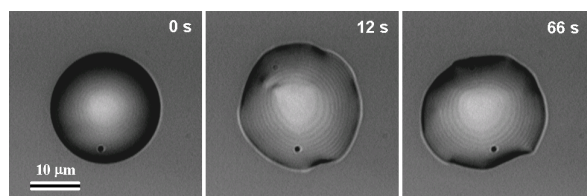


Figure 2.12. Sequence of optical microscopy images showing changes in the morphology of a hexatriacontane (C_{36}) drop at 4°C below bulk melting temperature. The drop sits on its own molecularly thin terrace. The time values are relative to the initial moment of the transition.

2.5. Theory of melting

2.5.1. Bulk melting mechanisms, surface premelting

Although freezing is a complicated process, there is a general agreement about its essential features. In contrast, there has been a long-standing debate about the process that leads to melting in solids [70, 71]. Many theoretical criteria explain the melting process in terms of various instability considerations [72]. Among these, two of them have been frequently discussed in literature: the Lindemann's vibration instability criterion [73], predicting that melting takes place once the thermal root-mean-square displacement of atoms from their equilibrium positions in the crystal reaches a critical fraction of the interatomic distance (typically 10-20%) and Born's shear instability criterion [74], which states that melting occurs when the shear moduli of the crystal become zero, i.e., the crystal loses its rigidity. Originally, these theories consider the melting process as a breakdown of the crystal lattice occurring uniformly throughout the solid at the melting point, i.e. melting is homogeneous. However, there is ample experimental evidence that melting is actually heterogeneous, involving nucleation of the liquid phase at some preferred sites of the solid. The melting process can start between solid and vapour ("surface melting"), between two materials ("interfacial melting"), and between crystallites of the same substance ("grain-boundary melting") or from dislocations ("dislocation-mediated melting"). The most likely site from where the melting starts is the free surface of the solid.

Surface premelting solves the intriguing puzzle of melting, namely why liquids can be cooled below the freezing point, whereas solids cannot be heated above the the melting point. On the basis of classical nucleation theory one expects, upon melting and freezing, that hysteresis effects should occur. The absence of "overheating" of solids, is indicative of the general absence of an energy barrier for the nucleation of melt. Tammann [75] was the first to point out that the surface may play an important role in initiating melting. Surface premelting can be explained considering the Lindemann criterion. Surface atoms are more loosely bound compared to bulk (reduced number of neighbours) and therefore their vibrational amplitude is higher. Consequently, at the surface the Lindemann criterion is satisfied at lower temperature.

Surface melting means wetting of a solid by its melt which occurs when the surface energy of the combined solid-liquid-vapour interface is lower than that of the "dry" solid,

$$\gamma_{SL} + \gamma_{LV} < \gamma_{S0} \quad (\text{at } T < T_{mp}) \quad (2.55)$$

The reduced surface energy makes it advantageous for a thin layer of the solid to premelt at temperatures lower than the bulk transition. Not all the facets are wetted by the melt liquid [76], but since typical crystals have some facets that are wetted, premelting is a general rule. Theory predicts that the temperature at which premelting begins and the temperature dependence of the film thickness are controlled by the interactions within the system. In van der Waals solids, premelting begins typically at a reduced temperature $t = (T_{mp} - T)/T_{mp}$ smaller than 0.1, and the film thickness increases as $t^{-1/3}$ close to T_{mp} . The power law has been confirmed by experiments on rare-gas films [77]. In many metals the thickness typically varies as $|\log(t)|$, which is the temperature dependence characteristic of short range interactions [78].

By suppressing surface melting, overheating to temperatures well above the equilibrium melting point (the temperature at which both solid and liquid forms of a material can exist in thermodynamic

equilibrium) has been achieved. Up to now, the suppression of premelting has been attempted only by completely confining the solid and burying all surfaces including those which premelt. For instance, the experiments of Daeges et al. [79] demonstrated that silver monocrystals spheres (≈ 0.15 mm diameter) covered with gold ($T_{mp}^{Au} > T_{mp}^{Ag}$) can be overheated up to ≈ 25 K for periods in the order of one minute. However alloying between the two metals (diffusion of Au into Ag) may have influenced the result. Banhart et al. [80] found "extreme" overheating effects in Sn and Pb clusters encapsulated in graphitic fullerene-like shells. However, the observed overheating could be caused entirely by the effect of very high pressure on the melting point (see also [81]).

2.5.2. Influence of size, dimensionality and confinement on the melting temperature

Size and dimensionality are also important parameters determining the melting point. For solids with free surfaces, a depression of the melting point with decreasing size was observed experimentally. Applying the liquid drop model, Nanda et al. [82] derived a generalized expression for the melting point depression in low-dimensional systems:

$$T_{mp}^* = T_{mp} \left(1 - \frac{\beta}{zd} \right) \quad (2.56)$$

were $z = 1, 3/2$ and 3 for nanoparticles, nanowires and thin films, respectively, and T_{mp}^* is the corresponding size-dependent melting temperature for the considered geometries. Note that d represents the diameter in case of nanoparticles and nanowires, whereas it represents the thickness in case of thin films. The parameter β depends on the three material parameters: the atomic volume (V_{at}), surface energy (γ) and bulk melting temperature according to:

$$\beta \propto \frac{V_{at}\gamma}{T_{mp}}. \quad (2.57)$$

The same model can be extended to the case of embedded nanoparticles with epitaxial interface between their material and the one of the surrounding matrix (e.g. Pb in Al). In such cases, the expression 2.56 becomes:

$$T_{mp}^* = T_{mp} \left[1 - \frac{\beta}{d} \left(1 - \frac{\gamma_M}{\gamma} \right) \right]. \quad (2.58)$$

were γ_M is the surface energy of the embedding matrix. It can be seen from equation 2.58 that nanoparticles will melt above the melting temperature if $\gamma_M > \gamma$.

Based on the Lindemann criterion for melting, a thermodynamic model for size-dependent melting temperature has been proposed by Shi [83] and further developed, notably by Jiang et al. (see [84] and the references therein). The model predicts the following size-dependent melting temperature

$$T_{mp}^* = T_{mp} \exp \left(\frac{1 - \alpha}{d/d_0 - 1} \right). \quad (2.59)$$

In equation 2.59, α is a size independent parameter equal to the ratio between the mean-square displacement (msd) of surface atoms of a crystal and that of volume atoms and d is either the diameter (nanoparticles, nanowires) or the thickness for a film. The parameter d_0 has the meaning of a critical size (at which almost all atoms of the nanocrystal are located on the surface). The value of d_0

depends on the dimensionality D of the crystal ($D = 0, 1, 2$ for nanoparticles, nanowires and films, respectively). The relation between d_0 and D is

$$d_0 = 2(3 - D)h \quad (2.60)$$

with h being the atomic diameter. The equation 2.59 is monotonically controlled by α : if $\alpha > 1$, T_{mp}^* decreases with decreasing d whereas if $\alpha < 1$, T_{mp}^* increases with decreasing d , relative to T_{mp} . Depending on whether the system is an embedded nanocrystal with coherent or semi-coherent interfaces or a free standing film, different expressions for α can be assumed (see [84]). This model fits reasonably some experimental data presented in the literature for both nanocrystals with free-standing surfaces (depression of T_{mp}^*) and nanocrystals embedded in a matrix with coherent or semi-coherent interfaces. Furtheron, Jiang et al. conclude that overheating of nanocrystals occurs when the following conditions are satisfied: (i) the melting temperature of the matrix material is higher than that of the embedded nanocrystal; (ii) the interface between nanocrystals and matrix is (semi-)coherent; (iii) the atomic diameter of the nanocrystal is larger than that of the matrix.

A detailed thermodynamic treatment of surface melting of nanoscopic epitaxial film is presented by Müller and Kern [85]. They consider the following layered structure: V (vapour) / L(liquid film) / S(solid film) / B (semi-infinite, bulk solid substrate). In addition to the usual spreading coefficient of a liquid melt on its own semi-infinite solid:

$$S = \gamma_{SV} - \gamma_{SL} - \gamma_{LV} \quad (2.61)$$

whose sign indicates whether a system premelts ($S > 0$) or not ($S < 0$), for the case of an epitaxial solid film on a semi-infinite substrate they introduce a similar spreading coefficient:

$$S^* = \gamma_{BL} - \gamma_{BS} - \gamma_{SL} \quad (2.62)$$

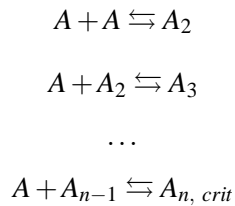
The new parameter S^* describes the wetting behaviour of the solid film intercalated between the liquid film and the semi-infinite solid substrate. According to the sign of S^* two types of surface melting can be predicted. When this parameter is negative, the attraction between L/S and S/B interfaces boosts the premelting which then occurs in two steps: a continuous premelting followed by a first order transition. When S^* is positive, the repulsion between the same interfaces suppresses the premelting so that a part of the deposited solid remains solid above its melting point.

2.6. Classical nucleation theory, crystallization from melt

The condition of undercooling below its T_{mp} alone is not sufficient for a system to begin to crystallize. The formation of any new phase from a bulk parent phase requires (with the exception of spinodal decomposition) the creation of an interface between the two phases. Before crystals can develop there must exist in the liquid a number of minute solid bodies (*embryos, nuclei or seeds*) that act as centers of crystallization. The formation of such small particles requires an amount of work which depends on the interfacial tension of the interface. Nucleation may occur spontaneously, or it may be induced artificially. Agitation, friction, extreme pressures (*e.g.* in cavitation, on cavity collapse, the pressure can reach 10^{-5} bar) can induce nucleation in melts. To avoid confusion, the terminology related to nucleation (which is used in the following) will be defined here. In general, the term *primary* refers to cases of nucleation in systems that do not contain crystalline matter. *Primary* nucleation can be of two types: *homogeneous* or *heterogeneous* (induced by foreign particles). In contrast, *secondary* nucleation (nucleation induced by crystals) describes the formation of nuclei in the vicinity of crystals present in a undercooled melt, due to similar or identical structure between the forming nuclei and the crystal.

2.6.1. Homogeneous nucleation

Exactly how a stable crystal nucleus is formed within a homogeneous fluid is not known with certainty. The number of molecules in a stable crystal nucleus can vary from a few to thousands: ice nuclei, for instance, may contain about 100 molecules. However, a stable nucleus can hardly result from the simultaneous collision of the required number of molecules since this is an extremely rare event. More likely, it will arise from a sequence of bimolecular additions according to the scheme:



Further molecular additions to the critical cluster would result in nucleation and subsequent growth of the nucleus. Many of the embryos or "sub-nuclei" fail to achieve maturity; they simply redissolve because they are extremely unstable. If, however, the nucleus grows beyond a certain size (n_{crit} , *critical nucleus*), it becomes stable under the average conditions of undercooling. The classical nucleation theory, stemming from the work of Volmer and Weber (1926), Farkas (1927), Becker and Döring (1935) and others, was originally developed for droplet condensation from undercooled vapours but can be extended to crystallization from undercooled melts. Assuming the formation of a spherical nucleus, the associated excess free energy is

$$\Delta G_{tot} = \Delta G_I + \Delta G_V = 4\pi r^2 \gamma_{SL} + \frac{4}{3}\pi r^3 \Delta g_V \quad (2.63)$$

where r is the nuclei radius and ΔG_{tot} is the overall excess free energy between a small solid particle and the same amount of liquid in the undercooled melt. The two contributions to ΔG_{tot} are the positive ΔG_I , surface excess free energy, associated with the formation of the S-L interface and a

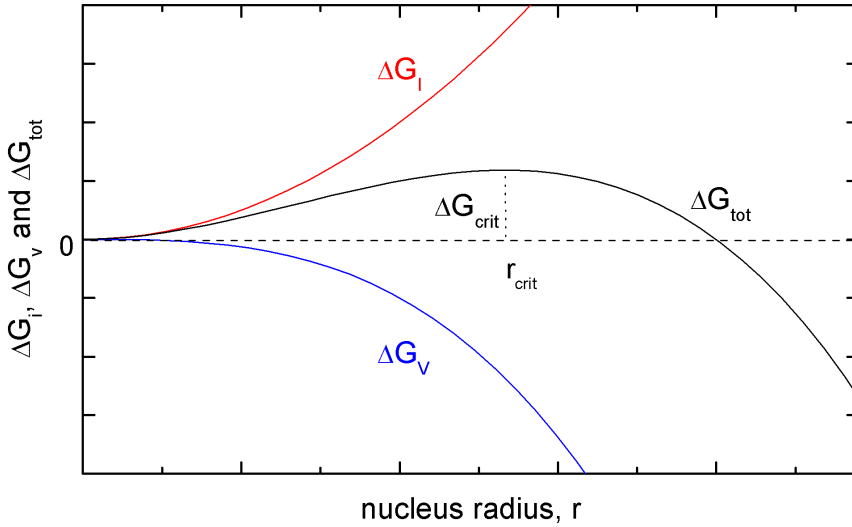


Figure 2.13. Free energy plot for nucleation showing the existence of a "critical nucleus".

negative volume contribution $\propto \Delta g_V$, the excess free energy per unit volume between a very large particle ($r \rightarrow \infty$) and the same amount of liquid in the melt. The two terms of the right-hand side of equation 2.63 are of opposite sign ($\Delta g_V < 0$) and scale differently with radius, hence the total free energy passes through a maximum (see figure 2.13).

The maximum value of ΔG_{tot} , i.e. ΔG_{crit} , corresponds to the critical nucleus, r_{crit} . For a spherical cluster it is obtained by setting $d\Delta G_{tot}/dr = 0$:

$$\frac{d\Delta G_{tot}}{dr} = 8\pi r\gamma_{SL} + 4\pi r^2\Delta g_V = 0 \quad (2.64)$$

therefore:

$$r_{crit} = \frac{-2\gamma_{SL}}{\Delta g_V} \quad (2.65)$$

From the equation 2.63 and 2.65 we get:

$$\Delta G_{crit} = \frac{16\pi\gamma_{SL}^3}{3(\Delta g_V)^2} = \frac{4\pi\gamma r_{crit}^2}{3} \quad (2.66)$$

The behaviour of a newly created crystalline lattice structure in a melt depends on its size; it can either grow or remelt, but the process which it undergoes should result in the decrease of the free energy of the particle. The critical size r_{crit} represents the minimum size of a stable nucleus, above which the particle continues to grow because it reduces its free energy. The mean energy of a fluid system at constant temperature and pressure is constant, but locally there are fluctuations around this value. This statistical distribution of energy, or molecular velocity for the molecules constituting the system means that there are regions with a temporarily high energy level where nucleation is favoured. The *rate of nucleation*, J , i.e. the number of nuclei formed per unit time and unit volume, can be expressed as an Arrhenius reaction velocity equation which is commonly used to describe the

rate of thermally activated processes:

$$J = A \exp\left(\frac{-\Delta G_{crit}}{k_B T}\right) \quad (2.67)$$

where k_B is the Boltzmann constant and A is a preexponential constant. To obtain ΔG_{crit} we need Δg_V , which can be expressed as:

$$\Delta g_V = \frac{-\Delta S_{LS}\Delta T}{V_S} = \frac{\Delta H_f(T - T_{mp})}{V_S T_{mp}} \quad (2.68)$$

where ΔS_{LS} is the molar entropy change upon crystallization, V_S is the molar volume of the solid, T_{mp} is the solid-liquid equilibrium temperature, $\Delta T = T - T_{mp}$ is the undercooling and ΔH_f is the latent heat of fusion. The radius of a critical nucleus is then given by:

$$r_{crit} = \frac{-2\gamma_{SL}V_S T_{mp}}{\Delta H_f \Delta T} \propto (\Delta T)^{-1} \quad (2.69)$$

and the rate of nucleation, from equations 2.68, 2.66, and 2.67 is:

$$J = A \exp\left[\frac{-16\pi\gamma_{SL}^3 V_S^2}{3k_B T_{mp} \Delta H_f^2 T_r (\Delta T_r)^2}\right] \quad (2.70)$$

where T_r is the *reduced temperature* defined by $T_r \equiv T/T_{mp}$. Equation 2.70 shows that undercooling is the dominant effect on the nucleation rate ($\Delta G_{crit} \propto (\Delta T)^{-2}$). Nevertheless, classical nucleation theory does qualitatively explain most of the experimental evidence; in many cases the significant deviations can be observed. Melts frequently demonstrate abnormal nucleation characteristics, for instance the rate of nucleation follows an exponential curve only for low values of undercooling but reaches a maximum and subsequently decreases on further cooling. This behaviour was explained by a sharp increase in viscosity with undercooling which restricts molecular movement and inhibits the formation of ordered crystal structures.

2.6.2. Heterogeneous nucleation

It is generally accepted that true homogeneous nucleation is not a common event. Crystallization can be induced by inoculating or seeding a melt with small particles of material to be crystallized. These seed crystals do not necessarily have to consist of the same material to be crystallized in order to be effective; isomorphous substances can also be efficient. As an example, the success of silver iodide as an artificial rain maker is generally attributed to the striking similarity of AgI and ice crystal lattices. However, there are many cases where lattice similarity does not exist and undoubtedly other factors have to be considered.

The overall free energy change associated with the formation of a critical nucleus under heterogeneous conditions $\Delta G'_{crit}$, must be less than the corresponding free energy change, ΔG_{crit} , associated with homogeneous nucleation, i.e.

$$\Delta G'_{crit} = f \Delta G_{crit} \quad (2.71)$$

where the factor f is less than unity.

2. Theoretical background

We can calculate the excess free energy for the heterogeneous nucleation case by assuming a crystal nucleus with a spherical-cap shape, attached to a foreign planar body. The excess free energy, $\Delta G'$, contains, like for the homogeneous case, two contributions: $\Delta G'_I$ and $\Delta G'_V$. The interfacial contribution for heterogeneous nucleation is

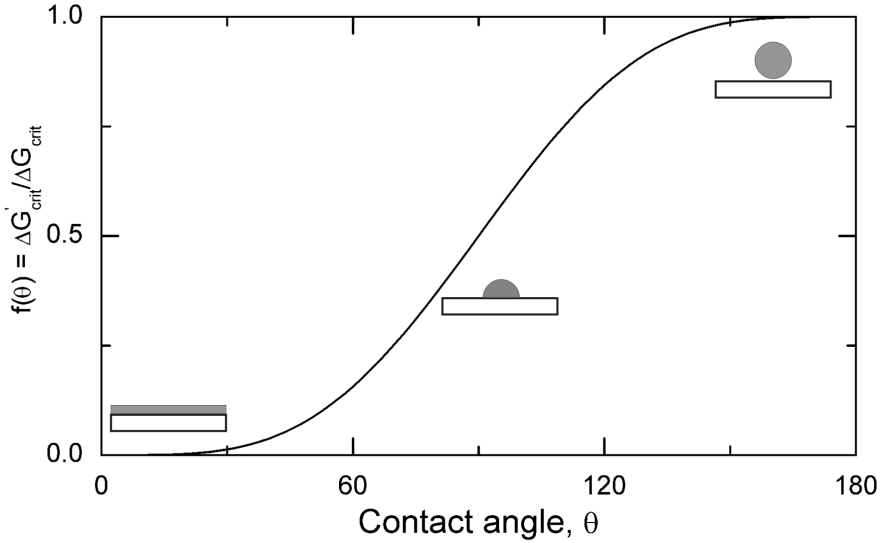


Figure 2.14. Ratio of free energies of homogeneous and heterogeneous nucleation as a function of the contact angle θ .

$$\Delta G'_I = A_{CL}\gamma_{CL} + \pi R^2(\gamma_{CS} - \gamma_{SL}) \quad (2.72)$$

where R is the radius of the contact area between the nucleus and the planar solid surface of the foreign body and A_{CL} is $2\pi r^2(1 - \cos \theta)$, with θ the contact angle and r the radius of the spherical cap. Using the Young equation,

$$\gamma_{SL} = \gamma_{CS} + \gamma_{CL} \cos \theta \quad (2.73)$$

and substituting R with $r \sin \theta$ and $\sin^2 \theta$ with $1 - \cos^2 \theta$ we get

$$\Delta G'_I = 4\pi r^2 \gamma_{CL} \left[\frac{2 - 3 \cos \theta + \cos^3 \theta}{4} \right] \quad (2.74)$$

The spherical cap volume, V_C , multiplied with Δg_V gives the volume contribution to the excess free energy:

$$\Delta G'_V = V_C \Delta g_V = \frac{\pi r^3 [2 - 3 \cos \theta + \cos^3 \theta]}{3} \Delta g_V \quad (2.75)$$

If we now sum up the two contributions, i.e. equations 2.74 and 2.75, the following expression results:

$$\Delta G'_{tot} = \left[\frac{4\pi r^3 \Delta g_V}{3} + 4\pi r^2 \gamma_{CL} \right] \left[\frac{2 - 3 \cos \theta + \cos^3 \theta}{4} \right] \quad (2.76)$$

which compared with equation 2.63 leads to

$$\Delta G'_{tot} = \Delta G_{tot} f(\theta) \quad (2.77)$$

where the factor $f(\theta) = (2 + \cos \theta)(1 - \cos \theta)^2/4$. The equations 2.76 and 2.77 show that the nucleation barrier is smaller in the case of heterogeneous nucleation ($r = r_{crit} = r'_{crit}$, $V_{homo} > V_{hetero}$). In figure 2.14, $f(\theta)$ is plotted against the contact angle, indicating how the excess free energy ratio, $\Delta G'_{crit}/\Delta G_{crit}$ increases when θ varies from 0 to 180° . We find two limiting cases: if θ is zero (complete wetting), there is no barrier for heterogeneous nucleation and, if θ is 180° the barrier has the same value as in the case of homogeneous nucleation.

3. Experimental methods and equipment

3.1. Specular X-ray reflectometry

The investigation of surfaces and interfaces with x-ray and neutron scattering methods is a relatively new field in physics. Technological developments concerning sophisticated surface diffractometers, advancements in manufacturing of high quality and high complexity surfaces and development of the surface scattering theory made the recent progress possible. The surface sensitivity of the method is a consequence of the phenomenon of total external reflection, resulting from the fact that the real part of the refractive index in matter is slightly smaller than unity for x-rays. For the particular cases of liquid surfaces or buried layers, scattering methods have clear advantages over the complementary methods like scanning tunneling (STM), atomic force (AFM) and high resolution transmission electron (TEM) microscopy.

3.1.1. Basic concepts

For small angle X-ray scattering experiments, in the region of total reflection, the detailed locations of the atoms in a medium may be neglected [86]. The properties of the medium can be simply described by the complex refractive index:

$$n = 1 - \delta - i\beta \quad (3.1)$$

where the small, positive term δ accounts for dispersion, and the coefficient of the imaginary part β , for absorption. The classical model of an elastically bound electron yields the following expression of δ and β :

$$\delta = \frac{\lambda^2}{2\pi} r_e \rho_e, \quad (3.2)$$

$$\beta = \frac{\lambda}{4\pi} \mu, \quad (3.3)$$

where r_e is the classical electron radius ($r_e = e^2/4\pi\epsilon_0 mc^2 = 2.81 \cdot 10^{-5} \text{ \AA}$), λ is the wavelength, ρ_e is the electron density of the material (Z electrons per atom), and μ is the linear absorption coefficient. This shows that the real part of the refractive index mainly depends on the electron density of the material and on the wavelength. Typical values for δ are 10^{-5} to 10^{-6} ; β is ten times smaller.

Since the refractive index for x-rays is slightly less than unity, a beam impinging on a flat surface can be totally reflected. The condition for total reflection is that the angle of incidence θ_{in} (between incident ray and surface) must be less than a critical angle. The critical angle, θ_c can be obtained by applying Snell-Descartes' law

$$n_1 \cos \theta_{in} = n_2 \cos \theta_{tr} \quad (3.4)$$

if $\cos \theta_{tr}$ is set to 1. In this case, $\theta_{in} = \theta_c$, and since n_1 is unity (air on one side of the interface), $\cos \theta_c = n_2 = 1 - \delta$ (absorption is neglected). Since δ is of the order of 10^{-5} , after an expansion of the

cosine as $1 - \theta_c^2/2$, one obtains

$$\theta_c^2 \approx 2\delta \quad (3.5)$$

Typical values of the critical angle are in the range 0.2 to 0.5° for $\lambda = 1 \text{ \AA}$ radiation. For silicon and $\lambda = 1.54 \text{ \AA}$ (CuK $_{\alpha}$ radiation) the dispersion term δ is $7.6 \cdot 10^{-6}$, the linear absorption coefficient μ is 141 cm^{-1} and the critical angle $\theta_c = 0.223^\circ$.

The essence of a specular reflectivity experiment is to measure the reflectivity R of a surface as function of the incident angle θ or alternatively as a function of the modulus $q = \frac{4\pi}{\lambda} \sin \theta$ of the wave-vector transfer \mathbf{q} [87]. The reflectivity is defined by the following ratio

$$R = \frac{I_r}{I_{in}}, \quad (3.6)$$

where I_r is the reflected intensity for the corresponding incidence angle θ or wave-vector transfer q and I_{in} is the incident beam (figure A.2). By normalizing the intensity of the incident beam to unity, the experimentally measurable reflected intensity will be the reflectivity, which is the square of the modulus of the reflection coefficient

$$R = |r|^2 = r^* r \quad (3.7)$$

Under the approximation that the electron density can be considered as continuous, the reflection is treated like in optics (more details in section A.2 of the appendix).

3.1.2. Kiessig fringes and Bragg peaks

The Fresnel reflectivity is applied to single uniform substrates. In the case of stratified media or multilayers, scattering from all interfaces has to be considered. If a thin layer, dissimilar to the substrate, is deposited at the interface, the reflectivity profile becomes an oscillating function with periods of oscillations known as *Kiessig fringes*. They are the result of the constructive/destructive interference of the reflected beams from the two interfaces. In figure 3.1 is presented a set of three reflectograms for a layer with a thickness of 40 Å (left graph) and the corresponding $\delta = 1 - n$ versus thickness profile (right graph). The solid and dotted lines correspond to ideally smooth interfaces and two values of the refractive index for the film. The dashed reflectivity profile corresponds to the same refractive index as the solid one but with rms $\sigma_{film/air} = 4 \text{ \AA}$ and $\sigma_{Si/film} = 2 \text{ \AA}$. The oscillation amplitude increases if the contrast between air/film/layer refractive indexes is more pronounced. The main influence of roughness at the interfaces is that the oscillation amplitude decreases with increasing q -values, and that R decays faster with q .

A simple analysis of the Kiessig fringes in a reflectivity profile can allow direct determination of the layer thickness h from the Δq spacing of the minima of two neighboring interference fringes

$$h = \frac{2\pi}{\Delta q} \quad (3.8)$$

More complex data analysis methods can provide further information about the sample, i.e. electron density profile, roughness of interfaces, and more accurate values of the layer thickness. The reflectograms were analyzed with *Parratt32* reflectivity tool software. The calculations are carried out by means of Parratt's dynamical approach [88].

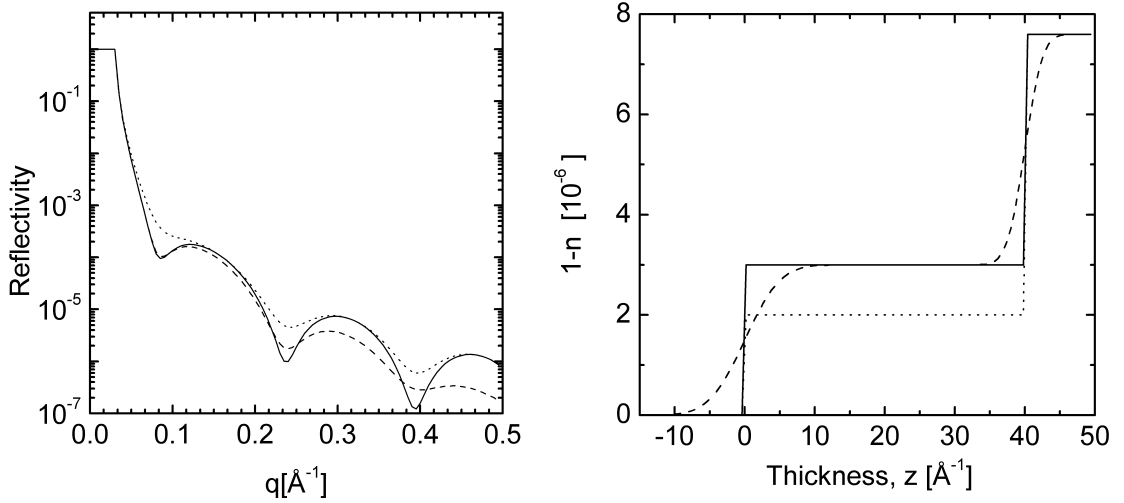


Figure 3.1. Calculated X-ray reflectivity of a 40 \AA thick alkane film on Si substrate (left), and the corresponding refractive index profile along the z direction (right).

If the layered systems consist of many identical repeating units with a thickness h , additional to the Kiessig fringes, Bragg peaks of different orders i can be observed. The position of these peaks is given by the Bragg equation,

$$i\lambda = 2n_2h\sin\theta, \quad i = 1, 2, 3, \dots \quad (3.9)$$

The small angle X-ray reflectivity measurements were performed on a StadiP θ/θ Röntgen reflectometer (StadiP, Stoe & Cie GmbH, Darmstadt). The working parameters were: x-ray tube power supply $U = 30$ kV, $i = 15$ mA, and the divergence of the incoming beam 0.1° . For small angles, the sample width is smaller than the corresponding beam illuminated width. In this case, the measured intensities in the θ range 0 to $\arcsin(w_b/w_s)$ require the so-called "footprint correction",

$$I_{corr} = I_{meas} \frac{w_b}{w_s \sin\theta} \quad (3.10)$$

where w_s is the sample width and w_b is the beam width (slit width).

3.2. Atomic force microscopy

Scanning Probe Microscopy techniques are used to investigate surface structures at very high resolution. One of these techniques, atomic (scanning) force microscopy (AFM, SFM), developed by Binnig et al. [89], is applied for studying the topology of surfaces on the nm scale. The method consists of scanning the surface with a very sharp tip at the end of a cantilever, which probes and maps the morphology of the surface. When the tip approaches the sample surface, interactions like van der Waals, capillary, steric, electrostatic or electromagnetic can be detected [90]. The interaction force between the surface and the tip is detected by the deflection of the cantilever. The cantilever bending is usually detected optically, by directing a laser beam onto the back side surface of the cantilever. The laser beam reflected by the cantilever is detected by a properly positioned, four sector

photodiode. The electrical signals from the photodetector give the actual position of the tip. In most of the cases, piezoelectric tube actuators perform the scanning by moving the sample or the probe over the sample. The basic components of an atomic force microscope are illustrated in Figure 3.2.

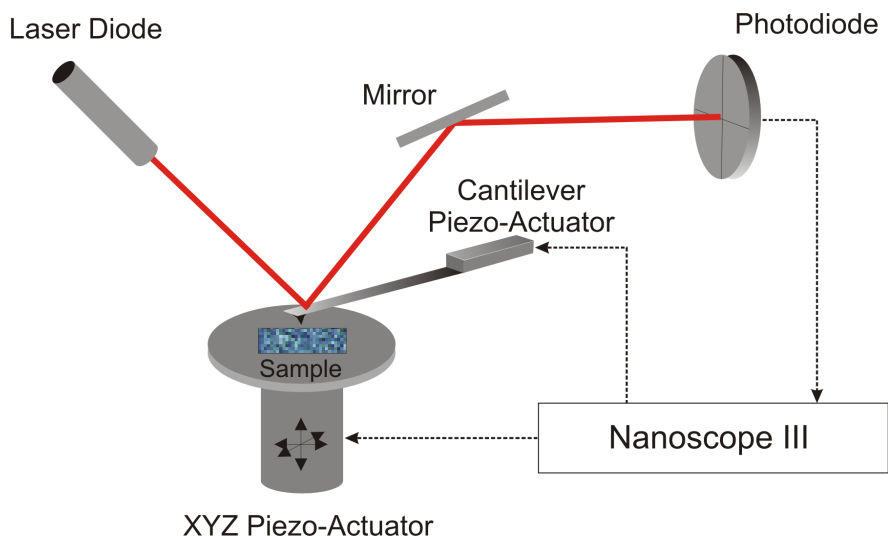


Figure 3.2. Schematic diagram of an atomic force microscope. The arrows represent the electrical connections between the main unit and the photodetector, XYZ piezo-actuator and cantilever piezo-actuator.

AFM imaging can be performed basically in two modes.

In *contact mode*, the tip is in continuous contact with the sample surface. An electronic feedback loop adjusts the probe position in such a way that the interaction force (cantilever deflection) is kept constant (set point). In this way, the acquired image is the probe z-position signal recorded versus the x,y scanning directions (sample plane). The resulting image called height image ideally corresponds to the sample surface topography. In a similar way, lateral forces can be imaged. This scanning method is appropriate for hard (non-deformable) surfaces. The cantilever deflection (the force) originates usually from the repulsive forces in the force-distance curve and this may lead to surface deformations or damage.

For imaging of soft samples a good alternative is the so-called *tapping mode*, also referred to as intermittent contact mode. In this mode, the cantilever is excited to vibrate close to its resonance frequency, usually between 100 to 400 KHz, with a free amplitude in the range of 10 to 150 nm. When the tip approaches the sample surface, the sample-surface interaction force changes the cantilever spring constant. The resulting change in the resonance frequency leads to the attenuation of the oscillation amplitude. The amplitude shift is used as feedback parameter. In this mode the tip is only for a short time in contact with the sample and hence the lateral forces are drastically reduced.

In this work the AFM imaging was performed in air, with a *Nanoscope III* (Digital Instruments, Inc., Santa Barbara, CA).

3.3. Optical microscopy

If a thin, transparent film is deposited on a planar, solid substrate, two interfaces are created, film-air and substrate-film. By illumination with light the two interfaces will reflect part of the light and

the two reflected rays will interfere producing interference colours. For a film characterized by the thickness H and refractive index n , the optical path difference will be given by:

$$\Delta p = 2Hn \sin \theta \quad (3.11)$$

When such a film is illuminated with monochromatic light with the wave length λ , we can have constructive or destructive interference. If i is an integer, constructive interference means

$$\Delta p = (2i) \frac{\lambda}{2} \quad (3.12)$$

while destructive interference is obtained if

$$\Delta p = (2i + 1) \frac{\lambda}{2}. \quad (3.13)$$

By using as substrates silicon wafers covered with a thick oxide layer (e.g. ≈ 292 nm), the image contrast for the observation of molecularly thin alkane layers on top of the oxide layer can be dramatically improved. This fact is based on the interference of rays reflected at the air/SiO₂ (air/alkane) and SiO₂/Si interfaces. In figure 3.3 (a), an incoming ray (1) with the intensity I_1 and amplitude A_1

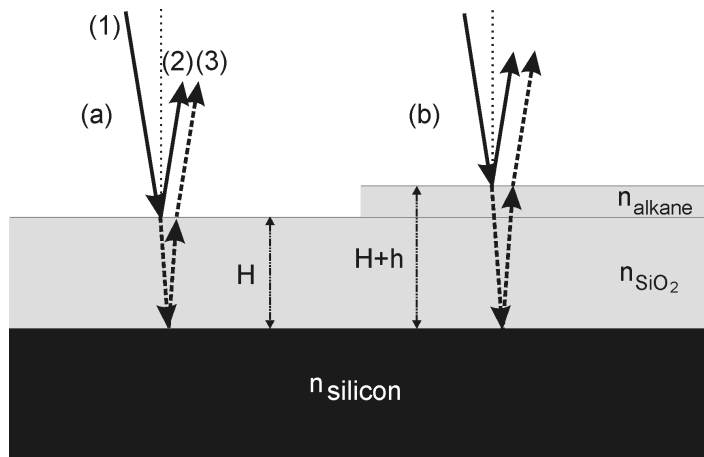


Figure 3.3. Contrast enhancement by using a silicon wafer covered with a thick oxide layer; (a) bare substrate and (b) substrate covered with a molecularly thin alkane layer.

is reflected at the SiO₂/air interface generating the ray (2) with the intensity I_2 and the amplitude A_2 . The refracted part of (1) is reflected at the second interface, SiO₂/Si, and transmitted as ray (3) at the SiO₂/air interface. By neglecting the subsequent reflections/refractions, one can calculate the intensity of outgoing light which results from interference (superimposing) of the two outgoing waves (2) and (3). In 3.3 (b), a molecularly thin alkane layer with the thickness h covers the substrate. One can treat this case in the same way like the bare substrate, under the approximation that the difference in refractive indexes between silicon oxide and alkane is very small, $n_{SiO_2} \approx n_{alkane} \approx n_2$. Thus we can ignore also the reflection at the SiO₂/alkane interface. The relations between the three intensities are

$$I_2 = I_1 R_1 \quad (3.14)$$

and

$$I_3 \approx I_1(1 - R_1)R_2 \quad (3.15)$$

where R_i are the reflectivities of the corresponding interfaces. In equation 3.15 multiple reflections are not considered. For the simplest case (normal incidence), the reflectivities at the two interfaces are given by

$$R_1 = R_{air/SiO_2} = \left(\frac{n_2 - 1}{n_2 + 1} \right)^2 \quad (3.16)$$

$$R_2 = R_{SiO_2/Si} = \left(\frac{n_{Si} - n_2}{n_{Si} + n_2} \right)^2 \quad (3.17)$$

In order to calculate the amplitude of the wave resulting from the interference of the two outgoing waves (2) and (3), we should take into account the phase difference between them. If we regard the amplitudes as vectors or complex numbers we can write

$$\vec{A}_2 = A_2 \cos(\omega t + \phi_2) \quad (3.18)$$

$$\vec{A}_3 = A_3 \cos(\omega t + \phi_3) \quad (3.19)$$

By applying the law of cosines, one can calculate A^2 , the square of the resultant amplitude

$$A^2 = A_2^2 + A_3^2 + 2A_2A_3 \cos(\phi_3 - \phi_2) \quad (3.20)$$

Since both reflections introduce the same phase change (180°) and the optical path difference is given by $\Delta p = 2Hn_2$, the corresponding phase shift will be $\phi_3 - \phi_2 = 2kHn_2$, with $k = 2\pi/\lambda_0$. The reflected intensity can be calculated from equation 3.20 by considering $I = A^2$,

$$I = I_2 + I_3 + 2\sqrt{I_2I_3} \cos(2kHn_2) \quad (3.21)$$

If the second partial derivative of the resulting intensity against thickness is set to zero, i.e. maximum or minimum of $\partial I(H, k, n_2)/\partial H$, one can find the thickness of the silica layer which corresponds to the highest sensitivity to thickness variation:

$$\frac{\partial^2 I}{\partial H^2} = -2(2kn_2)^2 \sqrt{I_2I_3} \cos(2kHn_2) = 0 \quad (3.22)$$

Since for molecularly thin alkane films $h \ll H$, equation 3.22 is appropriate to calculate the SiO_2 thickness values which correspond to maximum sensitivity. In figure 3.4 the function $\cos(2kHn_2)$ is plotted versus thickness of the silicon oxide layer ($n = SiO_2^{550} = 1.46$) and for $\lambda_0 = 550$ nm.

The optical microscopy images were recorded using a *Olympus (Provis) AX-70* (Optical Co. GmbH, Hamburg) research microscope. Two types of light sources were used, tungsten filament lamp (variable intensity) and high pressure Hg lamp. A third (home-made) light source generating pulsed (stroboscopic) light consists of a power LED and was used to improve the time resolution of the recorded image sequence. This illumination mode is described in the section A.3 of the appendix, together with other home-made equipment used in this work. For images recorded by illumination with monochromatic light a green interference filter (LF550) with the peak at 550 nm was used.

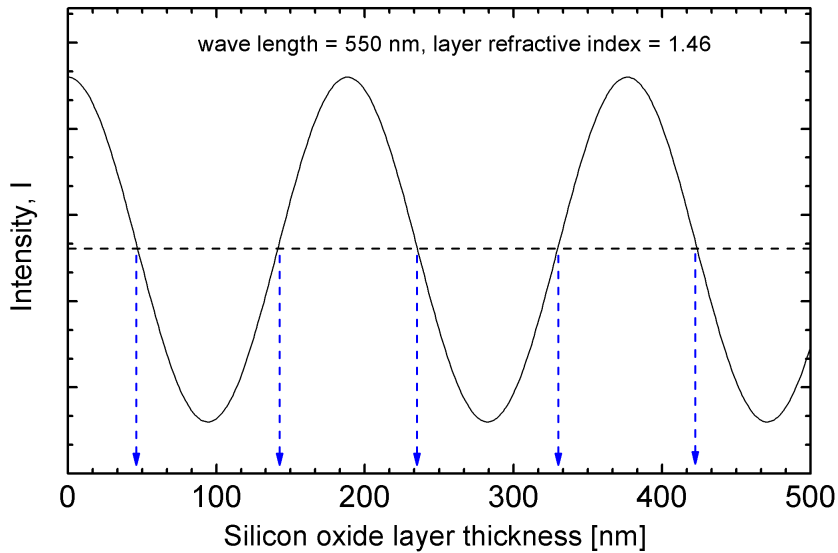


Figure 3.4. Dependence of the reflected intensity versus thickness of the silicon oxide layer. The arrows indicate the thickness of the SiO_2 layer for maximum sensitivity.

Images and movies were acquired with black/white and colour CCD cameras. The black/white camera (TVCCD-460, MonacorTM, Bremen, Germany) has a 1/3" chip with 752(H) x 582(V) resolution, 0.1 Lux minimum illumination, electronic shutter, 1/50 to 1/100000. The colour camera (TVCCD-460COL, MonacorTM) has the same chip dimension and resolution, 1 Lux minimum illumination, electronic shutter in the range of 1/50 to 1/10000. The picture and images were recorded directly in digital format with the FAST AV MasterTM 2000 video acquisition card and processed afterwards. The scale of the acquired images was determined using the 10 μm resolution microscope scale.

4. Materials and sample preparation

4.0.1. Alkanes and substrates

The n-alkanes used in this work were tetracosane (n-C₂₄H₅₀), triacontane (n-C₃₀H₆₂) and hexatriacontane, (n-C₃₆H₇₄). Their melting points are easily accessible experimentally and they have low volatility. They were purchased from Aldrich (purity of 99+%). The alkane solutions were prepared with toluene (purity 99% , Aldrich) with concentrations between 10⁻³ and 10⁻² mol/L. Silicon wafers are ideal substrates for SAXS and AFM: they are characterized by a good electron density contrast ($\rho_{el}^{Si} = 0.7 \text{ e}^-/\text{\AA}^3$ vs. $\rho_{el}^{alkane} = 0.3 \text{ e}^-/\text{\AA}^3$), low roughness (typically $4 \pm 1 \text{ \AA}$) and they are chemically and physically well defined. Two types of monocrystalline Si wafers (cut along the (100) plane, one-side polished, B-doped, with a resistivity of 8.5-11.5 Ωcm) were used: (i) substrates covered with a natural oxide layer ($\sim 15 \text{ \AA}$) and total thickness of $725 \pm 15 \mu\text{m}$, and (ii) substrates covered with thick oxide layer ($\approx 2920 \text{ \AA}$). For measurements, the wafers were cut to pieces of 20 mm x 15 mm.

Besides silicon wafers, glass slides (designed for optical microscopy) and mica glued onto glass slides were used as substrates. The mica surface is crystalline and atomically flat. When freshly cleaved, it has a high energy surface and therefore has to be used immediately.

Cleaning procedure and sample preparation

For the cleaning of the silicon and glass substrates, a modified RCA cleaning procedure was used [91–94]. The cleaning procedure consists of two steps: a precleaning step, 10 min at 40°C in a water:2-propanol 1:1 mixture and subsequently, a main cleaning step, for 10 min, at 75° in a 1:1:5 solution mixture of NH₄OH:H₂O₂:pure water (30% ammonium hydroxide, 99,99% purity, Aldrich and 35% hydrogen peroxide "medically pure", Merck). The ultrapure water (resistivity $\approx 18 \text{ M}\Omega \text{ cm}$) was produced with a Seradest USF machine (Seral Company). Subsequently, the substrates were washed in a flow of pure water for 10 min and stored under the same liquid to prevent contamination. Prepared in this way, silicon and glass substrates are completely wetted by water. All the experiments were performed with freshly prepared substrates, i.e. no more than 24 h after they have been cleaned.

Before alkane deposition the substrates were dried in a flow of pure nitrogen. A spin-coating machine (1-EC101DT-R485, Headway Research Inc., Garland, Texas, USA) was used for deposition of alkanes from solution. In order to achieve different alkane coverages, both the rotational speed (1000 to 6000 rpm) and the concentration (10⁻³ to 10⁻² mol/L) were varied. Typically one drop of solution was used to obtain the desired coverage (obviously most of the solution is spun off in the course of spin coating).

After alkane deposition, in most of the cases, the samples were heated to 10°C above the melting point to ensure reproducibility of the experimental results.

5. Droplet solidification by growing molecularly thin terraces

5.1. Introduction

Liquids on solid surfaces in thermodynamic equilibrium either form drops with a well-defined contact angle (partial wetting) or cover the surface as a continuous film (complete wetting). Drops on surfaces are, however, often not in their equilibrium conformation. The behaviour of the macroscopic properties characterizing spreading drops, e. g. radius of the macroscopic liquid edge, the height, the profile, and the contact angle, are described empirically by the Tanner laws [8, 9], which were originally deduced from hydrodynamic equations. At microscopic scale, in the case of complete wetting ($S > 0$), a spreading drop has supposedly a thin liquid film (precursor) which precedes the macroscopic liquid edge. Ellipsometric measurements [21, 23, 25] indicate that the lateral dimension of the film grows with $R \propto \sqrt{time}$, irrespective of the nature of the species involved.

The wetting behaviour of long chain alkanes, in the temperature range around the bulk melting point is shown in figure 5.1. Starting from about 10°C above the melting point (a), where a complete wetting film can be observed, on cooling the system passes through different reversible wetting states. At about $T_{DW} \approx T_{SF} \approx T_{mp} + 3^\circ\text{C}$ (DW - dewetting, SF - surface freezing) a dewetting transition occurs. This leads to an uniform, compact and well defined surface frozen layer and partially wetting droplets on top (b). Below the bulk melting point, the partially wetting droplets are metastable and tend to solidify. The solidification behaviour depends on the extent of undercooling and on the cooling rate. Thus, a cooling rate of $\approx 0.5^\circ\text{C/s}$, from above the melting point to room temperature, (path (1) in the figure), leads to the topology (d), which consists mostly of solidified (amorphous) droplets on top of the surface frozen layer. If the partially wetting drops are subject to only few degrees undercooling (path (2)) they can solidify continuously by growing concentric, solid, circular multilayer terraces on the surface, topology (d). Path (3) corresponds to a very fast cooling, e.g. $\approx 100^\circ\text{C/s}$, when the cooling process is faster than the dewetting process. Such temperature treatment leads to a solid replica (vitreous or polycrystalline state) of the completely wetting liquid.

This chapter describes the growth of solid terraces from undercooled drops according to the second path in figure 5.1. The experimental results show that the growth of the solid mono/multilayers terraces is supplied by a diffusive flow of alkane in a precursor-like film on top of the terraces, between the droplet perimeter and the terrace edge. In the following will be presented first the various nucleation processes which can lead to either terrace growth or bulk solidification. Then, the structure of the solid terrace will be discussed and finally the transport in the precursor film will be analyzed.

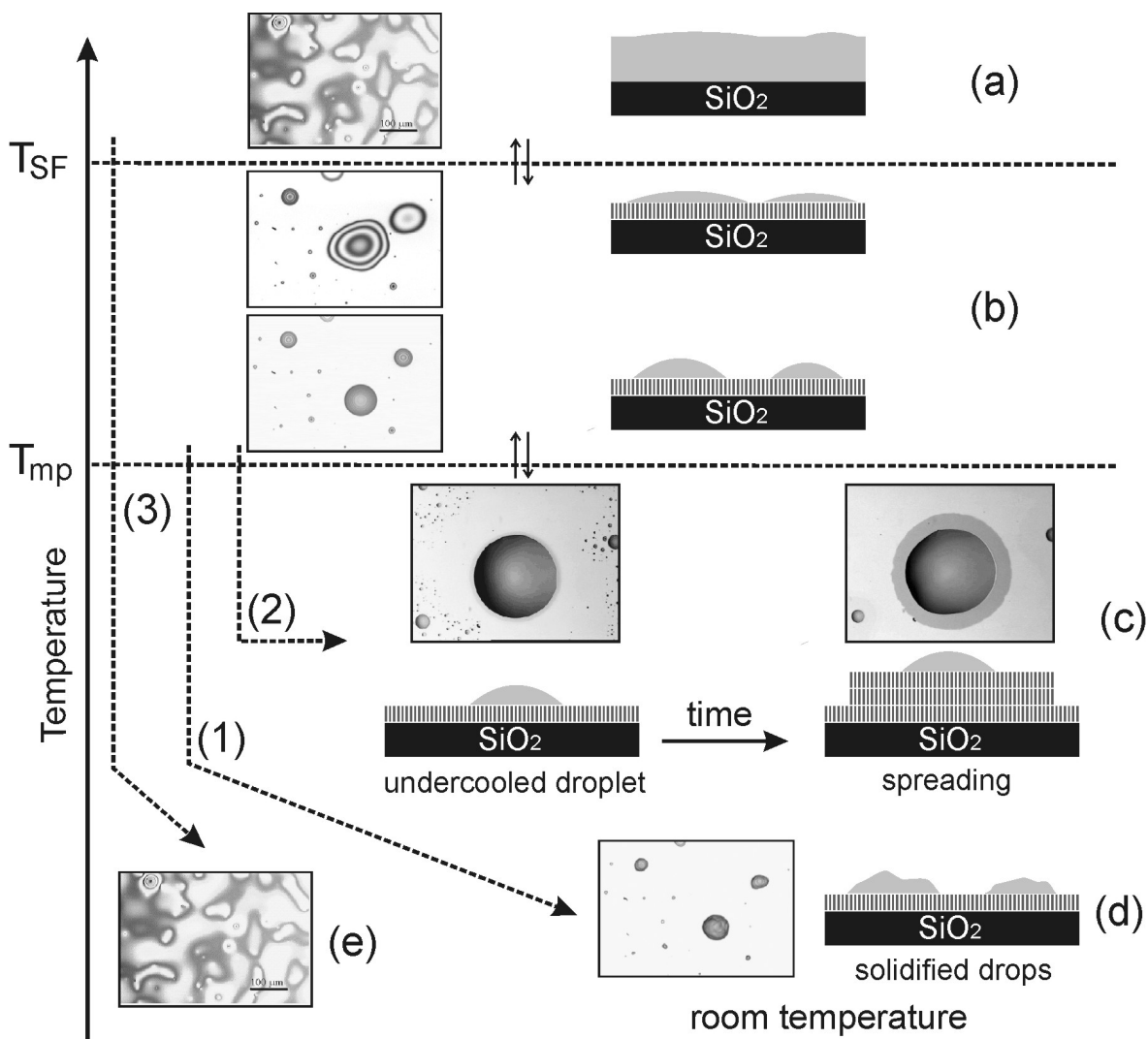


Figure 5.1. Temperature dependence of wetting behaviour of C_{30} at Si/SiO_2 interface: (a) complete wetting, (b) partial wetting, (c) terrace growth from undercooled droplets (d) solidified drops, (e) "completely wetting", amorphous solidified film resulting when cooling is faster than dewetting.

5.2. Nucleation of bulk solidification and terrace growth

Undercooled, partially wetting alkane drops (contact angle $\approx 15^\circ$) on a planar Si/SiO₂ substrate can solidify either completely (at once, in 3D), when the entire liquid drop transforms into a polycrystalline "drop". Alternatively they can solidify continuously (2D), creating circular, well-defined, molecularly thin solid terraces. These two solidification mechanisms do not start instantaneously as soon as the temperature is below T_{mp} ; undercooling and time is needed in order to overcome the nucleation barrier. A systematic study of the droplet behaviour reveals that, at small undercooling temperatures, the nucleation leads, in most of the cases, to the formation of discrete (mono)molecular solid layers with the molecular axis oriented perpendicular to the surface plane. Thicker terraces (thickness \approx multiple of all-trans length of the molecule) are created by a sequence of nucleation events, each of them followed by the growth of monomolecular layers. In this way, starting from the three-phase contact line, layer-by-layer growth leads to the formation of thick terraces. Although less likely, multilayered terraces can also result from a single nucleation event.

Three types of nucleation were observed in the temperature range between T_{mp} and $T_{mp} - 6^\circ\text{C}$: (i) "homogeneous" (spontaneous nucleation), (ii) heterogeneous (caused by impurities, dust particles, surface defects), and (iii) secondary nucleation, induced by a growing terrace front from a neighbouring drop. Deeper undercooling ($\Delta T \equiv T - T_{mp}$ larger than -6°C) promotes the 3D solidification of the entire drop rather than 2D nucleation of growing solid terraces. The terminology used here to describe the nucleation of terrace growth (2D) is obviously not strictly correct, since it is not really homogeneous because both, S/L and L/V interfaces are present. In the following, the term "homogeneous" means that the solidification is not initiated by either solid impurities (inside or outside the drop) or solid fronts approaching the contact line.

Homogeneous (spontaneous) nucleation

Homogeneous nucleation may occur either inside the drop, at S(surface frozen)/L interface or at the contact line. It is still under investigation which of the two processes prevails.

Secondary nucleation

Secondary (induced) nucleation is the most important mechanism for initiating the growth of terraces. It (always) occurs when a growing solid front approaches the contact line of a droplet without terrace.

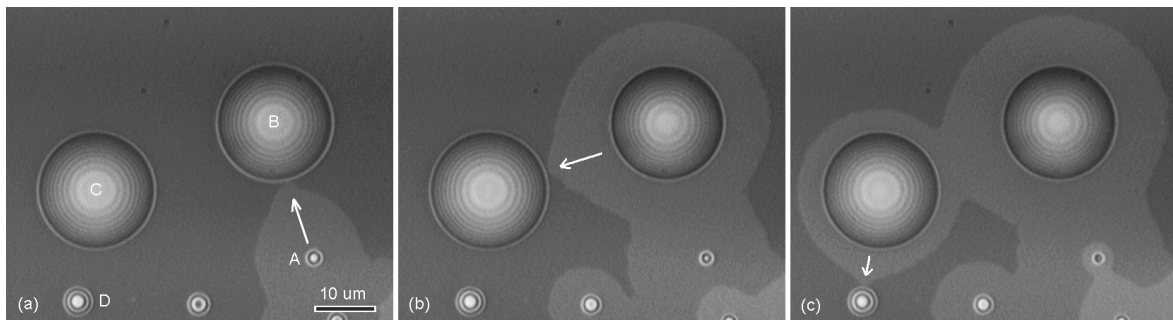


Figure 5.2. Drop-to-drop nucleation of terrace growth (C₃₆, at two degrees below T_{mp}). One monolayer thick solid terrace grows on the surface from drop A to the initially non-growing drops B, C, and D.

When the distance is small enough, the liquid drop starts forming a solid terrace from the point of smallest distance between the approaching terrace and its contact line. This freshly formed solid terrace propagates fast (within less than 1 second) all-around the drop and forms a ring of solid terrace. Thus, a drop-to-drop propagation of the growing front (a kind of "domino effect") can initiate terrace growing from many drops. The sequence of optical microscopy images in figure 5.2 shows the mechanism of induced nucleation. In image (a), the droplet A is already growing its terrace and B is just before its nucleation. The contour of the terrace surrounding droplet A is not circular because its growing front moved faster along the direction connecting its center and the center of droplet B. This can be explained by the increased supply of solidifying alkane along that direction, i.e. because the flux of molecules comes not only from A but also from B. In image (b), the front coming from B is just about to trigger the terrace growth of drop C and in (c) the droplet C initiates the growth of D. As a general rule it is observed that by this mechanism, the thickness of a freshly nucleated growing terrace can not exceed the thickness of the one which nucleated it.

Heterogeneous nucleation

Dust particles or defects in the structure of the solid surface can promote heterogeneous nucleation even outside the drop. This is presented in figure 5.3. The first image shows a dust particle (the circle indicates its position) near a "big" drop of C_{36} , at three degrees under T_{mp} . In the second image (after ≈ 4 min) a monomolecular terrace starts to grow from the dust particle. Its growth is directed towards the drop, as one can observe in images (3) and (4). Images (5) and (6) show the growth of a circular terrace around the drop, after the growing front "touched" (secondary nucleation) the contact line of the drop.

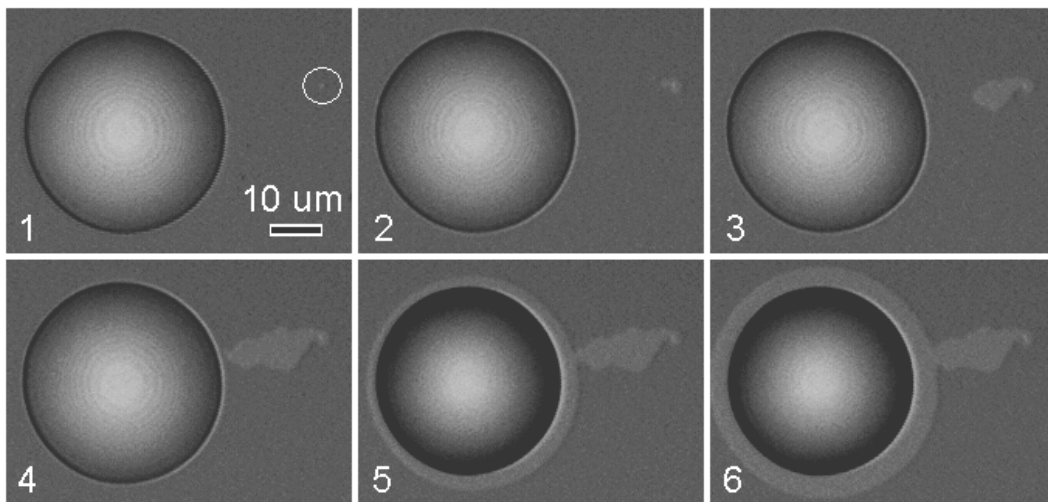


Figure 5.3. Heterogeneous nucleation at three degrees below T_{mp} : a dust particle (the circle indicates its position) near an undercooled drop of C_{36} (1); (2) - (4) directed growth of a newly formed solid terrace towards the drop; (5) and (6) radial terrace growth around the drop after the front "touched" its contact line.

Figure 5.4 presents possible topologies for: (a) drop-to-drop induction of the solid terrace growth, and (b) dust-induced nucleation. In the first cartoon, the terrace is supposed to be present under drop A and to advance under drop B after reaching its contact line. This supposition is based on the fact

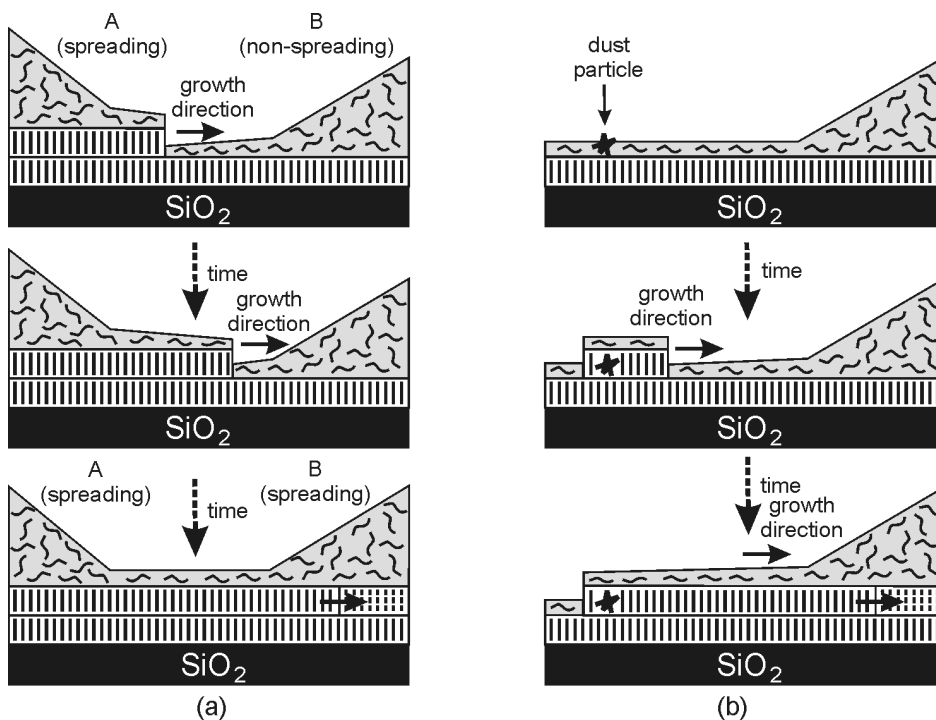


Figure 5.4. Suggested topology during induced nucleation (a), and heterogeneous nucleation (b).

that a solidifying front has enough liquid available as soon as it "touched" the contact line of an undercooled drop. The liquid molecules are most probably transported via a "liquid-like", molecularly thin film (thinner than the all-trans length of the molecule) on top of the terraces (experimental evidence supporting this scenario will be presented in the following sections). Qualitatively, it was observed that the nucleation barrier for terrace growth decreases on increasing the substrate roughness, i.e. on decreasing temperature, the growth starts at $\approx T_{mp}$. In these conditions, terraced structures were also observed (see the AFM images in figure 5.5).

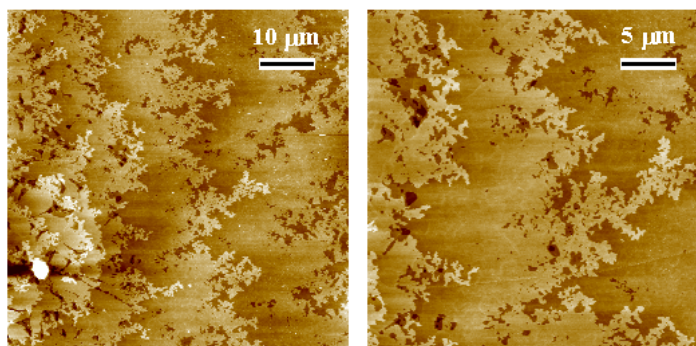


Figure 5.5. AFM images showing terraced structures with "diffuse" edges, which grew on a rough substrate surface.

5.3. Structure and thickness of the growing film

Optical microscopy, AFM and X-ray reflectivity measurements indicate that the structure of the terraces growing from undercooled drops is an ordered, mono/multilayered solid.

5.3.1. Optical microscopy and AFM

One can observe that the brightness of the regions covered by the growing film is uniform (see figures 5.2 and 5.3). This suggests that the thickness of the film during growth is constant and its edge is sharp.

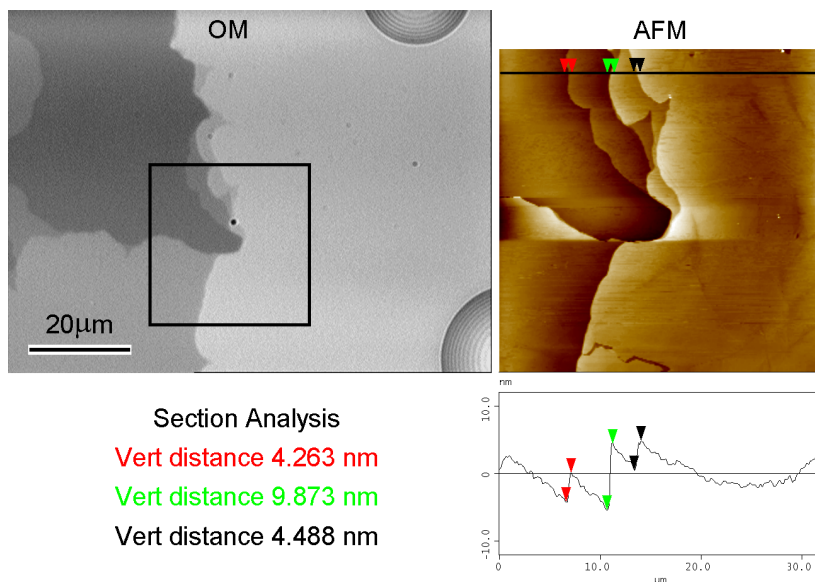


Figure 5.6. Comparison between OM and AFM images (room temperature) of the same sample area after terraced growth of C_{36} films. The section analysis shows discrete steps at the edge with the heights multiples of the all-trans length of the molecule. In the section analysis, the continuous height variation on top of the plateaus is an artifact of the AFM machine due to some drift when large areas are scanned.

Figure 5.6 compares optical microscopy (OM) and AFM images of the same sample area. Thus, it is possible to attribute to each brightness value the corresponding film thickness. The section analysis of the AFM images proves that: (i) the film consists of plateaus with constant thickness separated by sharp steps (terraced structure) (ii) within the accuracy of the method, the height of the steps at the terrace edge is a multiple of the all-trans length of the corresponding alkane.

5.3.2. Small-angle X-ray reflectivity data

Kiessig fringes

C_{30} samples prepared by spin-coating from toluene solution were heated at 10°C above T_{mp} and then cooled to 3° below T_{mp} . At this temperature they were kept for 3h in order to obtain solid terraces as a result of the process of terrace growth. The mean alkane coverage was adjusted by preparation to two and three monomolecular layers. The samples were measured by SAXR at the terrace growth

temperature. The results are presented in the reflectograms (a) and (b) of figure 5.7. The fitting curves (red points) correspond to the best fit assuming an uniform (complete) layer of constant thickness. The values of δ and β (the two components of the complex refractive index) for SiO_2 and $(\text{CH}_2)_x$ were taken from [95]. The fitting results are: $H(\text{thickness}) = 80.8 \text{ \AA} (\approx 2\text{ML})$, $\sigma_{\text{SiO}_2/\text{alk}}(\text{roughness}) = 1.9 \text{ \AA}$, $\sigma_{\text{alk}/\text{air}} = 4.9 \text{ \AA}$ for sample (a) and $H = 118.9 \text{ \AA} (\approx 3\text{ML})$, $\sigma_{\text{SiO}_2/\text{alk}} = 2.9 \text{ \AA}$, $\sigma_{\text{alk}/\text{air}} = 5.7 \text{ \AA}$ for sample (b). The difference between the experimental data and fitting curves is a consequence of the fact that the layered structure is not perfectly continuous (the substrate is covered by uniform solid films whose thicknesses differ by the all-trans length of a C_{30} molecule). Such structures are schematically presented in figure 5.8. The results prove that the structures resulting from terrace growth have, at least locally, uniform thickness.

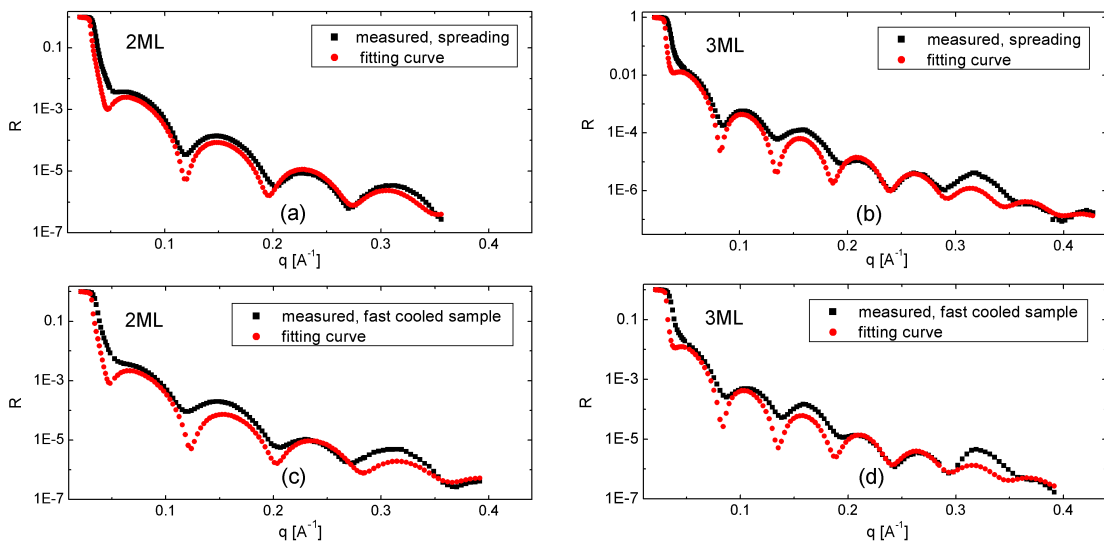


Figure 5.7. SAXR experimental data and the corresponding fitting curves for samples with different C_{30} coverages prepared by terrace growth - (a) and (b), and very fast cooling ($\approx 100^\circ\text{C/s}$) - (c) and (d).

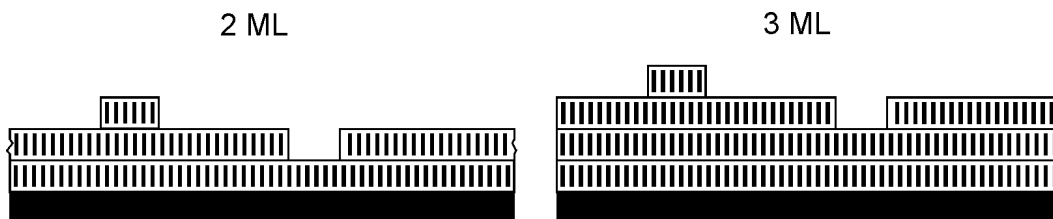


Figure 5.8. Possible topologies of the solid films corresponding to the samples (a), $\approx 2\text{ML}$, and (b), $\approx 3\text{ML}$.

Similar results (reflectograms (c) and (d) in the figure 5.7) are obtained when samples with the same mean coverage as the previous ones are cooled very fast ($\approx 100^\circ\text{C/s}$) from temperatures corresponding to a completely wetting film to room temperature (path (3) in figure 5.1). The measurements were performed at room temperature after few minutes of annealing at 3°C below T_{mp} . The fitting curves correspond to $H(\text{thickness}) = 78.2 \text{ \AA} (\approx 2\text{ML})$, $\sigma_{\text{SiO}_2/\text{alk}}(\text{roughness}) = 1.8 \text{ \AA}$, $\sigma_{\text{alk}/\text{air}} = 5 \text{ \AA}$ for sample (c) and $H(\text{thickness}) = 118.1 \text{ \AA} (\approx 3\text{ML})$, $\sigma_{\text{SiO}_2/\text{alk}}(\text{roughness}) = 2.3 \text{ \AA}$, $\sigma_{\text{alk}/\text{air}} = 5.9 \text{ \AA}$ for sample (d). At this cooling rate, the dewetting process does not occur and the resulting struc-

tures consist of disordered solids in the "completely wetting" regime. These results indicate that even in solid, disordered state, the alkane molecules have a strong tendency to form lamellae structures oriented parallel to the sample plane.

Bragg peaks

By terrace growth it is not possible to obtain, within reasonable time, "thick" solid terraces (more than 3ML) covering large areas of the substrate. However, using the very fast cooling method such structures can be produced. Figure 5.9 shows the AFM section analysis of a sample prepared in this manner, indicating a solid film thickness of about 5-6 ML.

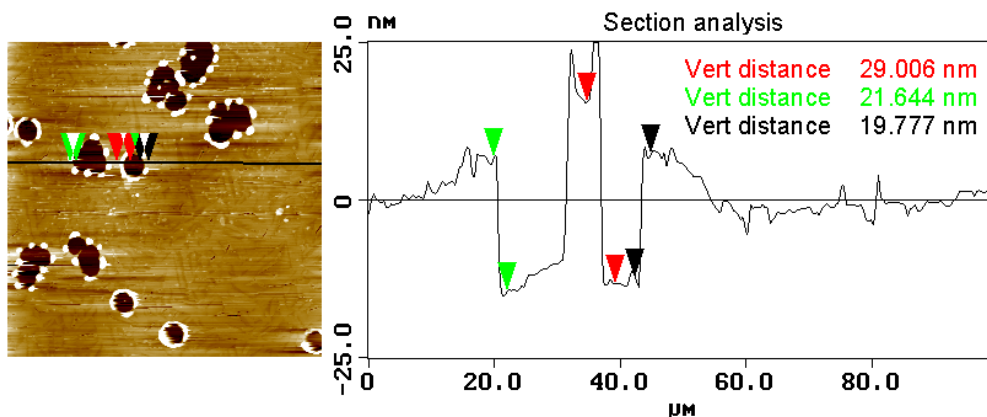


Figure 5.9. AFM image of a C_{30} sample which was cooled at a rate of $\approx 100^\circ\text{C}/\text{s}$. The section analysis is performed in a region with holes formed by dewetting (stopped in its early stages due to the high cooling rate).

The graph in figure 5.10 presents the SAXR scans from the sample whose AFM image is presented in figure 5.9.

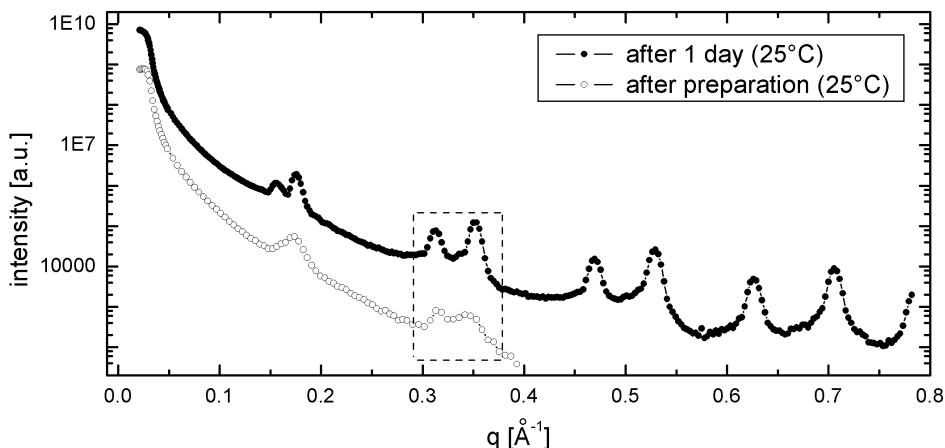


Figure 5.10. Reflectograms of the sample presented in figure 5.9, measured at 25°C immediately after preparation (open circles), and after 24h (full circles).

The open circles in figure 5.10 correspond to the measurement immediately after preparation (at room temperature). The presence of the first and second order Bragg reflections indicate a layered

solid with the same repeat unit. The first order reflection consists of a broad peak while the second order one consists of two overlapping peaks. The scan after 24h (full circles) is shown in the same figure. In this case, one can observe two distinct Bragg peaks for both first and second order reflections. This indicates that, by annealing at room temperature, the structure becomes more ordered (layered) and that two structures with different layer spacing coexist.

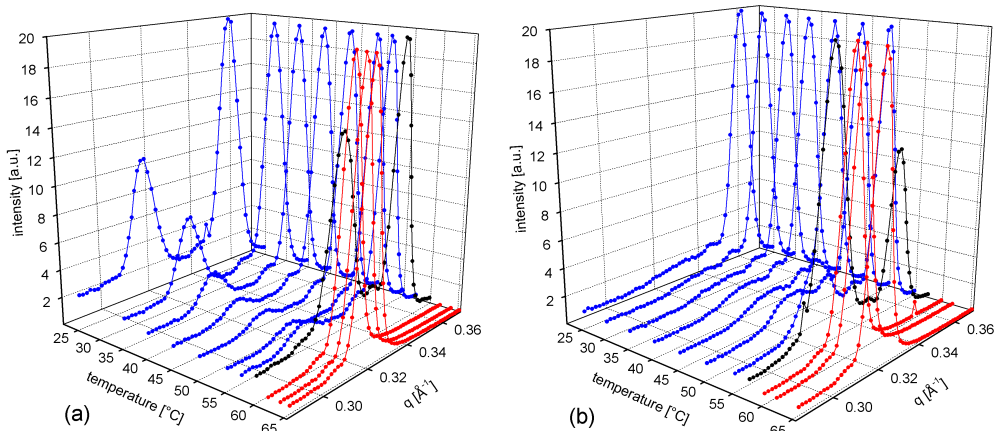


Figure 5.11. The second order Bragg peaks of the reflectogram presented in figure 5.10 on (a) increasing temperature, and (b) decreasing temperature.

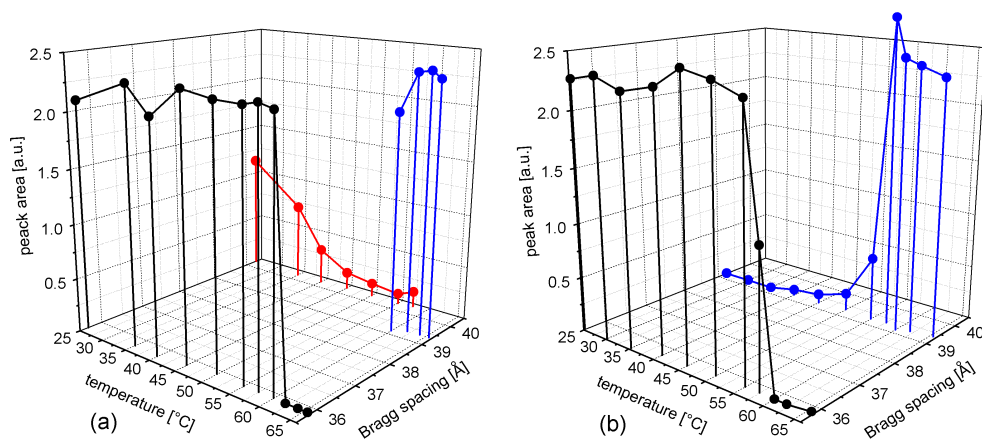


Figure 5.12. Same data as in figure 5.11 plotted as peak area vs. Bragg spacing at different temperatures.

Subsequently, the two peaks of the second order Bragg reflection were selected for a temperature scan. The results (intensity vs. temperature and q) are presented in figure 5.11. The time interval between two scans was ≈ 15 min. The same data are also represented in figure 5.12 as peak area (estimated by triangulation) vs. temperature plus the corresponding Bragg spacings, calculated from the positions of the peak maxima. The graphs (a) and (b) in the two figures correspond to increasing and decreasing temperature, respectively.

On increasing temperature, two phases are present in the temperature range 25 to 60°C. The phase with a Bragg spacing of ≈ 35.8 Å corresponds to the monoclinic crystalline phase of bulk even-numbered alkanes which is well described in the literature [49]. The Bragg spacing of the second

crystalline phase is $\approx 40.3 \text{ \AA}$ (\approx all-trans length of the C_{30} molecule) which corresponds to a perpendicular orientation of the molecules with respect to the layer plane. A similar phase coexistence was observed by Mo et al. [96], in the case of C_{32} films with the "ellipsometric" thicknesses of 99 \AA and 153 \AA . They suggested that the phase characterized by the longer spacing is stabilized by the presence of the substrate surface. Between 60 and 65.5°C the Bragg spacing is $\approx 39.3 \text{ \AA}$ which corresponds roughly to both RIII (triclinic) and RIV (monoclinic) rotator phases of bulk C_{30} which are well described in the literature [64].

On cooling, the behaviour is reversible except the missing reflection corresponding to $\approx 40.3 \text{ \AA}$. This suggests that the phase with the Bragg spacing of $\approx 40.3 \text{ \AA}$ is either a metastable crystalline phase or a long equilibration time is needed for its formation.

These SAXR results indicate that the solid films resulting from either growth of terraces from undercooled drops or fast cooling of a completely wetting liquid film are ordered, layered structures. At temperatures above $\approx 60^\circ\text{C}$, the alkane molecules are perpendicularly oriented with respect to the sample plane.

5.4. Equations describing the kinetics of terrace growth

The sequence of OM images presented in figure 5.13 shows the typical time evolution of a growing terrace. Assuming a spherical cap geometry, the droplets can be fully described by their in-plane radius (denoted in the following by R_1) and their contact angle θ . On the other hand, for the circular terrace surrounding the drop, the relevant parameters are its thickness H and the distance from the center of the drop to the circular growing front (denoted by R_2). This parametrization is shown in figure A.5 of the appendix. Large drops barely decrease their volume during terrace growth. This

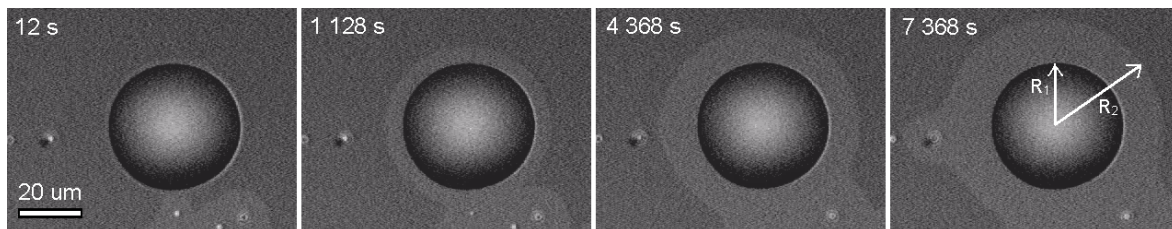


Figure 5.13. Terrace growth from the three-phase contact line of a "large" C_{30} drop at 1°C below T_{mp} .

is because the film thickness is much smaller (for instance $\approx 4\text{nm}$ per monolayer of C_{30} alkane) compared with the droplet height (usually in the order of microns). Thus, for large drops, R_1 can be considered constant during the growing process. However, in the case of small droplets, the variation of R_1 cannot be neglected and very small ones disappear completely (see, for instance the two drops in the lower part of the images presented in figure 5.13).

The kinetics of growth from the droplet presented in figure 5.13 is shown in the two graphs of figure 5.14. Since in this case R_1 can be considered constant, R_2 and $(R_2 - R_1)$ were chosen as parameters describing the position of the growing front. In section A.4 of the appendix different speed-limiting steps of the growing process (release-limited, transport limited and growth limited) are considered and their corresponding equations are deduced for both linear and circular growing geometry. In graph (a) of figure 5.14, one can observe that only $\log(R_2 - R_1)$ is a linear function of $\log(\text{time})$. The corresponding slope is ≈ 0.5 which allows us to consider $(R_2 - R_1)^2 \propto (\text{time})$, the proper equation

describing the terrace growth process (see the linear time dependence in graph (b) of figure 5.14). Although in theory the proportionality $(R_2 - R_1)^2 \propto (\text{time})$ is not exact for a circular geometry, for short growing times i.e. small $(R_2 - R_1)/R_2$, it is quite a good approximation.

A linear time dependence of the difference between the two squared radii would correspond to a release-limited flow¹ of alkane molecules supplying the growth. Graph (b) in figure 5.14 proves that the growth does not correspond to a release-limited process. Both (a) and (b) graphs prove that, for our circular geometry, the growth of terraces from undercooled drops is transport-limited and diffusive in nature. Therefore, an *apparent diffusion coefficient*, defined by the equation:

$$D_{app} = \frac{(R_2 - R_1)^2}{t} = \frac{d[(R_2 - R_1)^2]}{dt} \quad (5.1)$$

will be used in the following as a measure of how fast the terraces grow.

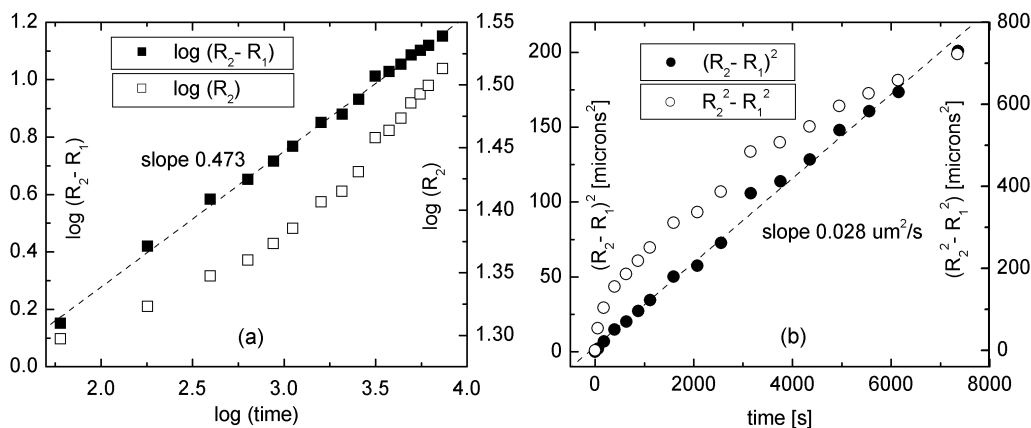


Figure 5.14. Time dependence of both the terrace radius R_2 and the terrace width $R_2 - R_1$: (a) double-logarithmic plot and (b) $(R_2 - R_1)^2$ and $(R_2^2 - R_1^2)$ vs. time.

The supply of material which feeds the solidification front of a terrace comes not only from its "own" drop but also from the neighbouring ones (see the figure 5.2 where the circular shape is distorted towards neighbouring drops). The droplets which were used to analyze the growth kinetics were selected as much as possible to fulfill the conditions: (i) to be far enough from the neighbouring drops which do not build terraces (non-nucleated ones), and (ii) to have R_1 larger than $10 \mu\text{m}$ i.e. to justify the neglect of the volume decrease of the drop upon terrace growth. In most of the cases the nucleation happened by induction. This does not influence the kinetics of terrace growth of the droplet of interest since a "foreign" drop which builds terraces, (mainly) supplies its own growing terrace. Regions where the growing terrace formed bulges were discarded from the data analysis.

The alkanes C_{30} and C_{36} can be considered non-volatile in 3D for the time scale of a typical experiment. This was proven experimentally by the following: (i) even small drops (which are not growing terraces), do not change significantly their R_1 when kept for hours at temperatures close to T_{mp} (ii) for all-solid structures (solidified drops and terraces) there is no detectable change in the position of the terrace steps for the same time scale. C_{24} can be considered slightly volatile: (i)

¹The growth of solid terraces from the contact line of undercooled drops can be viewed as a spreading process since it is supplied by a flux of material coming from undercooled drops.

in the final stages of terrace growth, holes in the solid film can be observed (probably due to 3D evaporation/sublimation), and (ii) the kinetics of growth follows a power law $(R_2 - R_1)^n \propto (\text{time})$ with a temperature dependent exponent (for instance $n = 0.31$ at 4°C undercooling, $n = 0.28$ at 3°C undercooling, $n = 0.19$ at 2°C undercooling).

5.5. Kinetics of sequential growth of monomolecular terraces at constant temperature

Thick terraces form usually by monomolecular layer-by-layer growth. As soon as a new layer starts growing, the previous layer stops its growth² because the entire supply from the central drop is taken by the newly growing one.

5.5.1. Growth of the second terrace on top of the first one

Figure 5.15 presents the sequential growth of two C_{30} monomolecular terraces on top of each other, at two degrees below T_{mp} . At 0 s, the growth of the first terrace is nucleated by the growing front of another drop (not in the image). Note that the terrace whose growing front induces the nucleation had initially a thickness of two monolayers. On approaching the drop whose terrace is not yet nucleated, the growing front splits into a slower one (on top) and a faster one. This leads to two distinct secondary nucleation events followed by the observed growth sequence. The first terrace grows (72 s), reaching at 264 s a width of $\approx 5 \mu\text{m}$, and stops as soon as the second terrace is nucleated. The snap-shots at 348 s and 432 s present the growth of the second terrace before reaching the edge of the first one which does not grow anymore. At about 600s, when the second terrace reaches the edge of the first one, they both continue to grow together reaching at 2184 s a width of $\approx 9 \mu\text{m}$.

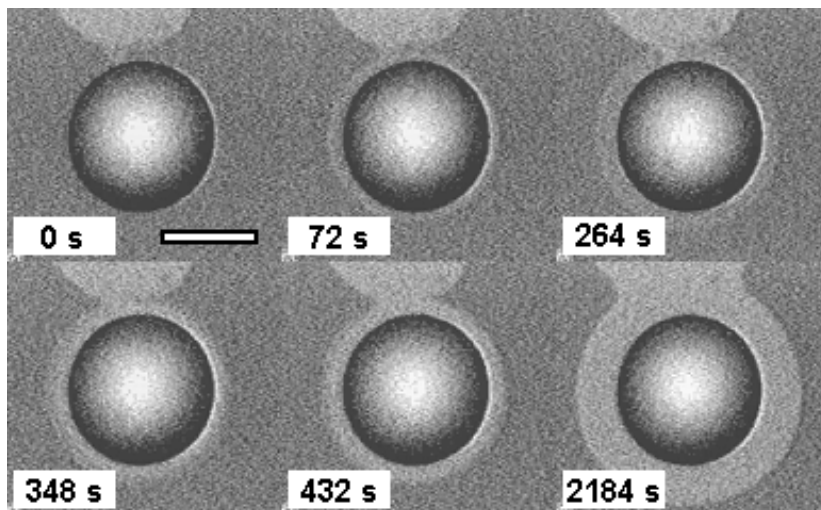


Figure 5.15. Growth of C_{30} mono- and bilayer terraces at 2.0°C undercooling, bar = $20 \mu\text{m}$.

The kinetics of terrace growth shown in figure 5.15 is presented in figure 5.16, graph (a).

²This is not entirely correct since the growth can be supplied from neighbouring "foreign" drops which do not build terraces.

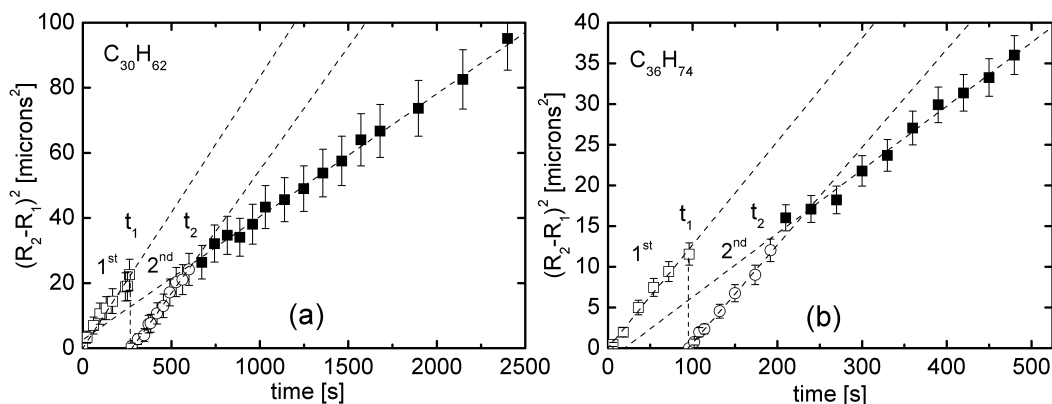


Figure 5.16. Growth kinetics of a monolayer terrace followed by a second monolayer on top: (a) C_{30} at 2.0°C undercooling and (b) C_{36} at 1.5°C undercooling.

The slopes calculated from the linear fit are for the first layer $D_{app}^{1st} \approx 0.075 \mu\text{m}^2/\text{s}$, and for the second, before reaching the edge of the first one, $D_{app}^{2nd} \approx 0.076 \mu\text{m}^2/\text{s}$. When they grow together as a double-layer, the slope is $D_{app}^{both} \approx 0.038 \mu\text{m}^2/\text{s}$, about half of the value for one molecular layer. Graph (b) of figure 5.16 describes a similar experiment, with C_{36} at 1.5°C below the bulk melting point. The corresponding slopes are $D_{app}^{1st} \approx 0.13 \mu\text{m}^2/\text{s}$, $D_{app}^{2nd} \approx 0.12 \mu\text{m}^2/\text{s}$, and $D_{app}^{both} \approx 0.078 \mu\text{m}^2/\text{s}$. Within the experimental error, these results indicate a slope ratio $D_{app}^{1st} : D_{app}^{2nd} : D_{app}^{both}$ is 2 : 2 : 1, i.e. the flow supplying the growth is independent from the thickness of the terrace. This suggests a scenario presented in figure 5.17 and discussed in further detail below.

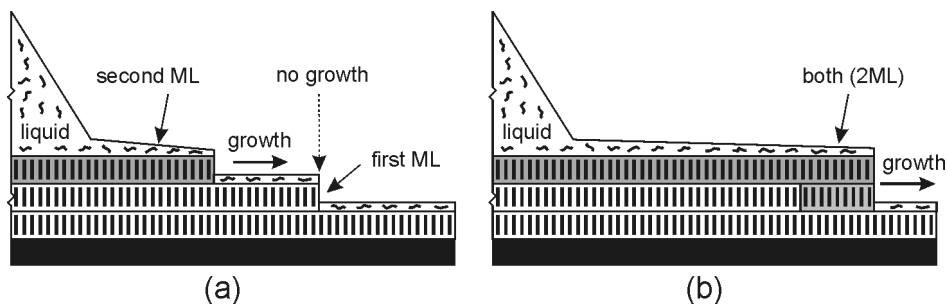


Figure 5.17. Schematic cartoon showing the growth of a second terrace on top of the one which has grown before: 1ML growing (a), and the two layers growing together (b). The scenario suggests the presence of a film of mobile molecules on top of the terrace supplying the growth at the terrace edge.

Possible transport mechanisms are summarized in table 5.1, (see also the discussion in section A.4 of the appendix). Only the transport mechanism occurring via a thin film of mobile molecules is consistent with the experimental observations (diffusive transport *and* a slope ratio of 2:2:1). The most plausible position of such a thin film would be on top of the terrace. A film between the layers or at the substrate surface seems unlikely because the molecules would have to cross the solid monolayers. If, however, the droplets sit on the frozen monolayer, or directly on the substrate, the molecules may flow through a film between the SiO_2 surface and the "frozen" solid monolayer whose existence was derived from ellipsometric data [97].

5. Droplet solidification by growing molecularly thin terraces

Table 5.1. Different transport mechanisms and their corresponding equations for the first growing terrace and the second terrace, before (1ML) and after (2ML) reaching the edge of the first one (* – surface frozen monolayer not counted, ** – surface frozen monolayer counted.)

Transport mechanism	1 st ML	2 nd ML	both (2ML)	slope ratio
through the solid:				
release limited	$R_2^2 - R_1^2 \propto tR_1$	$R_2^2 - R_1^2 \propto tR_1$	$R_2^2 - R_1^2 \propto tR_1/2$	2:2:1
growth limited	$R_2 \propto t$	$R_2 \propto t$	$R_2 \propto t$	1:1:1
diffusive*	$(R_2 - R_1)^2 \propto t$	$(R_2 - R_1)^2 \propto 2t$	$(R_2 - R_1)^2 \propto t$	1:2:1
diffusive**	$(R_2 - R_1)^2 \propto 2t$	$(R_2 - R_1)^2 \propto 3t$	$(R_2 - R_1)^2 \propto 3t/2$	4:6:3
via a thin film:				
release limited	$R_2^2 - R_1^2 \propto tR_1$	$R_2^2 - R_1^2 \propto tR_1$	$R_2^2 - R_1^2 \propto tR_1/2$	2:2:1
growth limited	$R_2 \propto t$	$R_2 \propto t$	$R_2 \propto t$	1:1:1
diffusive	$(R_2 - R_1)^2 \propto t$	$(R_2 - R_1)^2 \propto t$	$(R_2 - R_1)^2 \propto t/2$	2:2:1

5.5.2. Kinetics of growth for first, second, and third monomolecular layer

The images presented in figure 5.18 show the late stages of terrace growth from a C_{36} drop. Three monomolecular terraces grow on top of each other. The image at 4800 s shows the first monolayer, the one at 15600 s the second layer and the final one (22000 s) the third layer. The graphs in figure 5.19 show their kinetics of growth. Note that a solid front does not advance any more as soon as a new layer nucleates and grows on top (open symbols). For all the three layers the slopes are very similar. This observation supports the scenario that the transport of molecules from the central droplet to the terrace edge occurs via a thin film on top of the terrace whose transport properties are barely influenced by the number of molecular layers in the terrace underneath.

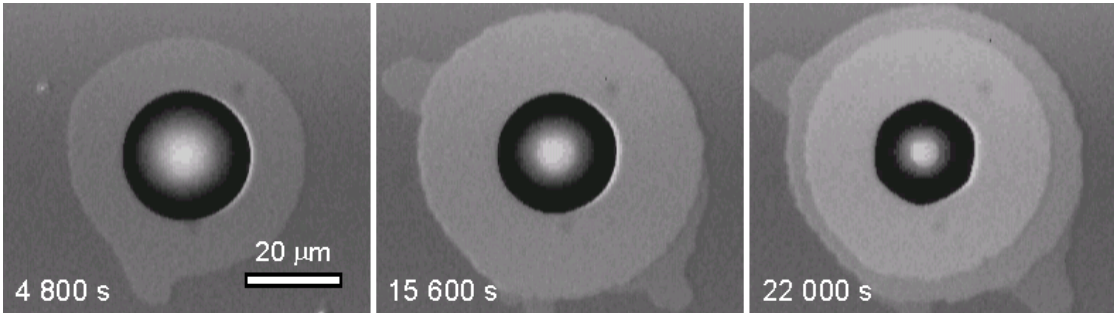


Figure 5.18. Snap-shots during the growth of first, second and third C_{36} monomolecular terraces at 3°C below T_{mp} .

During terrace growth the central drops do not have always a spherical-cap shape. Distortions leading to a hexagonal shape of their three-phase contact line can be observed in some cases (see for instance the last image of figure 5.18). A systematic study of this behaviour is quite difficult because many parameters such as temperature, droplet size, thickness and width of the terrace growing seem to play a role. However, some qualitative observations are worth to be mentioned: (i) the transition from spherical-cap drops to hexagonal-shaped drops is, in most of the cases, continuous; (ii) its occurrence increases with decreasing temperature; (iii) the thicker the growing terrace the more likely the formation of hexagonal-shaped droplets; (iv) the smaller the width of the growing terrace ($R_2 -$

R_1) the more pronounced the distortion. For instance, after nucleation of the second layer of figure 5.18, the droplet shape was also hexagonal but relaxed to a spherical cap in the late stages; the highest distortion occurred when the third layer started to grow. One can suppose that the distortion is a result of anisotropy of the surface energy of the solid terrace or that it is generated by the surface freezing at the L/V interface.

The above-mentioned observations suggest alternatively that the distortion is a dynamic effect, which increases with the amount of alkane passing through the contact line of the central drop.

5.6. Influence of temperature on the terrace growth kinetics

Experiments performed at the same undercooling temperature (for the same alkane) show that the values of the apparent diffusion coefficient for growing one monomolecular layer are varying considerably. This may be attributed to slight changes of the experimental conditions such as temperature drifts, surface preparation and roughness, sample history. In order to discard such possible influences, for each alkane the growth was recorded for drops at the same sample area, using freshly cleaned silicon substrate. To exclude the possible influence of sample history, after recording the growth at one temperature, the samples were heated far above T_{mp} and undercooled to randomly chosen temperatures for the next growth experiment. The results are presented in 5.20. In graph (a), on increasing the undercooling from -1 to -4°C , the values of the slopes (D_{app}) are 0.043, 0.083, 0.145, and 0.172 $\mu\text{m}^2/\text{s}$. This indicates a linear increase of D_{app} with increasing undercooling. The same data are plotted in the graph (b) as $\log(\text{terrace width})$ vs. $\log(\text{time})$. The corresponding slopes on increasing undercooling are 0.50, 0.52, 0.43, 0.43 which confirms the suggested diffusive growth.

Similar results for two series of experiments with C_{36} and one with C_{30} are presented in figure 5.21. The data are plotted as D_{app} vs. undercooling temperature. The two series corresponding to C_{36} alkane are slightly different but for all the samples, D_{app} decreases linearly with decreasing undercooling and the curves can be extrapolated through the origin at the bulk melting point.

5.7. Behaviour of the solidified "drops"

As soon as a drop solidifies it does not contribute anymore to the growth of the terraces. This behaviour is proven by the images of figure 5.22 (C_{36} , 2°C below T_{mp}). In the image (a) all the liquid drops form terraces and, the front (1ML) coming from the droplet in the upper-left corner of the image is about to "touch" the contact line of the central drop. When the central drop "senses" the solidifying front (image (b), 12 s), it solidifies as bulk instead of starting to build its terrace (induced nucleation). Nine hours later, (image (c)), the solidified drop changed its shape (due to bulk annealing) but there is no observable growth of a terrace from its contact line. One can estimate the maximum value of D_{app}^S for the terrace growth from the solidified drop. Differentiating the equation which defines D_{app} we get:

$$D_{app} = 2(R_2 - R_1) \frac{d(R_2 - R_1)}{dt} \approx 2(R_2 - R_1) \frac{\delta(R_2 - R_1)}{\delta t} \quad (5.2)$$

An estimated displacement $\delta(R_2 - R_1)$ smaller than $0.5 \mu\text{m}$ (from the resolution of the optical microscopy image) and a value of $(R_2 - R_1)$ of $\approx 1 \mu\text{m}$, means that the value of D_{app}^S is smaller than

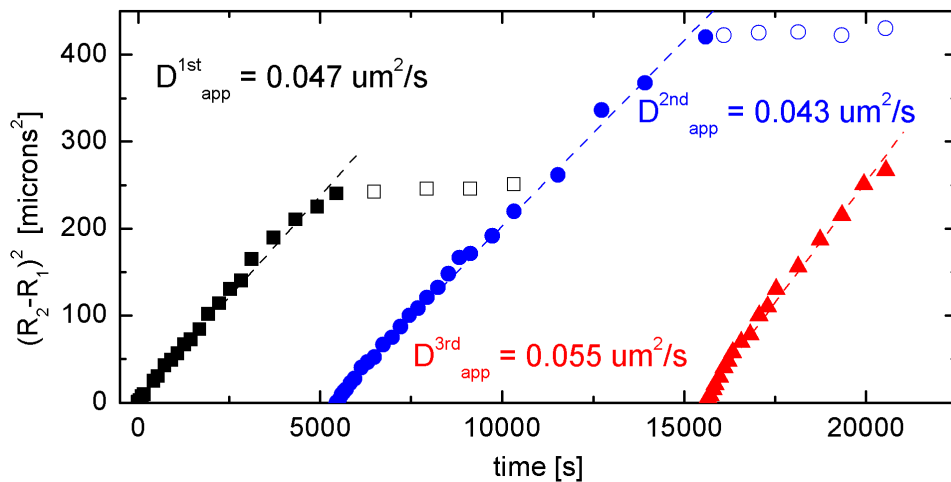


Figure 5.19. Kinetics of sequential growth of three monomolecular terraces on top of each other, corresponding to the images presented in figure 5.18.

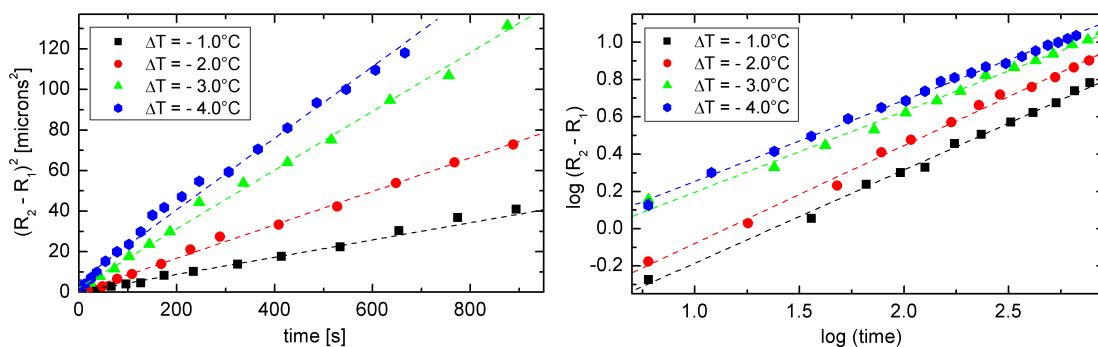


Figure 5.20. Growth kinetics of C_{36} alkane at different undercooling temperatures. The data are represented as: terrace width squared vs. time (a), and logarithm of terrace width vs. logarithm of time, (b).

$1.5 \cdot 10^{-5} \mu\text{m}^2/\text{s}$ at two degrees below the melting point, i.e. at least three order of magnitude smaller than in case of the liquid undercooled drops.

It is important to note that in the second image after solidification, the central drop shrank, revealing a brighter contour of circular shape (with the same thickness as the solid front which touched the drop) whose border describes the initial position of the contact line of the liquid drop. This is an evidence that, after induced nucleation, the solid front advances very fast underneath the liquid, i.e. when a drop grows its terrace, the thickness of the solid structure is the same outside and underneath the undercooled drop.

In figure 5.23 four optical microscopy snap-shots show the difference between the behaviour of solidified drops and liquid ones (different samples with C_{30} , C_{36} , at different undercooling temperatures). One can observe not only that the solidified ones do not form terraces but also that "foreign" growing terraces *avoid* the three-phase line of the solidified ones. This behaviour can be explained by a decreased supply towards the growing fronts when they get closer to solidified drops. Solid structures consume part of the available material for their own, (disordered) growth (see also the discussion section).

For samples covered only with solid C_{36} (terraces and solidified drops), there is no observable change in the positions of the terrace steps after keeping them ≈ 20 hours at one degree below T_{mp} . This proves that (i) sublimation in 3D can be neglected and the (ii) terraced solid structure does not exchange molecules between their terrace steps.

5.8. Monolayer growth from a solid on the bare silicon substrate

As shown, solidified droplets do not form terraces on a silicon substrate covered with a surface frozen monolayer. In contrast, a tiny amount of solid alkane, deposited on the *bare* SiO_2 surface, at temperatures below the melting point, creates a monomolecular layer whose front advances slowly on the surface. The sequence of OM images in figure 5.24 shows a piece of solid C_{30} , forming a terrace on a silicon wafer covered with a thick oxide layer, at 1.7°C below the bulk melting point. Although the advancing front does not move parallel to the apparent contact line between the solid alkane and the substrate (the real three-phase line was under the crystal and obviously not a straight line due to imperfect contact). Nevertheless, it is possible to measure its position along fixed directions. The results averaged for two such directions are plotted in figure 5.25. The double logarithmic plot (a), has a slope of ≈ 0.53 which indicates a diffusive behaviour ($x^2 \propto \text{time}$). In the second graph (b), the data are plotted according to the diffusional power law. The value of the slope (D_{app}) is $0.188 \mu\text{m}^2/\text{s}$.

This experiment comes in support of the assumption that there must be a film of mobile alkane molecules through which the growth of the terrace (in this case, the surface frozen monolayer) is supplied. The fact that the solid film can grow from a solid crystal on the bare substrate but not from a solidified drop sitting on the surface frozen layer indicates that the driving force is significant for the former case and virtually zero for the later one. In other words, the higher surface energy of the *bare* substrate compared to the substrate covered already with a frozen monolayer is the "force" driving the growth from the solid alkane crystal.

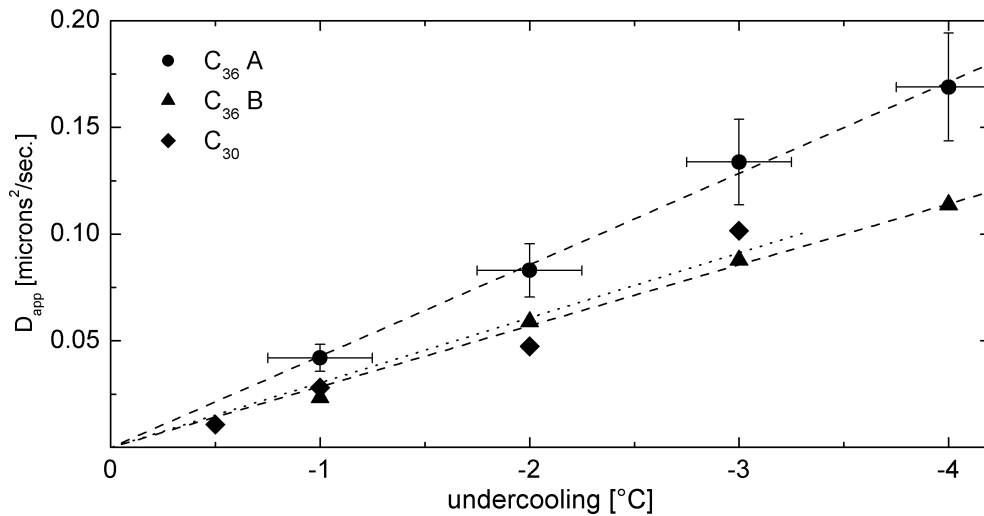


Figure 5.21. Temperature dependence of D_{app} for three series of experiments (for each series: same sample area and preparation history, random variation of undercooling).

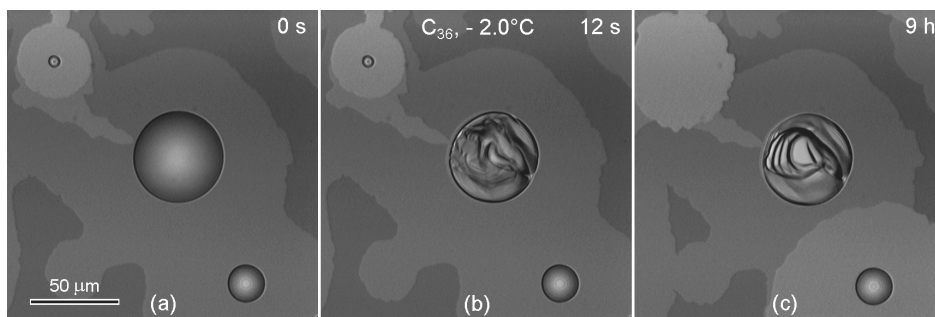


Figure 5.22. Sequence of optical microscopy images showing that solidified drops, although nucleated, do not grow terraces.

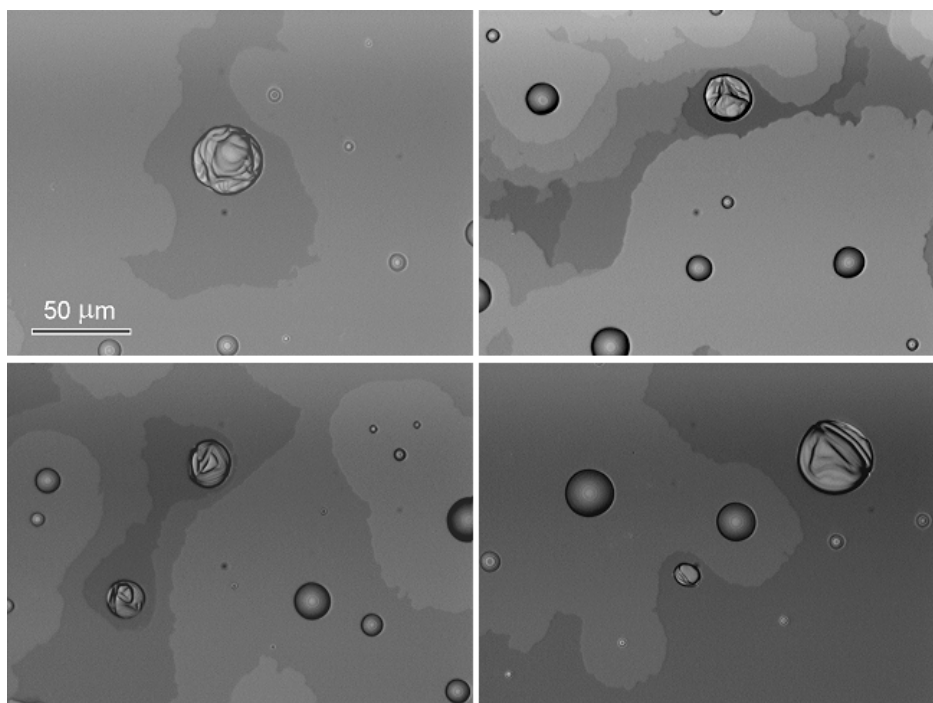


Figure 5.23. Growing (from undercooled, liquid) and non-growing (from solidified) drops (C_{30} , C_{36} alkanes, different undercooling temperatures).

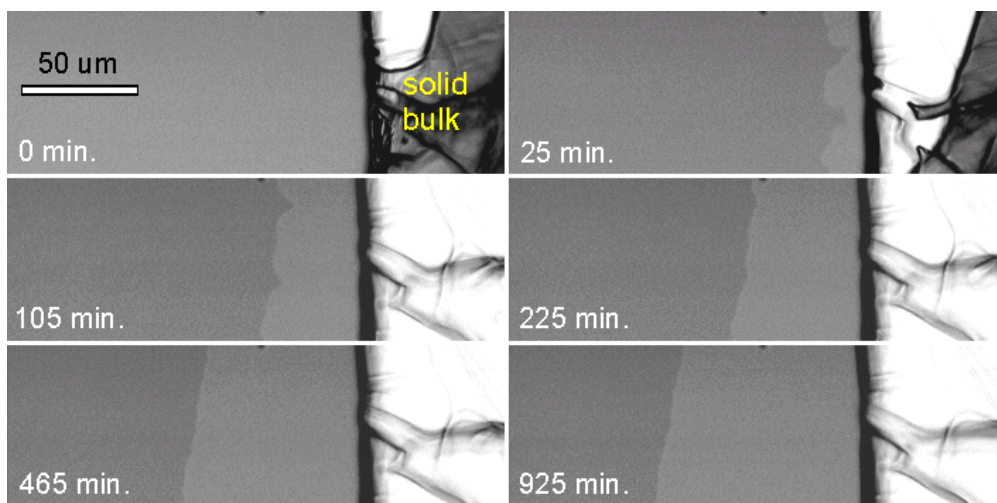


Figure 5.24. Growing of a monomolecular layer (surface frozen) from a solid C_{30} piece on the bare thick oxide covered silicon wafer, at 1.7°C below the bulk melting point.

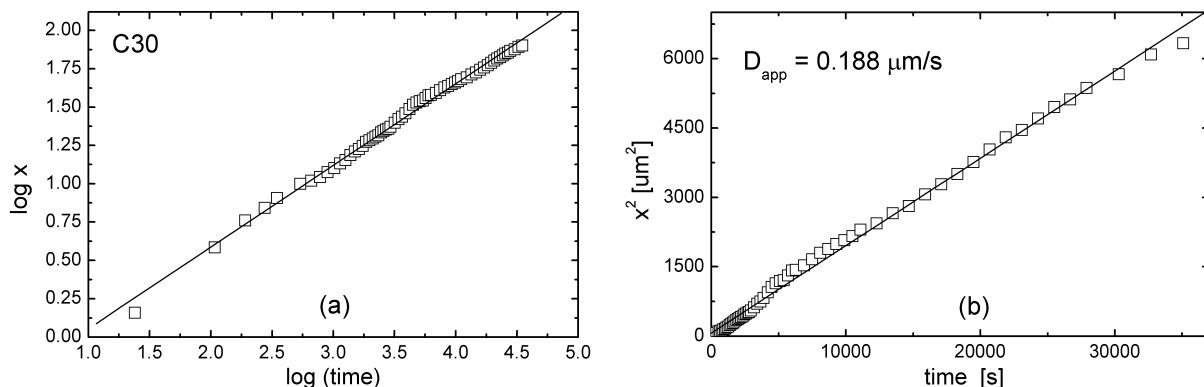


Figure 5.25. Double-logarithmic plot of the front position vs. time describing the growth of a solid terrace on the bare substrate (a), and plot of the position squared vs. time for the same data set, (b).

5.9. Terrace behaviour above bulk melting point

As shown, below T_{mp} droplets can create mono-/multilayer terraces on the substrate covered with surface frozen monolayer. The presence of undercooled alkane droplets is required for this process. In terms of kinetics, it was observed that the higher the undercooling the faster the terrace growth. At T_{mp} the growth stops. Above T_{mp} the growth can even be reversed, i.e. the alkane from the solid terrace can flow back into the liquid drop if the overheating temperature (of the solid terrace) does not exceed a certain limit which depends on the number of molecular layers forming the terrace. For a monomolecular terrace this limit is $\approx +0.3^\circ\text{C}$. Above this limit, another mechanism of melting can be observed (see chapter 6).

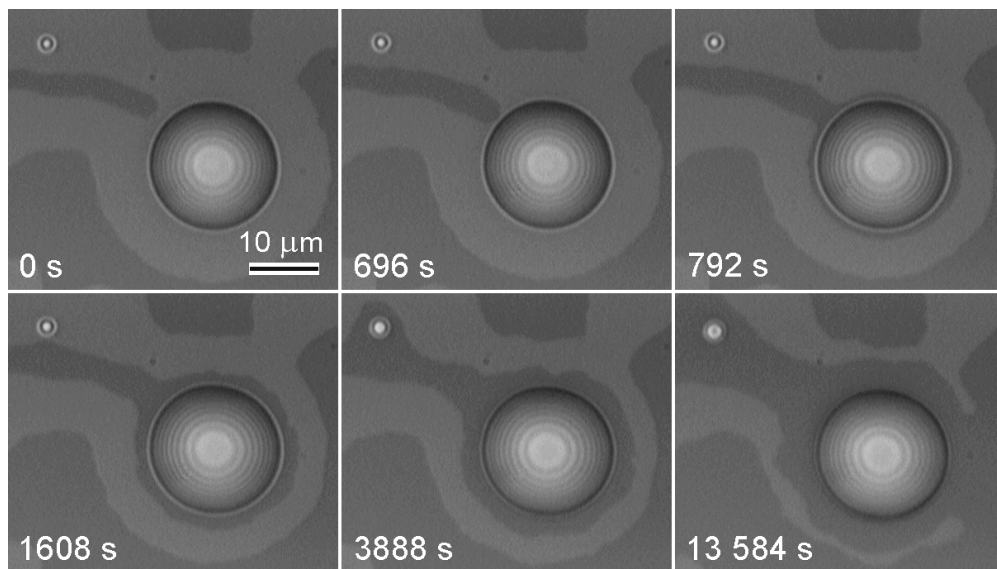


Figure 5.26. Gradual elimination of the monolayer terrace (brighter area) due to an alkane flux towards the droplets ($\approx 0.3^\circ\text{C}$ above bulk melting, C_{30}).

Figure 5.26 shows the time evolution of a monomolecular terrace at $\approx +0.3$ °C overheating. In the first frame (0 s) one can see a big and a small droplet surrounded by a terrace. A lengthy trench in the terrace extends from the upper left corner nearly to the large drop. This trench advances towards the drop (696 s) and eventually initiates the growth of a groove around the large drop (792 s). The groove widens in time as one can see in the figure. The $\log(R_2 - R_1)$ - $\log(\text{time})$ plot in figure 5.27 has a slope of ≈ 0.35 (which is not too far from a "diffusive" exponent).

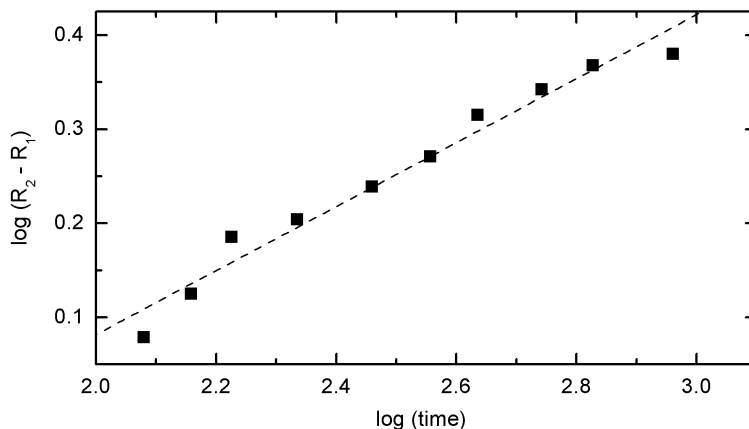


Figure 5.27. Double-logarithmic plot showing the growth kinetics of the groove surrounding the big droplet in figure 5.26.

The fact that the material from the terrace is mostly collected into the droplets and not lost by 3D evaporation can be deduced from the behaviour of very small droplets. For instance, the volume of the tiny drop in figure 5.26 increases gradually due to accumulation of alkane material supplied by the melting at the terrace step (in the region close to the drop, the width of the trench increases in the time interval 0 to 1608 s). The volume of the small drop continues to increase even after the terrace edge reaches its contact line (1608 s to 13584 s) while the groove surrounding it widens. Note also that the outer edge of the terrace surrounding the large drop does not change during the experiment confirming that there is no significant 3D evaporation/sublimation.

5.10. Discussion and conclusions

The experimental results are explained with the model presented in figure 5.28. An undercooled (overheated) alkane droplet partially wets a circular solid terrace (for simplicity, only a monolayer terrace is considered). Both the droplet and the terrace are placed on the solid frozen alkane monolayer which covers completely the planar SiO₂ substrate. The experimental results document an alkane flow between terrace edge and droplet perimeter which is independent from the thickness of the terrace (figures 5.16, 5.19). Therefore a thin film of mobile alkane molecules on top of the terrace is proposed. A film between the layers or between layers and substrate surface seems unlikely because the molecules would have to cross the solid monolayer(s). If, however, the droplets sit on the frozen monolayer or directly on the substrate, the alkanes may well flow between the layers. They may migrate through the thin film intercalated between the SiO₂ surface and the surface frozen monolayer whose existence is derived from ellipsometric data [97].

5. Droplet solidification by growing molecularly thin terraces

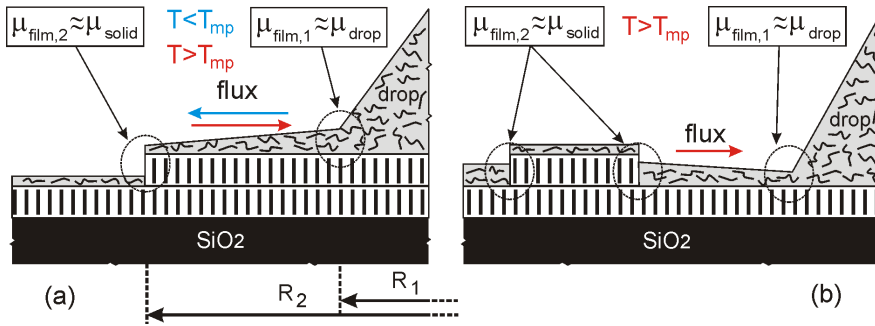


Figure 5.28. Proposed topology and scenario of the terrace growth (a), when the transport occurs via a molecularly thin film on top of the terrace(s). The cartoon (b) presents the topology and transport mechanism for the reversed process (terrace dissolution) at temperatures above the bulk melting point.

The model describes the idealized case of an isolated drop and its terrace. Any alkane exchange between neighbouring droplets and terraces is neglected. In most of the experiments from which the kinetics data were derived, the droplets from which terraces grew were selected such that the distances from their terrace perimeter to the three-phase line of other drops which *did not grow terraces*,³ was larger than that to their "own" three-phase line.

A diffusive transport between the droplet perimeter and the terrace edge can explain the observed behaviour. In general terms, a diffusive flux j , is given by $j = -L\nabla\mu$ ($L \equiv$ phenomenological diffusion coefficient, $\nabla\mu =$ chemical potential gradient). A chemical potential gradient drives the diffusive transport. The gradient is between the terrace edge and the droplet perimeter. At the edge perimeter local equilibrium is assumed ($\mu_{film,1} \approx \mu_{drop}$, $\mu_{film,2} \approx \mu_{solid}$). Either μ_{drop} or μ_{solid} does not correspond to their *thermodynamic equilibrium* values (undercooling or overheating) thus leading to the driving gradient.

For a *linear* growing geometry, the flux is given by:

$$j = -L\nabla\mu = -L\frac{\Delta\mu}{R_2 - R_1} = -L\frac{\mu_{film,2} - \mu_{film,1}}{R_2 - R_1} \approx -L\frac{\mu_{solid} - \mu_{drop}}{R_2 - R_1} \left[\frac{mol}{m \cdot s} \right] \quad (5.3)$$

On the other hand, the flux can be expressed as function of the velocity of the solidification front of the terrace (which is experimentally accessible):

$$j = \frac{\partial R_2}{\partial t} \frac{H\rho_S}{M} \left[\frac{mol}{m \cdot s} \right] \quad (5.4)$$

where $\partial R_2/\partial t$ is the front velocity, H is the thickness of the growing terrace, ρ_S is the mass density of the solid terrace and M is the molar mass of the alkane. Combining equations 5.3 and 5.4 we get the following relation

$$dR_2(R_2 - R_1) = -L\frac{\Delta\mu M}{H\rho_S} dt \quad (5.5)$$

which becomes after integration

$$(R_2 - R_1)^2 = -2L\frac{\Delta\mu M}{H\rho_S} t. \quad (5.6)$$

³Neighbouring drops which grow terraces do not contribute to the growth of the terrace of the droplet of interest, i.e. their growing front acts like a shield (separation line) between the growing front of interest and the external undercooled liquid sources.

For our *circular* growing geometry, the relations are different because the potential gradient is position dependent between R_1 and R_2 . Instead of equation 5.6, a similar line of argumentations (see section A.4 of the appendix, paragraph A.4.3), leads to

$$\frac{R_2^2}{2} \left(2 \ln \frac{R_2}{R_{01}} - 1 \right) + \frac{R_{01}^2}{2} = -2L \frac{\Delta\mu M}{H\rho_S} t \quad (5.7)$$

For $(R_2 - R_1) \ll R_1$, equation 5.7 can be approximated by

$$(R_2 - R_1)^2 \approx -2L \frac{\Delta\mu M}{H\rho_S} t. \quad (5.8)$$

Using the definition of D_{app} (equation 5.1), and equation 5.8, we obtain the following relation between D_{app} and the potential gradient

$$D_{app} = -2L \frac{\Delta\mu M}{H\rho_S}. \quad (5.9)$$

If we assume that the potential difference between the terrace edge and the drop depends on temperature as $\Delta\mu \approx \Delta S_{SL} \Delta T$ ($\Delta S_{SL} \equiv$ molar entropy of fusion, $\Delta T \equiv T - T_{mp}$), the equation 5.9 can be rewritten as

$$D_{app} = -2L \frac{\Delta S_{SL} M}{H\rho_S} \Delta T \propto \Delta T. \quad (5.10)$$

This agrees with the observed linear temperature dependence of D_{app} and explains why the terrace growth can be stopped ($T = T_{mp}$) or even reversed (terrace dissolution). The potential difference can have positive or negative values if the sample temperature is above or below bulk melting, respectively. With this configuration, the transport properties, L , are separated from the driving potential and can be calculated *independently!* Typical values derived from the graph in figure 5.21 are $L \approx 6 \cdot 10^{-22}$ [mol/j.s]. The experimental data still scatter too much to reveal systematic relations (e.g. between transport properties and chain length).

In conclusion, partially wetting, undercooled alkane droplets solidify (continuously) on the surface by growing molecularly thin, terraced structures. The terrace growth is a nucleated process. The main nucleation mechanism is induction, i.e. a growing front from a terrace induces the growth to non-nucleated drops by "touching" their three-phase line. In the solid terrace, the molecules are oriented up-right, i.e. the height of terrace steps is roughly a multiple of the all-trans length of the molecule. Terraces thicker than 1ML form usually via layer-by-layer growth. The growth kinetics obeys a "diffusive" law, (distance)² \propto time.

The terrace growth "speed" decreases with increasing temperature. At the melting point it stops and, above this value the terraces even shrink. This behaviour can be explained considering the solidification (melting) free energy⁴ as the driving force of the terrace growth (dissolution).

The analysis of the sequential growth of monomolecular terraces on top of each other show that the flux of molecules does not depend on the total thickness of the terrace. This indicates that the molecules are transported from the central drop to the growing front via a molecularly thin (a typical "precursor-like") film, most probably present on top of the terrace. The terrace growth can be viewed formally as a peculiar case of *spreading*⁵.

⁴Due to undercooling or overheating.

⁵In this case a precursor film spreads out radially from the nominal contact line of the *partially wetting* undercooled drop.

6. Reversible running drops driven by the S-L phase transition

6.1. Introduction

This chapter describes the formation and movement of liquid alkane droplets on a planar surface, at temperatures slightly above or below the melting point, T_{mp} . The movement occurs on either melting or solidification and is temperature-dependent. Above the melting point, solid, molecularly thin ordered terraces usually start melting from the edges. The edges are equivalent to defects in the solid structure. They generate liquid droplets which subsequently move consuming the solid. In order to move, the droplets must be subject to asymmetric (unbalanced) forces. This happens if a droplet is attached to the terrace step contacting solid regions with different height. After the entire solid structure is consumed, the droplets stop their movement.

Below the melting point, the direction of movement is reversed. In this case parts of the droplets solidify creating a solid terrace. In general, the terrace thickness resulting from droplet movement is preserved to its initial value. The solidification-driven movement may be stopped due to the competing process of symmetrical terrace growth (spreading). In the following the moving droplets resulting from layer melting will be denoted as "advancing" and the ones driven by solidification will be referred to as "receding".

6.2. Nucleation of the advancing running droplets

Terraced solid alkane structures can be obtained either as a result of terrace growth of undercooled droplets or by very fast cooling of completely wetting liquid films from temperatures above the complete wetting transition. In case of the first method the number of layers being formed can be easily controlled by stopping the process at any time. It is easy to quantify the number of solid layers under the optical microscope and the length of the terrace edge per unit area is large enough to analyze the nucleation process. In order to observe the droplet nucleation, after the growth of the terraces the samples were heated very slowly above the melting point until isolated drops appear at the terrace edge. In most cases these droplets are not stable and a slight temperature fluctuation set them in motion. They start to move on the surface consuming the solid terrace.

The nucleation of running drops occurs in two steps: (i) the formation of a drop (bulge) attached to the terrace step¹, and (ii) the detachment of the drops from the step (the drops start moving by consuming the solid material of the terrace).

Such a situation is presented in figure 6.1. The sequence of optical microscopy images show the nucleation and movement of the droplets marked A, B, C, D, and E from the edge of the monomole-

¹The size of these drops increases gradually by collecting the material from the step, i.e. *edge premelting*.

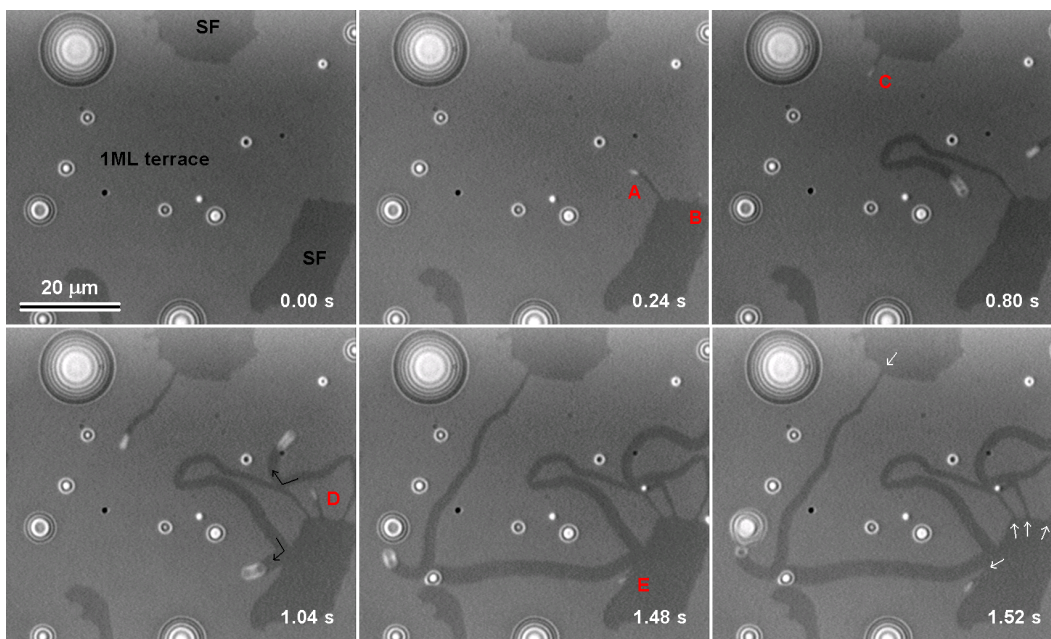


Figure 6.1. Sequence of OM images showing a one molecular layer thick (1ML) terrace (bright area) of C_{30} on top of its own surface frozen (SF) monolayer (dark area), at the bulk melting temperature (0.00s). After a slight increase ($\approx + 0.4^\circ\text{C}$) of temperature (images at 0.24, 0.80, 1.04, 1.48 and 1.52 s), tiny drops nucleate at the edge of the terrace and subsequently move "eating" into the solid terrace. The white arrows in the last image (1.52 s) indicate the nucleation sites of the droplets A, B, C, D, and E. The black arrows in (1.04 s) show the "reflection" of the moving drops at the terrace edge. The apparent elongation of the moving drops is due to stroboscopic (pulsed light) illumination of the sample, (details of the experimental set-up in the appendix section A.3).

molecular C_{30} terrace. Brighter area corresponds to one monolayer (1ML) sitting on top of the surface frozen (SF) monolayer. In the last image (1.52 s) the regions of the step where nucleation occurred (nucleation sites) are indicated with white arrows. The initial width of the grooves which result after nucleation and movement of the droplets is smaller than $1 \mu\text{m}$. When a drop reaches a terrace edge (step) it changes its trajectory as if it had been "reflected" by it. The black arrows in the image (1.04 s) show the "reflections" of the droplets A and B on their movement, after they reach the border between the areas covered by the terrace and the surface frozen layer. In the last two images, the drop C is immediately before (1.48 s) and after (1.52 s) touching the three-phase line of a larger drop. After "collision", the shape of the large drop changes. This effect can not be explained (only) by considering the momentum transfer since the drop increases almost symmetrically its in-plane size. The droplet stretching² suggests that the (metastable) solid terrace present under the large drop melts instantaneously after the "impact". This change in the structure³ of the three-phase line may explain the flattening (see section 6.3.5). Samples with thicker layers behave slightly differently. The AFM picture of an area covered with one- and two layer thick terraces of C_{36} is presented in figure 6.2. From the section analysis it is easy to observe that the regions where the terrace edge has twice the

²This behaviour is analyzed in detail in the section 6.3.5 of this chapter.

³The S/L interface (underneath the drop) changes from two solid layer in contact with the liquid to one (SF) layer in contact with the liquid.

height of a monolayer (≈ 9.7 nm) are preferred sites for nucleation. The initial width of the grooves are in this case, 2.13 and $1.75\mu\text{m}$, respectively. Other similar measurements gave the following values: $1.38\mu(\text{H}) \times 8.87\text{ nm}(\text{V})$, $2.25\mu(\text{H}) \times 8.93\text{ nm}(\text{V})$, $1.75\mu(\text{H}) \times 9.23\text{ nm}(\text{V})$, $1.63\mu(\text{H}) \times 10.99\text{ nm}(\text{V})$, $2.62\mu(\text{H}) \times 11.25\text{ nm}(\text{V})$. The temperature at which the nucleation occurs from steps of two monolayers height is lower ($\Delta T = T - T_{mp} \approx +0.15^\circ\text{C}$) than that from one monolayer height steps ($\Delta T \approx +0.4^\circ\text{C}$).

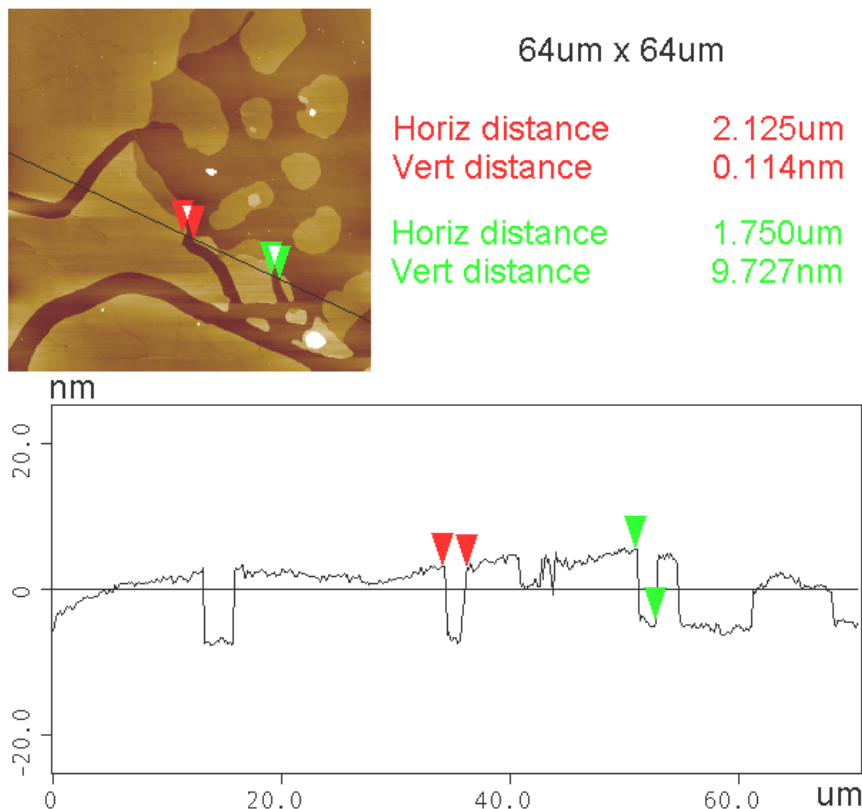


Figure 6.2. AFM section analysis of a C_{36} terrace after the detachment of nucleated drops (tapping modus at room temperature).

6.2.1. Instability of the wetting stripe at the terrace edge

In order to qualitatively explain the formation of the drops attached to the step on increasing temperature, one can consider that a certain amount of liquid alkane is present all over the sample surface, even when the temperature is a few degrees below the melting point. This molecularly thin liquid layer was evidenced indirectly by its transport properties (it supplies the growth of terraces from undercooled drops).

The existence of such a molecular film was proven also by imaging ellipsometry in a slightly different configuration [98]. Samples covered with less than one up-right oriented alkane monolayer were heated at different temperatures below the melting point. The presence of the film was proven

by comparing the area of the solid-covered regions with the thickness of the film in-between⁴.

On increasing temperature, the $-\text{CH}_3$ (top) and $>\text{CH}_2$ (lateral) terminated facets of the terrace behave differently. The liquid film tends to increase its thickness only at the edge, where the $-\text{CH}_2$ terminated facet is exposed. The liquid film on top does not change significantly its thickness. The top surface of the terrace is partially wetted by liquid alkane compared to the step facet which is supposedly completely wetted. The morphology of the liquid stripe which wets the step facet depends on the extent of overheating and on the step height. Two parameters may describe the evolution of the system: the amount of liquid per unit contour length of the step, and the step height. The amount of liquid per contour length increases with increasing temperature and, beyond a certain limit, the uniform liquid stripe becomes unstable. Gau et al. [99] describe the shape instability of liquid microchannels on structured surfaces with a wettability pattern consisting of hydrophilic stripes ($\theta \approx 5^\circ$) on a hydrophobic substrate ($\theta \approx 108^\circ$). They found that the channels undergo a shape instability at a certain amount of absorbed volume, from a homogeneous state with spatially constant cross section to a state with a single bulge. This type of instability differs from the classical Rayleigh-Plateau instability because it leads only to a single bulge. On increasing the volume per unit stripe length, at a certain contact angle value close to, but below 90° , the homogeneous state becomes metastable and the state with a single bulge becomes the state with the lowest free energy. Above 90° , the uniform cylindrical cap shaped channel is unstable leading to one bulge state of the liquid channel. The state with a single bulge is described by a constant mean curvature.

Qualitatively, it is possible to apply their results to our geometry. For simplicity we consider the extreme case, i.e. the top facet and the underlying surface frozen layer are non-wettable ($\theta = 180^\circ$), and the (lateral) facet of the step perpendicular to the sample plane is completely wetted ($\theta = 180^\circ$) by the liquid alkane. Thus, upon increasing the temperature, the step morphology may evolve following the scenario presented in figure 6.3.

6.2.2. Critical radius and free energy barrier

Based on classical heterogeneous nucleation theory, one can roughly estimate the size of the critical nucleus and the associated free energy barrier. Two simplifying assumptions are considered: (i) the liquid droplet which forms as a result of melting, has a spherical cap shape and is not attached to the solid terrace step; (ii) for small overheating temperatures, the surface energy of the solid on top of the terrace is the same as the surface energy of the surface frozen monolayer (both layers having the same molecular orientation with respect to the sample plane, exposing the same terminal $-\text{CH}_3$ groups at the interface). The second assumption means that, for the solid terrace, the replacement of a solid-vapour interfacial area of a thick layer by the same area covered with a thinner terrace does not contribute to the free energy associated to the nucleus formation. Thus, the total free energy, ΔG_{tot} , for creating a nucleus can be calculated from the interfacial free energies associated to the liquid drop formation (solid-liquid, solid-vapour and liquid-vapour interfaces) with the volume free energy $-\Delta T \Delta S \rho_L V_{drop}$, due to the overheating. The first graph (left) of figure 6.4, presents the dependence of ΔG_{tot} , ΔG_I (I = interface), ΔG_V (V = volume) on droplet size (expressed as radius of the circular solid-liquid contact area), for C_{36} at 0.2°C overheating. For the calculation the following parameters

⁴The film is present directly on the substrate surface (SiO_2) and changes its thickness with temperature; this behaviour is probably the consequence of the (temperature dependent) thermodynamic equilibrium, $\text{SF}(\text{surface frozen monolayer}) \rightleftharpoons$ (liquid-like) film.

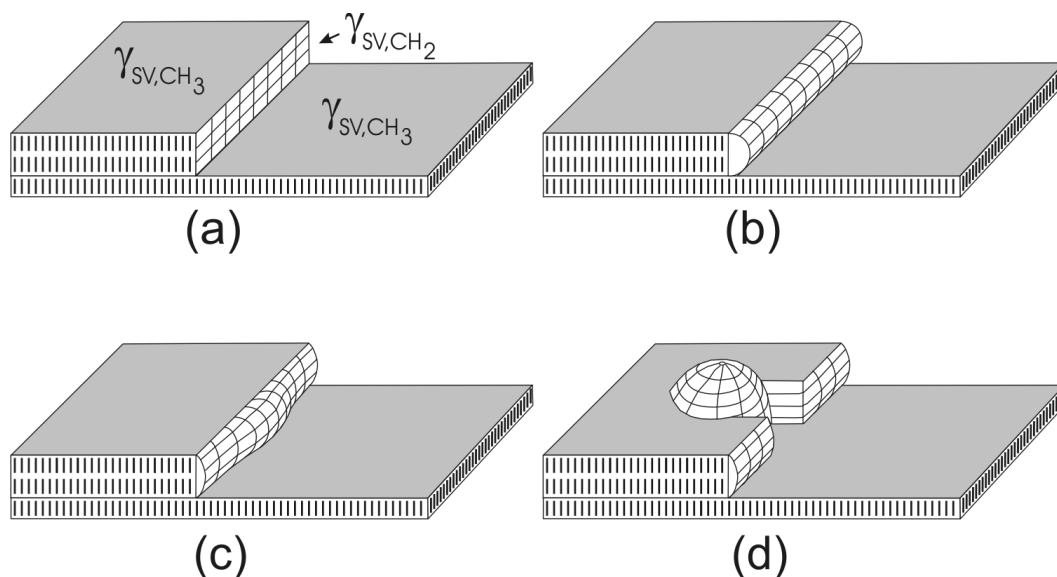


Figure 6.3. Schematic description of the evolution of a solid alkane terrace edge on increasing temperature. (a) Two molecular layer height step far below T_{mp} ; (b) uniform wetting stripe covering the lateral facet of the step; (c) bulge resulting from the instability; and (d) "running" of the drop after detaching from the step.

were considered: enthalpy of fusion 173 J/g [49], $\gamma_{LV} = 29$ mN/m, and $\rho_L = 770$ Kg/m³ and a contact angle of 20°⁵. The corresponding radius of the resulting critical nucleus is 0.26 μ m. The second graph (right) presents the variation of the free energy barrier and the radius of the critical nucleus as function of overheating temperature. In the range of 0.15 to 0.3°C overheating, the calculated R_{crit} is expected to vary between 0.35 and 0.17 μ m. Although a crude approximation, these results are close to the observed sizes of the nucleated droplets which were experimentally observed.

In the temperature range between 0.05 to 0.6°C, the height of the critical droplet varies from 184nm to 15.3nm, i.e. it is much larger than the terrace thickness.

6.3. Kinetics of running droplets on melting

In this section we analyze the velocity of the droplets running on the surface covered with mono- and multimolecular solid layers as function of size, temperature and chain-length of the alkane. For this study, the movement of the droplets is observed under the optical microscope with a CCD camera connected to a digital recording system. The maximum available acquisition rate, 25 frames per second (PAL TV standard), proved to be not enough to get sharp images for fast moving drops. A stroboscopic illumination described in the section A.3 was therefore developed. The power LED was driven typically at a frequency of 250 Hz with a duty cycle of 5% maximum, corresponding to an illumination time of less than 0.2 μ s. As a result, one recorded frame was an overlap of ten sharp images corresponding to different positions of the droplets in motion, at equal time intervals, typically 4 ms.

In order to quantify the influence of the temperature on the velocity of the advancing drops, tem-

⁵This value was observed experimentally.

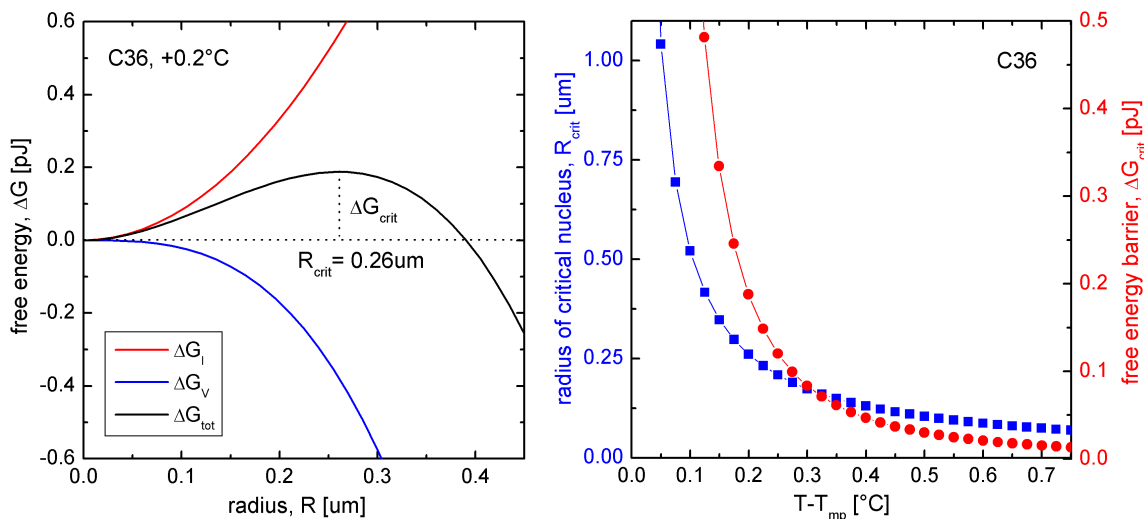


Figure 6.4. Size dependence of ΔG_{tot} associated to nucleus formation for C₃₆ at 0.20°C above the melting point (left) and the temperature dependence of ΔG_{crit} and R_{crit} (right).

perature ramps were generated. The starting temperature of these ramps was chosen at one to three degrees below the melting point in order to keep the transient behavior of temperature out of the range of interest (which is slightly above T_{mp}). By this we ensure that near the melting point and immediately above, the heating rate is constant and small offsets eventually affecting the temperature measurement are kept constant (constant heat fluxes towards the sample and towards the temperature sensor). By synchronizing the temperature ramps and image recording, it was possible to get the corresponding measured⁶ temperature for each image of the recorded sequence.

The heating rates ranged from 0.3 to 0.8°/s, not too slow in order to cover a large enough temperature interval while the drops run and grow, but also not too fast to minimize the possible temperature gradients and to get enough information for a certain temperature (under the assumption that within short times the measured velocity corresponds to one temperature value). This assumption proved to be true after analyzing the data. The frames containing ten overlapped images showed that the moving drop positions are roughly equidistant, i.e. within the corresponding time interval the temperature can be considered constant.

In order to check if inertial effects can affect the validity of the results, slightly overheated samples (for instance to $T_{mp} + 0.2^\circ\text{C}$, for 1ML) were illuminated with an electronic flash to produce an extremely fast, superficial⁷ increase of temperature. The droplets moved instantaneously quite fast and then the velocity decreased due to re-equilibration of the temperature.

The sequence of images shown in figure 6.5 is a typical time evolution of a mono- and bilayer structure of C₂₄ upon heating (the surface frozen monolayer adjacent to the silicon surface is not counted). The brightest area corresponds to the bilayer and the darker to the frozen monolayer. In the first image ($t = 0\text{s}$) two solid spots (circled) are used as internal calibration for the bulk melting

⁶The measured temperature-time data set can be translated into temperature-frame pairs, i.e. it is possible to assign for each image (frame) its corresponding temperature.

⁷This type of heating acts for a short period of time (the temperature decays exponentially to its initial value) since the heat resulting from absorption at the solid surface is dissipated quite fast into the substrate by thermal conduction.

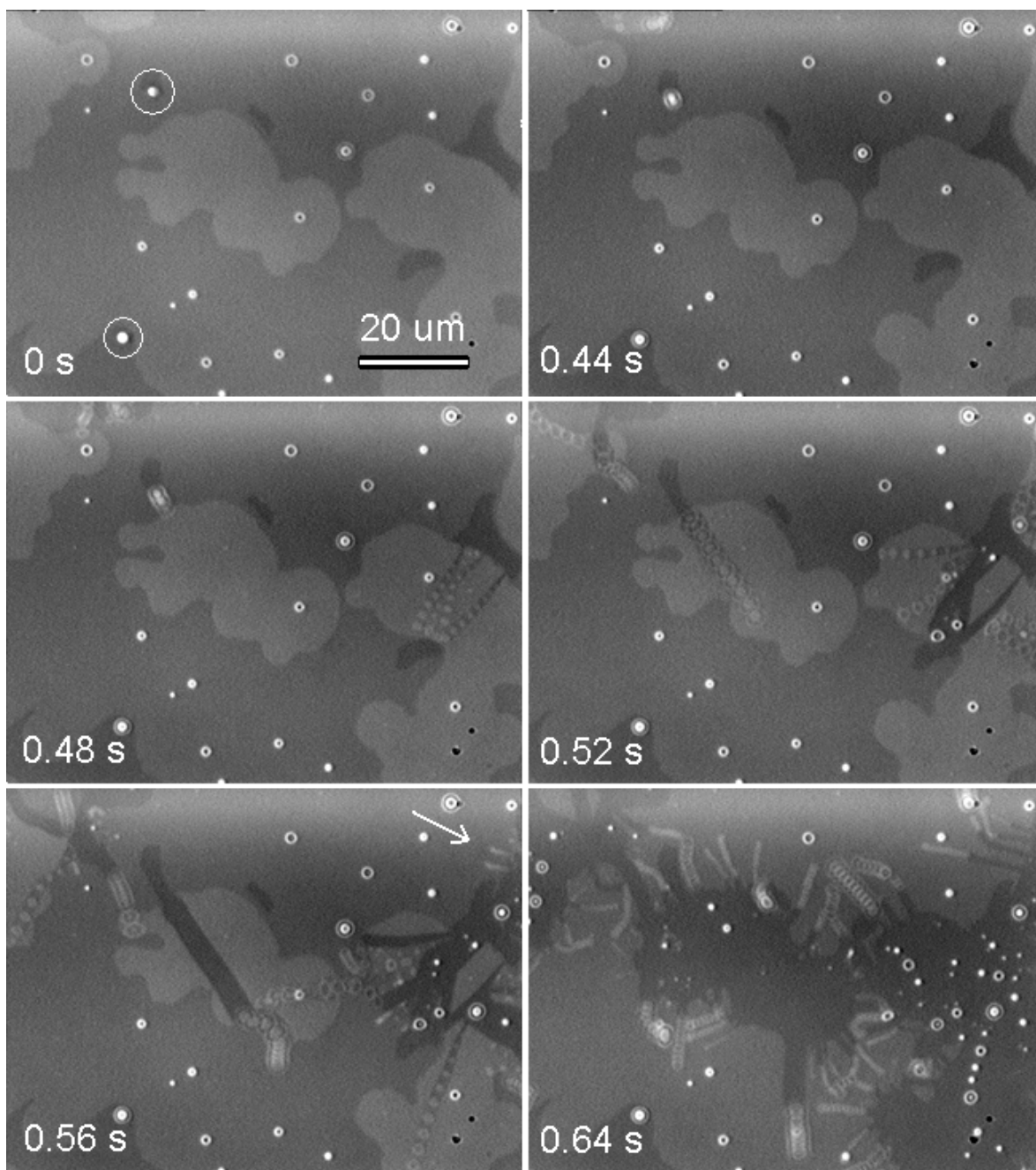


Figure 6.5. Formation and time evolution of running droplets upon heating (\approx linear temperature increase) of a solid C_{24} mono- and bimolecular layer on silicon substrate (illumination with pulsed light at 250 Hz, duty cycle 5%). The white circles indicate two solid spots and the arrow in the fifth image (0.56 s) the nucleation area for droplets moving into a monolayer.

temperature. Note that the other drops are not frozen, they consist of undercooled liquid. Immediately afterwards, (not shown) the two spots melt simultaneously proving that temperature gradients can be neglected. In the upper part of the second image ($t = 0.44$ s), the solid spot which melted into a drop moves at a temperature which is few tens of a degree above the melting point. Most of the droplets do not move because they are symmetrically surrounded by a solid layer with the same thickness. As soon as the symmetry is broken, i.e. when the drop is in contact with layers having different thickness, forces acting on the droplet are not in balance and set the droplet in motion. In the third image ($t = 0.48$ s), three new drops nucleate from the two-layer step and move "eating" into the bilayer. The velocities of these three drops are very similar ($\approx 450\mu\text{m/s}$) and more than 10 times higher than the velocity of the drop which moves only on a monolayer. At 0.52 s the central bilayer which was already touched in the previous frame by our first droplet, is now eaten by it. Upon changing from one to two monolayers, the drop velocity becomes similar to the velocity of other drops "eating" into bilayer structure. New nucleated drops run into the right bilayer. In the upper-left corner of the image one can also distinguish droplets running with two velocities, high speed for two layers and low for the monolayer. The following image ($t = 0.56$ s) shows new droplets nucleating (the arrow indicates their position) at the edge of a monolayer. The same velocity-thickness behaviour can be observed for the rest of the droplets. In the last image the entire two-layer structure is consumed and many drops of different size move "eating" into the monolayer. The velocities at the same temperature (i.e. in the same frame) are size-independent.

6.3.1. Dynamic contact angle of running droplets

Calculation of the dynamic contact angle from mass conservation

In the case of running droplets, the dynamic contact angle can be determined by using a mass conservation argument. On movement, the increase of the droplet volume is given by the amount of solid which melts⁸. The amount dm_S of alkane melted when the droplet advances with dx into the solid layer with the thickness H is

$$dm_S = -\rho_S WH dx \quad (6.1)$$

where W is the width of the solid layer consumed by the droplet on moving, x is the displacement and ρ_S is the solid density. In most of the cases when the droplets move, the interference rings and contact lines have a circular shape. This observation allows us to assume that the running droplets have a spherical cap geometry. Thus, the increase of droplet mass is related to the radius R of the circular contact line by the relation

$$dm_L = d[\rho_L \Xi(\theta) R^3] \quad (6.2)$$

where ρ_L is the liquid density close to the melting point and $\Xi(\theta)$ is a function which converts the cube of radius into the spherical cap volume, $V = \Xi(\theta) R^3$. The value of the function $\Xi(\theta)$ (under the assumption that θ is constant) can be calculated from the two previous equations, by setting $dm_S + dm_L = 0$ and replacing the width with $2R$. This gives,

$$\Xi(\theta) = \frac{2\rho_S H dx}{3\rho_L R dR} \quad (6.3)$$

⁸This assumption is particularly true for short time intervals (seconds) since the evaporation rate is very low.

After integration, the above equation becomes

$$\Xi(\theta) = \frac{4\rho_S H \Delta x}{3\rho_L \Delta(R^2)} = \frac{16\rho_S H \Delta x}{3\rho_L \Delta(W^2)} = f(\theta, \Delta W^2, \Delta x) \quad (6.4)$$

where $\Delta(R^2)$ is the increase of R^2 associated to a Δx displacement. The contact angle can be recovered from $\Xi(\theta)$ (derivation in the section A.1.1 of appendix) by using the equation,

$$\theta(\Xi) = \pi - 2 \arctan(x_0^{-1}) \quad (6.5)$$

where x_0 is the solution of the third order equation $x^3 + 3x - 6x/\pi = 0$,

$$x_0 = - \left(\sqrt[3]{\frac{-3\Xi}{\pi} + \sqrt{1 + \frac{9\Xi^2}{\pi^2}}} + \sqrt[3]{\frac{-3\Xi}{\pi} - \sqrt{1 + \frac{9\Xi^2}{\pi^2}}} \right) \quad (6.6)$$

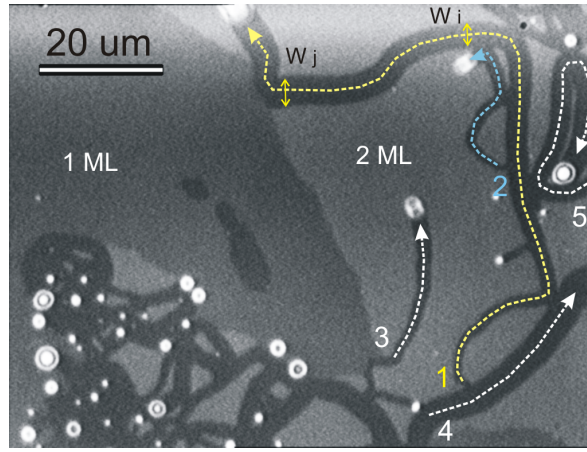


Figure 6.6. Optical microscopy image showing the geometry used to calculate θ_D from mass conservation. The five paths marked with dashed arrows correspond to different in-plane droplet sizes, ranging from 0.9 to 5 μm in diameter.

In figure 6.6 is presented a snap shot of a C_{24} mono- and bilayer structure during melting via running drops, few tenths of a degree above the melting point. In the area covered by a molecular double layer (2ML), five running droplet paths, marked with dashed lines, are selected for calculating the dynamic contact angle (the droplets 2 and 3 are moving at a velocity of about $35\mu\text{m/s}$). By choosing two positions along these paths one can measure the corresponding displacement, Δx and local path widths, for instance W_i and W_j for droplet 1. Considering a solid/liquid density ratio of $\rho_S/\rho_L \approx 1.1$ and $H = 2 \times 32.4\text{\AA}$, the calculated dynamic contact angles are in the range of 10 to 15° . A slight decrease of contact angle with increasing size can be observed. By dividing the long path of the droplet 1 into three regions it is possible to calculate three (size dependent) values of the contact angle. These values are shown in table 6.1 together with the values for the droplets 2 to 5.

Static contact angle after melting the solid layers

Immediately after the entire solid structure is melted, the contact angle of the droplets is not changing significantly if the temperature is far enough below the wetting transition ($T_W = T_{mp} + 3.5^\circ\text{C}$). In the

6. Reversible running drops driven by the S-L phase transition

Table 6.1. Calculated dynamic contact angle for C24 drops running into a two molecular layer structure (velocity $\approx 35 \mu\text{m/s}$).

Drop No.	size range, W_i-W_j [μm]	path length [μm]	θ_D [$^\circ$]
1	0.9-2.3	25	15.0
1	2.3-3.8	42	12.2
1	3.8-5	44	11.9
1	0.9-5	111	12.6
2	1-1.9	14	14.0
3	1.4-2.7	25	12.8
4	4.2-5	28	10.7
5	2.3-3.9	47	12.8

graph of figure 6.7, the static (\approx equilibrium) contact angles of three alkane chain lengths is plotted against droplet size, at $\approx 1^\circ\text{C}$ above their melting point. The average values are $18.85 \pm 2.23^\circ$ for C₂₄, $19.30 \pm 2.23^\circ$ for C₃₀, and $22.41 \pm 1.17^\circ$ for C₃₆.

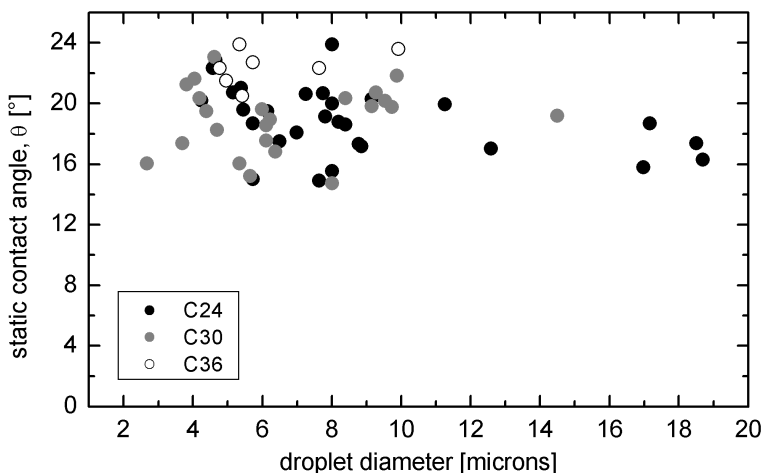


Figure 6.7. Static contact angle of C₂₄, C₃₀, and C₃₆ drops as function of their in-plane diameter, (at $\approx 1^\circ\text{C}$ above the melting point).

6.3.2. Dependence of velocity on droplet size

The droplet velocities as a function of the overheating temperature, for different droplet sizes, is shown in figure 6.8. The data refer to running droplets "eating" into a C₃₆ monolayer. They are classified into four groups, according to their in-plane diameter. The plot indicates that the velocities are size-independent. C₂₄ and C₃₀ show similar behaviour.

In the case of melting two or three solid layers, it is easier to observe experimentally that the velocities are size-independent because, for the same displacement, the thicker the terrace, the faster the increase in size.

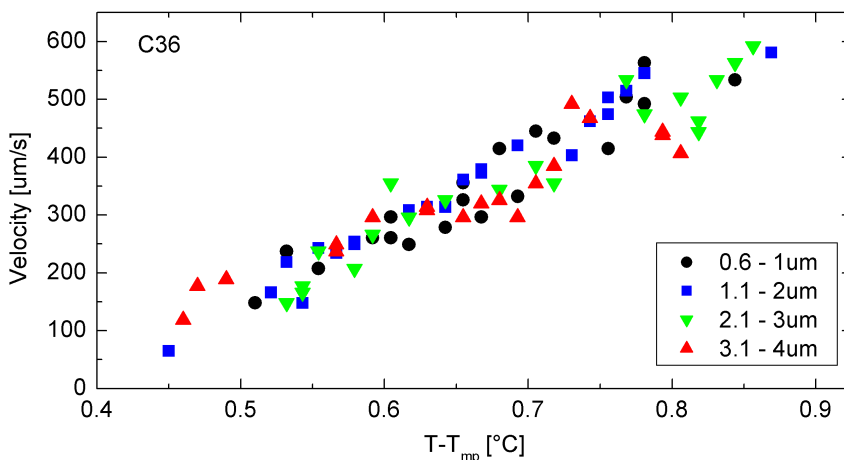


Figure 6.8. Dependence of droplet velocity on overheating temperature for different droplet sizes. The droplets are classified into four classes according to the values of their in-plane diameter.

6.3.3. Dependence of velocity on temperature and number of molecular layers

As already described, the temperature at which the liquid droplets start moving is always above the bulk melting point, defined as the melting temperature of solidified polycrystalline drops. The reproducibility of the melting point as previously defined was checked by slowly heating the samples, from a few degrees below the expected melting point, at a heating rate of less than $0.2^{\circ}\text{C}/\text{min}$. For a set of 7 samples, the values of the melting point did not differ by more than $\pm 0.05^{\circ}\text{C}$.

In the following, data are presented based on the previous observation that the droplet size does not influence significantly the velocity. As a consequence, velocity values are plotted irrespective of size. A systematic study of droplet velocities vs. temperature and number of layers was performed for all three alkanes C_{24} , C_{30} and C_{36} . The most accurate results are the ones for C_{30} , presented in figure 6.9⁹.

The initial temperature and the rate of temperature increase were very similar for all the samples, $T_{\text{init}} - T_{\text{mp}} = -2.75 \pm 0.15^{\circ}\text{C}$ and $dT/dt = 0.67 \pm 0.03^{\circ}\text{C}/\text{s}$.

The melting temperature of the frozen droplets (T_{mp}) measured during temperature ramp is very close to the melting temperature measured under quasi-equilibrium conditions (extremely slow heating rates). The maximum observed difference, $|T_{\text{mp},\text{eq}} - T_{\text{mp},\text{ramp}}|$, did not exceed 0.14°C , indicating that the melting point is not shifted much by a high heating rate (no detectable kinetical effects on melting). Rather the temperature sensed by the Pt100 sensor lags behind the temperature on top of the sample due to the small heat capacity of the sensor. For each sample the melting point was determined from the video frame sequence and not from the time-temperature record¹⁰. For samples having many frozen drops on the observation area, the melting occurred for all of them within one frame, corresponding to a melting interval of less than 0.02°C . This proves that there is no significant

⁹This is mainly due to a better temperature sampling; for the experiment with C_{30} , the temperature sensor, glued on a silicon wafer with the same dimensions as the sample dimensions, was positioned on top of the heating plate, in a position equivalent with the sample position, using the same silicon oil thermal connection.

¹⁰For each measurement, the temperature values recorded as temperature-time pairs were calibrated (shifted) according to the melting point observed in the video frame sequence. Subsequently, the corresponding temperature value was assigned to each frame in the video sequence.

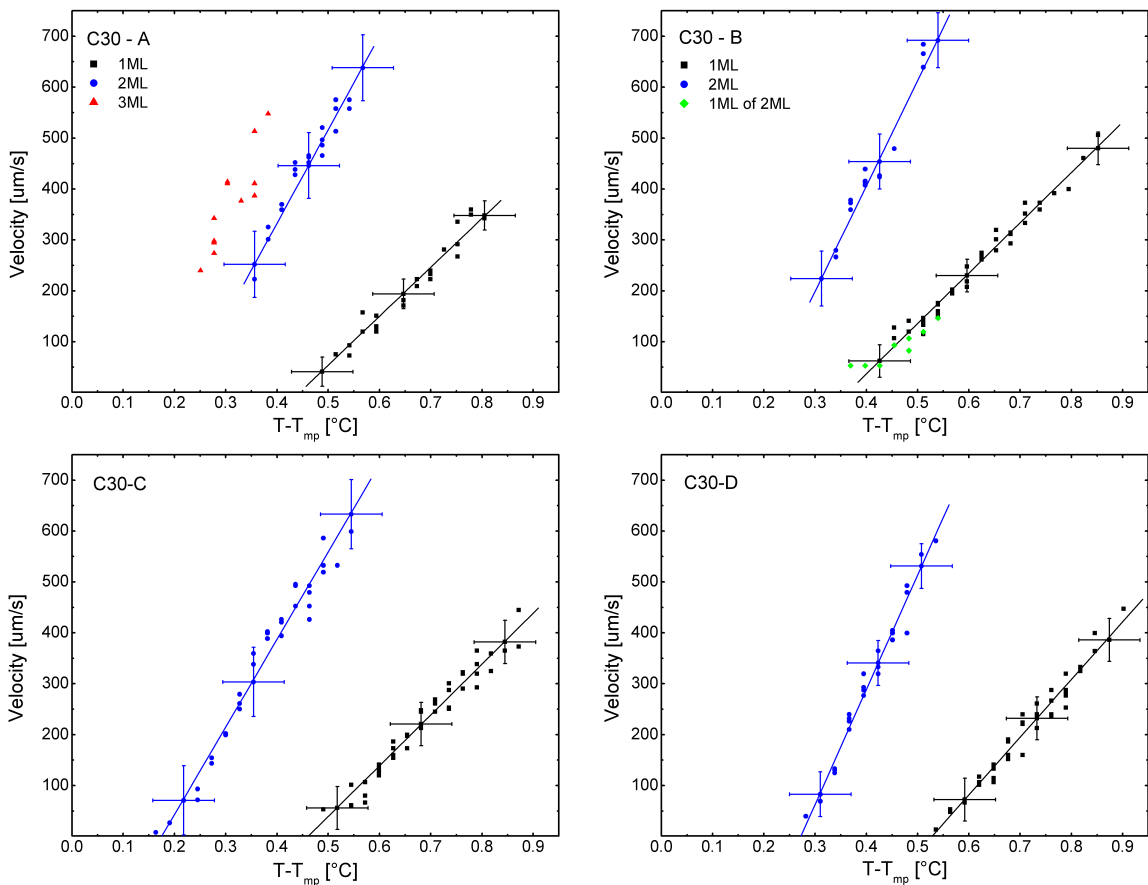


Figure 6.9. The dependence of droplet velocity vs. temperature for different number of solid layers, in the case of C_{30} . The data in the four graphs correspond to different samples measured within one day, with the silicon wafer substrates from the same cleaning batch.

temperature gradient which may act¹¹ as driving force for the running drops.

In the four graphs of figure 6.9, one can observe a linear increase of the velocities vs. temperature. For both, one (black squares) and two molecular solid layers (blue circles) being eaten by running droplets. The velocity error bars are twice the standard deviation calculated from the linear fit of each data set and the estimated temperature error is $\pm 0.06^\circ\text{C}$. The corresponding linear relation can be written as

$$U(\Delta T, N) = U_{0N} + s_N \Delta T \quad (6.7)$$

where $\Delta T = T - T_{mp}$ is the overheating, N is the number of solid, monomolecular layers, U_{0N} is the velocity (negative offset) at the bulk melting point and s_N is the temperature slope of the velocity with temperature. Since the value U_{0N} does not have an obvious physical meaning, the linear dependence may be described better by the zero velocity temperature intercept, $\Delta T_{0N} = -U_{0N}/s_N$. The fitting results describing the linear dependence are shown in table 6.2.

Table 6.2. Linear fit parameters of velocity-temperature dependence for one and two melting layers of C_{30} , (errors represent 2σ , double of standard deviation).

Sample	$s_1 [\mu\text{m/s}^\circ\text{C}]$	$s_2 [\mu\text{m/s}^\circ\text{C}]$	$\Delta T_{01} [^\circ\text{C}]$	$\Delta T_{02} [^\circ\text{C}]$	$U_{01} [\mu\text{m/s}]$	$U_{02} [\mu\text{m/s}]$
C30-A	960	1839	0.44	0.22	-426	-402
C30-B	988	2066	0.36	0.20	-358	-420
C30-C	997	1720	0.46	0.17	-460	-300
C30-D	1132	2252	0.53	0.27	-597	-612
average	1019 ± 154	1969 ± 474	0.45 ± 0.14	0.22 ± 0.09	-460 ± 201	-434 ± 260

The slope of the velocity vs. temperature for two monomolecular layers (2ML), $s_2 = 1969 \pm 474 \mu\text{m/s}^\circ\text{C}$, is about twice the value for one monomolecular layer (1ML), $s_1 = 1019 \pm 154 \mu\text{m/s}^\circ\text{C}$. This means that the slope of the driving force with temperature is proportional to the solid layer thickness. The zero velocity temperature intercepts (ΔT_{0N}) decrease with the number of layers, from $0.45 \pm 0.14^\circ\text{C}$ for 1ML to $0.22 \pm 0.09^\circ\text{C}$ for 2ML.

The graph C30-B deserves special attention: the green square points labeled "1ML of 2ML" are the droplet velocities "eating" a monomolecular layer on top of the first, surface frozen molecular layer. Although this type of melting was rarely observed compared with the situation when the entire thickness available is being "eaten", the result is important because it shows that the number of layers being melted is the key parameter determining the velocity. The distance from the substrate does not play an important role.

In the case of three solid layers (the red triangles in the graph labeled C30-A), the data points were not enough to get a reasonable fit. However, it is clear that, at the same temperature, the velocity increases with the number of layers being "eaten".

The velocity dependence with temperature and number of layers for C_{36} alkane are shown in figure 6.10 for two experimental runs. In terms of overheating values, these results are less accurate compared with ones for C_{30} due to the a different position of the temperature sensor. The error bars are twice the standard deviation calculated from the linear fit for the velocity, and $\pm 0.08^\circ\text{C}$ for the temperature.

The linear fit parameters for the two graphs are shown in table 6.3.

¹¹Droplets can move on a planar surface if they are subject of a temperature gradient which generates usually a surface

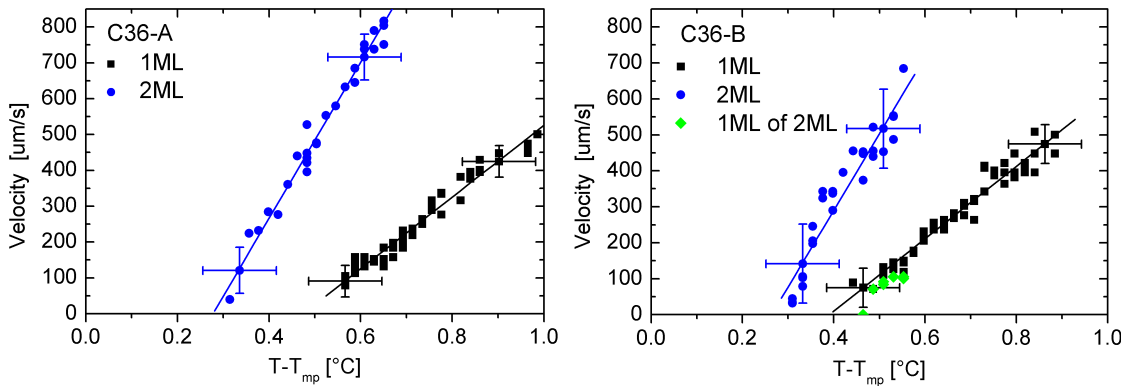


Figure 6.10. The dependence of droplet velocity vs. temperature for different number of solid layers for C_{36} .

Table 6.3. Linear fit parameters of velocity-temperature dependence for one and two melting layers of C_{36} .

Sample	s_1 [$\mu\text{m/s}^\circ\text{C}$]	s_2 [$\mu\text{m/s}^\circ\text{C}$]	ΔT_{01} [$^\circ\text{C}$]	ΔT_{02} [$^\circ\text{C}$]	U_{01} [$\mu\text{m/s}$]	U_{02} [$\mu\text{m/s}$]
C36-A	999	2174	0.47	0.28	-473	-603
C36-B	1008	2131	0.39	0.26	-394	-562
Average	1004	2153	0.43	0.27	-434	-583

Besides the data describing the droplet velocities when the entire thickness of the available solid structure is melting (1ML and 2ML), the graph labeled C36-B of figure 6.10 shows the velocity-temperature dependence for the case when only one of the two available layers melts. The behaviour is similar to the one observed for C_{30} (see the graph labeled C30-B in figure 6.9) i.e. the velocities at the same overheating temperature depend on the thickness of the layer being consumed (one molecular layer) and not on its position with respect to the solid substrate (on top of the surface frozen layer or on top of two layers).

The graph in figure 6.11 describes the experimental results for C_{24} alkane. These data bring additional evidence that the number of molecular layers melting is the dominant parameter deciding the droplet velocity at a certain overheating temperature. The velocity-temperature data points describing the melting of 1ML of 2ML available (green rhombs) overlap with the ones corresponding to melting of 1ML on the surface frozen layer (black squares). The same observation is valid for melting of 2ML of 3ML (red hexagons) compared with melting of 2ML on the surface frozen layer (blue circles). As previously observed for C_{30} (graph C30-A of figure 6.9), the velocities of the running drops for melting of 3ML on the surface frozen layer (red triangles) are characterized by a higher slope vs. overheating and a lower zero velocity temperature intercept as compared with the cases when two and one solid monolayer is being consumed. The fitting results are presented in table 6.4.

6.3.4. Generalized dependence of velocity versus terrace thickness and overheating

The analysis of the experimental results for the three alkanes, having different solid terrace thicknesses and at different temperatures, suggests that the data points can be unified into a *master curve*.

tension gradient (Marangoni effect).

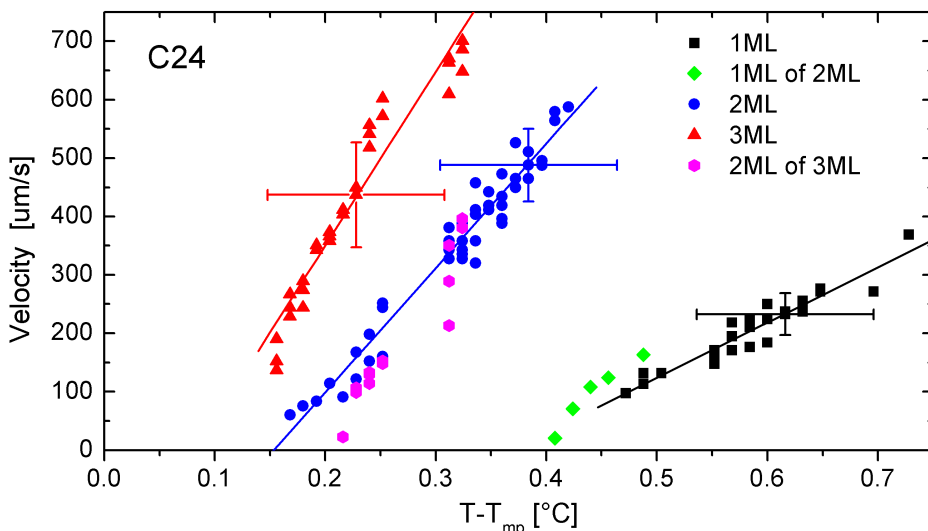


Figure 6.11. The dependence of droplet velocity vs. temperature for different number of solid layers for C_{24} .

Table 6.4. Linear fit parameters of velocity-temperature dependence for one, two and three melting layers of C_{24} .

Nr. of layers	$s_N[\mu\text{m/s}^\circ\text{C}]$	$\Delta T_{0N}[\text{C}]$	$U_{0N}[\mu\text{m/s}]$
1ML	944	0.37	-347
2ML	2128	0.15	-326
3ML	2977	0.08	-245

The values of the velocity extrapolated to the bulk melting point are very similar ($U_{0,1} \approx U_{0,2} \approx U_{0,3} \equiv U_0$), and the slopes are proportional to the terrace thickness. The equation of the master curve is:

$$\tilde{U} = \tilde{s}\Delta T \quad (6.8)$$

where the "reduced velocity" is defined by $\tilde{U} \equiv [U(\Delta T, N) - U_0]/N$ and \tilde{s} is the slope of the reduced velocity vs. overheating temperature when one molecular layer is being melted. The graph in figure 6.12 presents the master curve for the data points presented in figure 6.11. The value of U_0 was calculated by averaging the three $U_{0,N}$. Using the result of the averaging, the \tilde{U} values were recalculated and plotted against overheating. The slope \tilde{s} which results from fitting is $944\mu\text{m/s}^\circ\text{C}$.

6.3.5. Driving force: Surface tension or melting free energy?

In the temperature range between the bulk melting point and few tens of a degree above, interesting aspects of the behavior of some drops reveal the driving mechanism for moving droplets. *Non-moving* droplets sitting on their own solid terraced structure¹² can show two different behaviors:

(i) the drops *do not change* significantly their contact angle¹³ and its value is very similar to the one corresponding to the drops sitting on the surface frozen layer, i.e. $\approx 20^\circ$ (see, for instance, the

¹²This refers to drops which *are not* attached to a step,

¹³See for instance the static drops in figures 6.1 and 6.5.

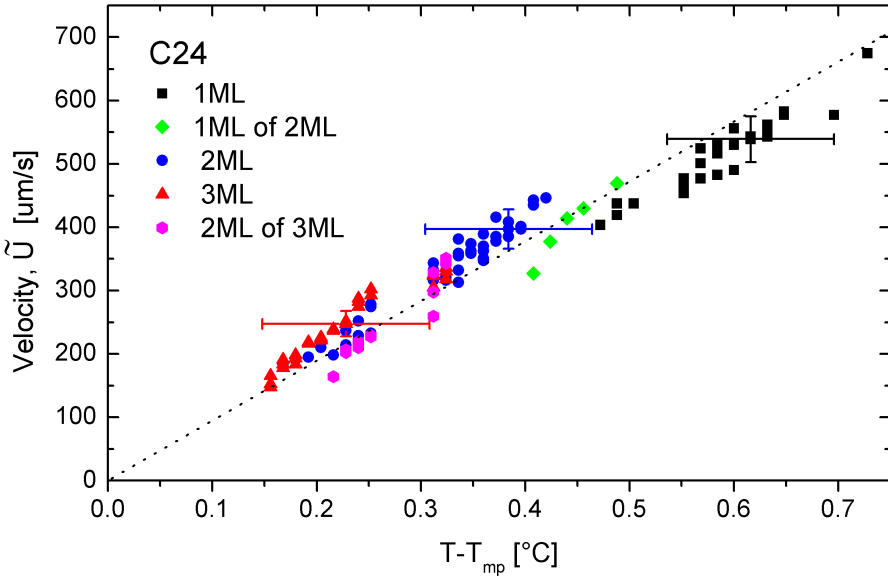


Figure 6.12. Unifying the data points of figure 6.11 into a *master curve*, described by $\tilde{U} = \bar{s}\Delta T$.

graph of figure 6.7).

(ii) on increasing the temperature droplets *change dramatically* their contact angle (see figure 6.13); this behaviour is more pronounced with increasing number of molecular layers.

For the first case (i), considering the Young equation (which describes the horizontal balance of forces at the three-phase line),

$$\gamma_{LV}(T) \cos \theta^{(i)}(T) = [\gamma_{SV}(T) - \gamma_{SL}(T)]^{(i)} \quad (6.9)$$

and the fact that for liquid long chain alkanes (e.g. C_{20} , C_{36}), the temperature dependence of γ_{LV} (in the range T_{mp} to $T_{mp} + 1^\circ\text{C}$) is given by the equation¹⁴ [100],

$$\gamma_{LV} \approx 28.6 - 0.1(T - T_{mp}) \text{ [mN/m]} \quad (6.10)$$

we can conclude that, in the temperature range of interest, both sides of the equation 6.9 do not vary significantly with temperature ($\cos \theta \approx \text{const.}$ and $d\gamma_{LV}/dT \approx 0.1 \text{ mN}/(\text{m}^\circ\text{C})$). The line (i) in the graph of figure 6.14 corresponds to the (almost constant) value of $\gamma_{LV} \cos \theta^{(i)}$ (γ_{LV} is calculated according to equation 6.10).

For the second case, under the assumption that at each temperature the contact angle corresponds to a quasi-equilibrium shape¹⁵, we can also write the Young equation,

$$\gamma_{LV} \cos \theta^{(ii)}(T) = [\gamma_{SV}(T) - \gamma_{SL}(T)]^{(ii)} \quad (6.11)$$

whereby assuming that in this case $\theta^{(ii)}$ varies significantly with temperature as presented in the graph of figure 6.14(b). Something seems wrong because the left sides of the equations 6.9 and 6.11 are different while the right sides are the same. However, one may argue that, for the second case (ii),

¹⁴Not considering the formation of the surface frozen layer.

¹⁵This means that the viscous dissipation is small enough to reach very fast the equilibrium shape corresponding to each temperature during the temperature ramp.

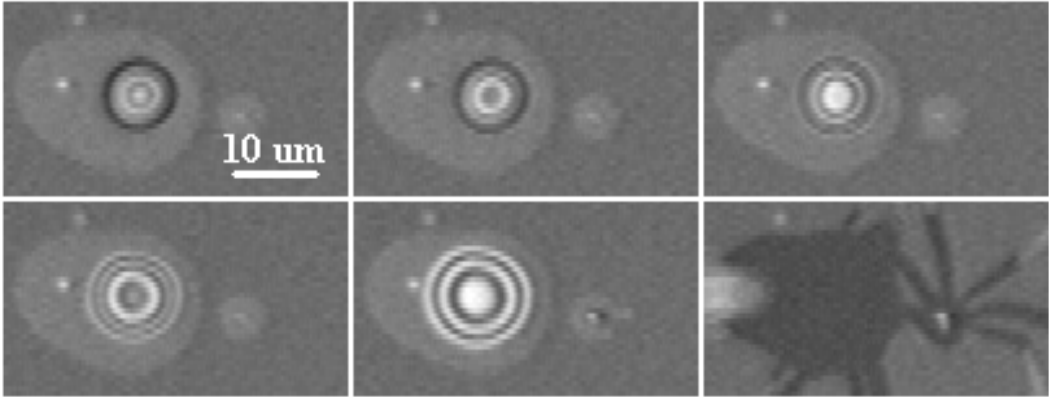


Figure 6.13. Sequence of images showing the time (and temperature) evolution of a C_{30} drop in contact with its own 3ML thick solid terrace upon increasing temperature. In the first five images the drop does not move on the surface but is "stretched" symmetrically by a force field which increases with temperature (finally the symmetry is broken and few running drops are generated).

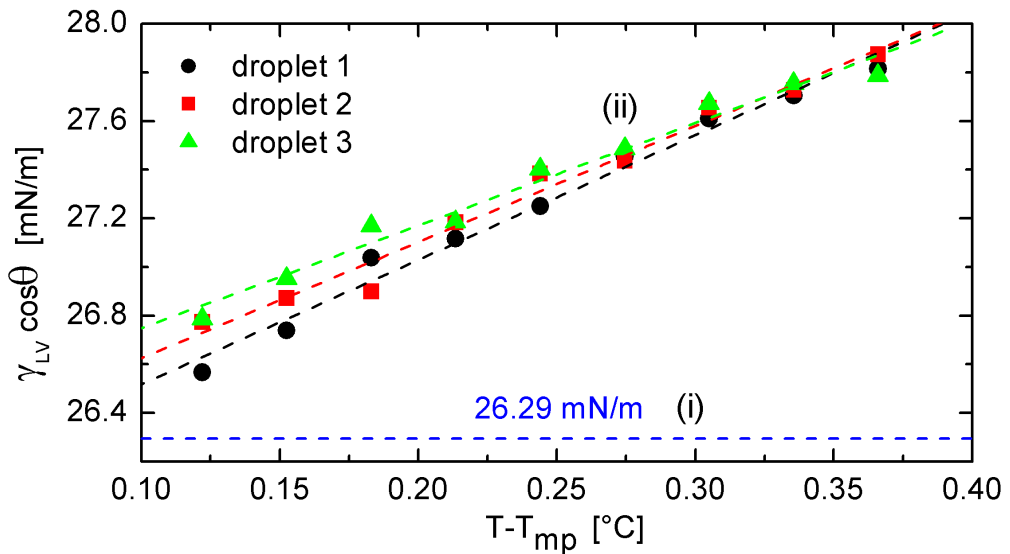


Figure 6.14. Horizontal component of γ_{LV} for: (i) droplets which do not change their contact angle on increasing temperature and (ii) the drop depicted in figure 6.13 and two other similar drops.

6. Reversible running drops driven by the S-L phase transition

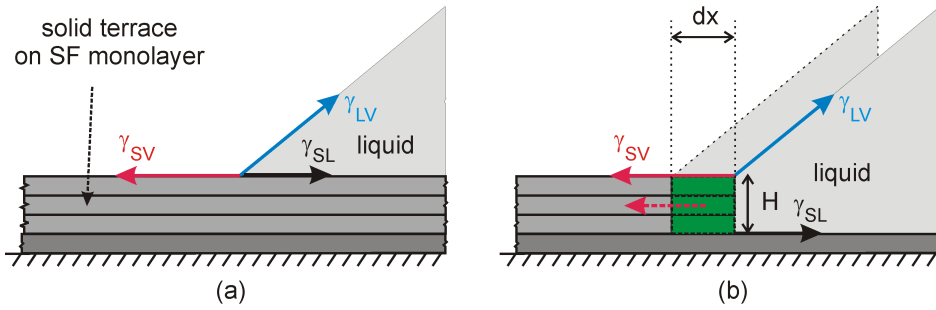


Figure 6.15. Proposed structure for the three-phase line when the contact angle (a) *does not* vary and (b) *varies* significantly with increasing temperature. In order to explain the second behaviour a *quasi-2D solid film tension* $\gamma_{fus} \propto \Delta T$, (red-dashed arrow is subfigure (b)), is considered as correction term in the horizontal balance of forces at three-phase line.

the increase of $\cos\theta^{(ii)}$ with temperature may correspond to a *change in the structure* of the three-phase line. We suggest that, in the cases when θ barely change with temperature the solid terrace remains present underneath the liquid while in case (ii) it does not. Figure 6.15 shows schematically the two structures.

We can add a correction term to equation 6.11 and thus solve the inconsistency of equation 6.9. This term takes into account the temperature variation of $\gamma_{LV} \cos\theta^{(ii)}$,

$$\gamma_{LV} \cos\theta^{(ii)} = \gamma_{SV} - \gamma_{SL} + \tau \Delta T = \gamma_{SV} - \gamma_{SL} + \gamma_{fus} \quad (6.12)$$

where ΔT is the overheating and τ is the temperature slope of $\gamma_{LV} \cos\theta^{(ii)}$ which is accessible experimentally. In our case the values of $\tau = \partial \gamma_{LV} / \partial T$ are 5.1, 4.8, and 4.2 mN/(m°C) (the slopes of lines (b) in the graph of figure 6.14). The correction term, a *quasi-2D tension* which adds to γ_{SV} (same direction) is named γ_{fus} because is most probably generated by the free energy of melting (fusion).

To check the validity of this assumption we calculate the force (per unit length) which will be generated by the free energy of melting. For our geometry, the work done by γ_{fus} is given by

$$\gamma_{fus} dx = -\Delta g_{fus} \quad (6.13)$$

The free energy of melting which corresponds to dx is,

$$\Delta g_{fus} = -H \rho_S \frac{\Delta H_{fus}}{T_{mp}} \Delta T dx = -H \rho_S \Delta S_{fus} \Delta T dx \quad (6.14)$$

where ρ_S is the solid (terrace) density, $H dx$ is the volume (per unit length), ΔH_{fus} and ΔS_{fus} are the enthalpy and entropy of fusion, respectively (per unit mass). Combining the two equations above we get,

$$\gamma_{fus} = -H \rho_S \frac{\Delta H_{fus}}{T_{mp}} \Delta T \quad (6.15)$$

For C_{30} , the enthalpy of fusion is about 160J/g [49]. For a molecular layer of up-right oriented C_{30} molecules (40Å thick, density of about 900 kg/m³), the value of $\gamma_{fus}(T)$ is 1.69 ΔT mN/m. This means that for three layers, the temperature slope $\tau_{fus} = d\gamma_{fus}/dT$ is about 5.1 mN/(m°C) which agrees quite well with our experimental values.

6.3.6. Calculation of the temperature slope of the driving force using the hydrodynamic model

The hydrodynamic model describing the droplet movement on a solid surface assumes the balance of driving force with the viscous force. Making use of the "lubrication approximation" theory of fluid mechanics (see section 2.2 in the chapter 2), the viscous force per unit length of a circular ridge in motion can be approximated by,

$$F_D = F_V \approx 6\eta \frac{UL}{\theta_d} \quad (6.16)$$

where U is the velocity, L is a dimensionless coefficient ($L \equiv \ln(x_{max}/x_{min})$, x_{min} and x_{max} the micro- and macroscopic cut-offs, respectively). The same equation stands also for a spherical cap drop moving on the surface. The running drop experiments reveal values of the slope of velocity with temperature (s_N). By calculating the derivative of the F_V ($= F_D$) with respect to temperature,

$$\frac{\partial F_V}{\partial T} = \frac{\partial F_D}{\partial T} = \frac{6\eta UL}{\tan \theta_d} \frac{\partial U}{\partial T} = \frac{6\eta L}{\tan \theta_d} s_N \quad (6.17)$$

the temperature slope of F_D can be derived. For C_{24} alkane, taking $\eta_{C_{24}}^{60^\circ} = 4.48 \text{ mPa s}$ [101], and $\theta_d \approx 10^\circ$ (see section 6.3.1), the value of L is ≈ 5.9 (the microscopic cut-off $\approx 0.5 \text{ nm}$, the macroscopic cut-off $\approx 2 \text{ }\mu\text{m}$). Considering $s_1 \approx 1 \text{ mm/s}$, we get $\partial F_V / \partial T = 0.96 \text{ mN}/(\text{m}^\circ\text{C})$. This is quite similar to $1.38 \text{ mN}/(\text{m}^\circ\text{C})$, the theoretical value assuming as driving force the free energy of melting. This result is another indication that, most probably, the movement is driven by the melting free energy, balanced by the viscous dissipation.

The two quantitative analysis' presented above suggest that there is no solid structure¹⁶ under the melting-driven running drops.

6.3.7. Dewetting Kinetics of the all-liquid film

The dewetting transition occurs¹⁷ when the temperature decreases below T_{SF} (i.e. $\approx 3^\circ\text{C}$ above the bulk melting temperature). Using the stroboscopic illumination, the velocity of the dewetting front was determined when the samples were cooled at a rate of $\approx 2^\circ\text{C/s}$. Figure 6.16 shows a sequence of optical microscopy images describing the dewetting of a C_{30} film with a thickness of about 100 \AA (2-3 up-right oriented ML). In the first image (top, left) the white arrows indicate some darker spots (defects) which, in the second image are the starting points of the dewetting process. Within one image (40 ms) up to ten concentric rings can be observed. The distance between two consecutive rings corresponds to a time interval of 4 ms. The dewetting velocity is independent of the radius of the dewetted area (equal distance between the concentric circles).

Graph (a) in figure 6.17 shows the time variation of the circular ridge radius upon dewetting (the data correspond to three dewetting regions in figure 6.16). The ridge radius varies linearly with time, i.e. the dewetting velocity is constant. The corresponding slopes (velocities) are 620, 614, and 652 $\mu\text{m/s}$, respectively. The second graph (right) presents the the dewetting velocities for different samples of C_{30} and C_{36} . The average velocity in case of C_{30} is $598 \pm 83 \text{ }\mu\text{m/s}$ (SD) and $622 \pm 67 \text{ }\mu\text{m/s}$ (SD) in case of C_{36} .

¹⁶Surface frozen layer is not counted.

¹⁷See the diagram 5.1 in chapter 5

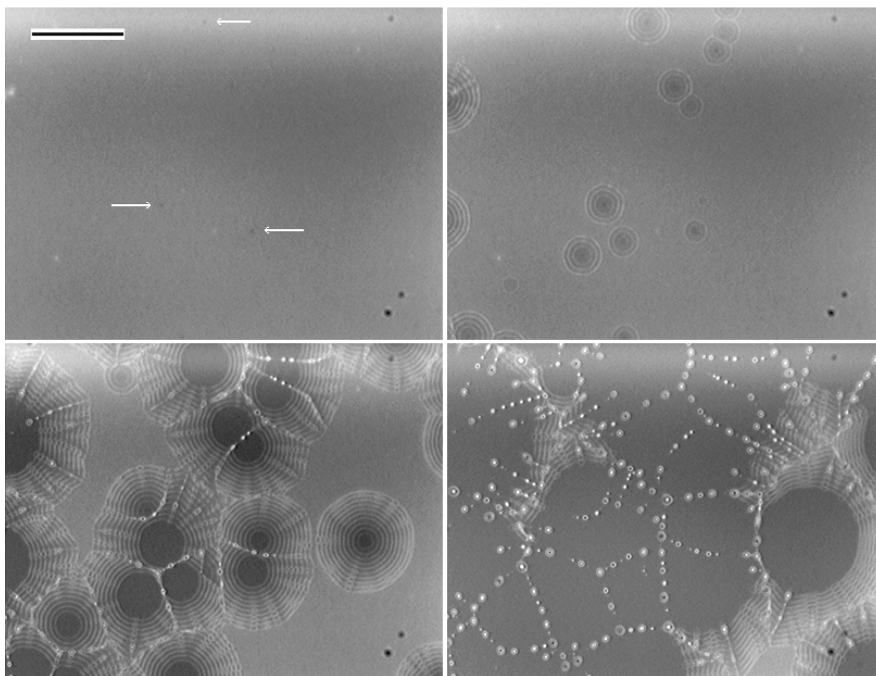


Figure 6.16. Sequence of images at 40 ms time intervals, illuminated with 250 Hz pulsed light, showing the dewetting kinetics of a C_{30} film (scale $50 \mu\text{m}$); in the first image (top-left), the starting points of dewetting (black defects) are indicated with arrows.

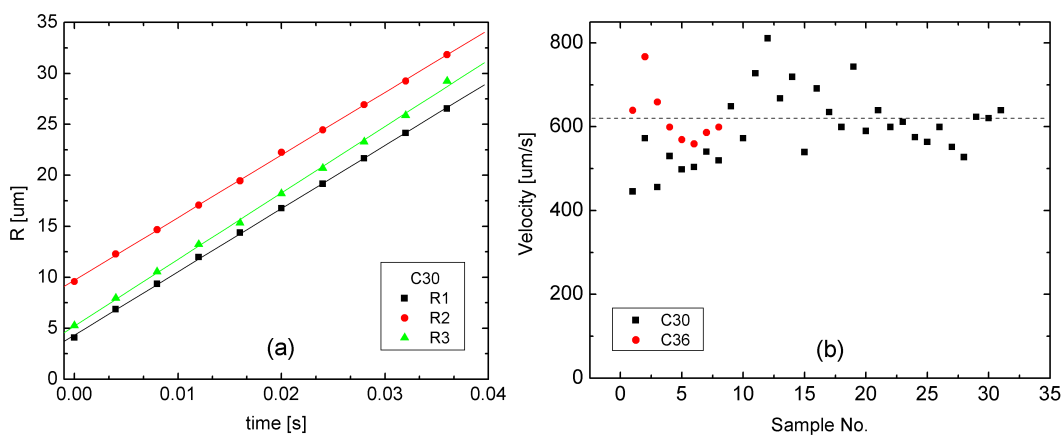


Figure 6.17. Time evolution of the radius of the dewetted area (a) corresponding to the figure 6.16 and dewetting velocities of C_{30} and C_{36} films measured for different samples (b).

Comparing the dewetting velocity of the thin liquid alkane films with the velocities of the running drops one can estimate that the liquid dewetting represents the limit case of "solid dewetting" i.e. running drops. In other words, the velocities of the running drops increase with increasing overheating but not beyond the liquid dewetting limit. A transition between the "running drop" mechanism of solid dewetting and liquid dewetting is expected at higher overheatings. This transition is discussed in more detail in chapter 7.

6.4. Running droplets driven by solidification

In chapter 5 was shown how undercooled droplets form molecularly thin, circular solid terraces. Under certain conditions an undercooled drop can form solid plateaus and move. Similar to the melting-driven running drops, the movement is driven by an unbalanced force field acting parallel to the sample plane. Most probably the difference in the front and rear contact line structures generates the driving force.

The solidification via running droplets *competes* with the formation of a round terrace and is a fairly rare event. It typically occurs when moving drops which "eat" into a solid terrace are stopped by lowering the temperature below T_{mp} . This creates an asymmetrical situation where the undercooled droplet is on one side in contact with a solid terrace and on the other side with the substrate.

Some characteristic features of solidification-driven running drops deserve special attention because they may help to elucidate the mechanism of movement:

(i) the movement occurs only in a very small temperature range below the melting point, not exceeding -1°C undercooling, further undercooling destabilizes the movement leading to terrace formation (symmetrical spreading);

(ii) the thickness of the solid trail which forms as the result of movement is usually more than 3-4 layers (solidifying running droplets forming only one molecular layer thick trail were not observed);

(iii) the velocity is more than two orders of magnitude slower than the melting-driven movement for the same deviation from T_{mp} and the same solid thickness being formed or consumed.

6.4.1. Temperature dependence of the velocity for solidification-driven running drops

The OM image sequence in figure 6.18 shows the *reversible* movement of three C_{24} drops *above* (19.6 s), and *below* T_{mp} . During solidification the drops follow the path which was previously created by partially melting the terraces. The trajectories are not straight, on their movement the droplets tend to avoid the 6 ML height terrace "walls" like being reflected by them. On their way, they reconstruct the solid structure at a thickness corresponding to the highest solid terrace which they contacted when they started moving. This feature can be observed in the area within the white rectangle (32.6 s) where a small drop leaved behind a 6 ML thick solid although it moves on an area with thicker coverage.

The graph 6.19 shows the temperature dependence of the velocity for three solidifying drops with roughly the same size ($14\mu\text{m}$). The velocity increases linearly with decreasing temperature. The slope dU/dT is $-2.7\mu\text{m}/(\text{s}^{\circ}\text{C})$ and the zero velocity intercept is about -0.1°C below T_{mp} .

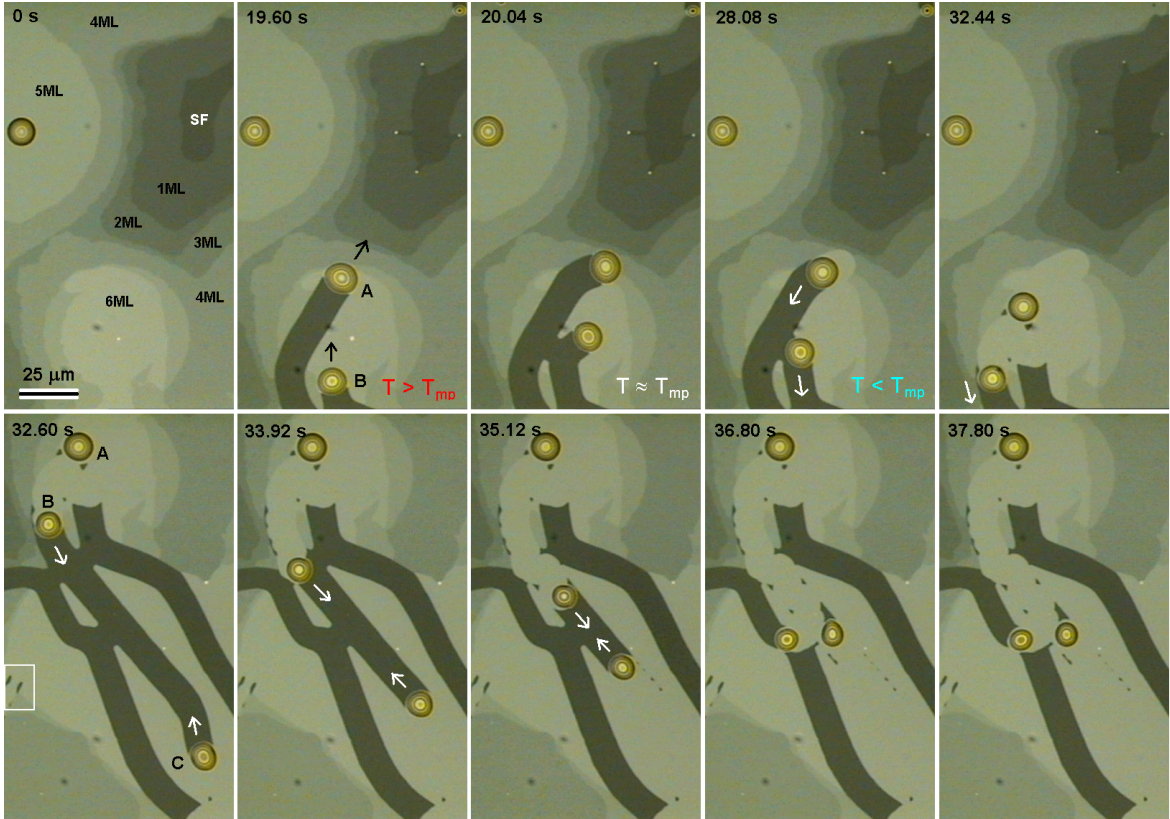


Figure 6.18. Solid terraced structure of C_{24} with a maximum height of 6ML (the surface frozen layer not counted) (0 s) at the melting point; (19.6 s) two (A, B) advancing drops "eating" the terrace upon a slight increase of the temperature; (20.04 s) the drops stop due to a slight decrease of temperature; further decrease (28.08 s) of temperature (below T_{mp} makes the drops move in the reversed direction; drop B moves while A stops (32.44 s) because it is surrounded by the terrace; in the rest of images the drop B and another drop C move leaving behind the solid plateau (which has the same thickness as the highest terrace they were in contact with when the movement driven by solidification started); finally both B and C stop moving and start to grow terraces (after image at 32.44 s, the observation area was changed).

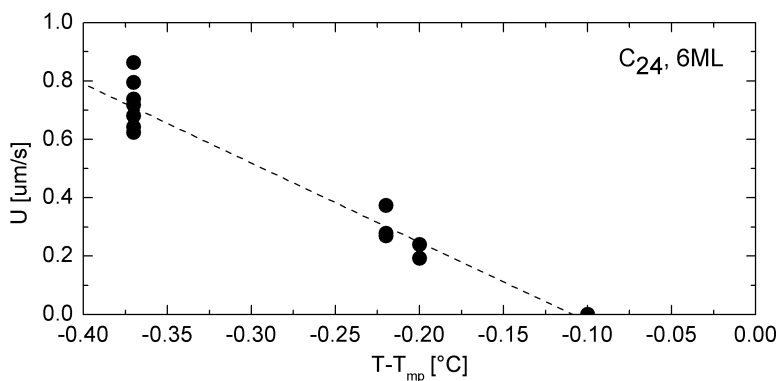


Figure 6.19. Temperature dependence of velocity when 6ML thick terrace forms as a result of movement (data correspond to figure 6.18).

6.4.2. Sequential initiation of solidifying running droplets

A special case for triggering the movement of droplets upon solidification is presented in figure 6.20, (a). This was observed by studying the movement of C_{36} drops on a mica substrate, at few tenths of a degree below T_{mp} . In subfigure (a), a sequence of optical microscopy images shows the movement of a droplet marked A towards droplet B (time mark 0s). When the distance between the two drops becomes very small ($< 1\mu\text{m}$), the droplet B becomes distorted and starts moving as if it was "kicked" by A (16s). Further on, following the same pattern, droplet B initiates the movement of droplet C (20s), which continues to move (25s). The average velocity of droplets A and C was $\approx 1.5\mu\text{m/s}$. This behaviour is quite surprising since two droplets approaching each other at a distance at which they can exchange liquid are expected to coalesce minimizing their surface free energy.

6.4.3. Mechanism of solidification-driven running drops when thin solid terraces are formed

Section 6.3.5 suggested a possible structure of the three-phase line for moving drops driven by melting, i.e. most likely the melting-driven (advancing) running drops sit directly on top of the surface frozen layer with their leading front attached to the terrace step¹⁸.

A possible mechanism, consistent with the features of solidifying moving drops, is schematically presented in figure 6.20, (b). The proposed scenario assumes that the structure of the leading part of the drop consists of a solid terrace (microscopic scale) whose solidifying front moves slightly ahead of the nominal contact line (macroscopic scale) of the undercooled drop¹⁹. The growth of the solidifying front is supplied from the macroscopic drop through a molecularly thin liquid film covering the solid structure. The assumption that the solid terrace is present underneath the undercooled drop is supported by the fact that, at few tenths of a degree below T_{mp} , a solidification front present at the rear

¹⁸In that case the thickness of the solid melting was in the order of few molecular layers; there are indications that the same topology would be consistent with the experimental evidence presented in chapter 7 (i.e. drops attached to a thick terrace adjust their position (melt or solidify gradually) upon extremely small changes of temperature.

¹⁹This implies the presence of the solid terrace (with the same thickness as the one which is formed) underneath the drop; this consideration is consistent with the undercooling range and extent at which the solidification-driven running drops move.

6. Reversible running drops driven by the S-L phase transition

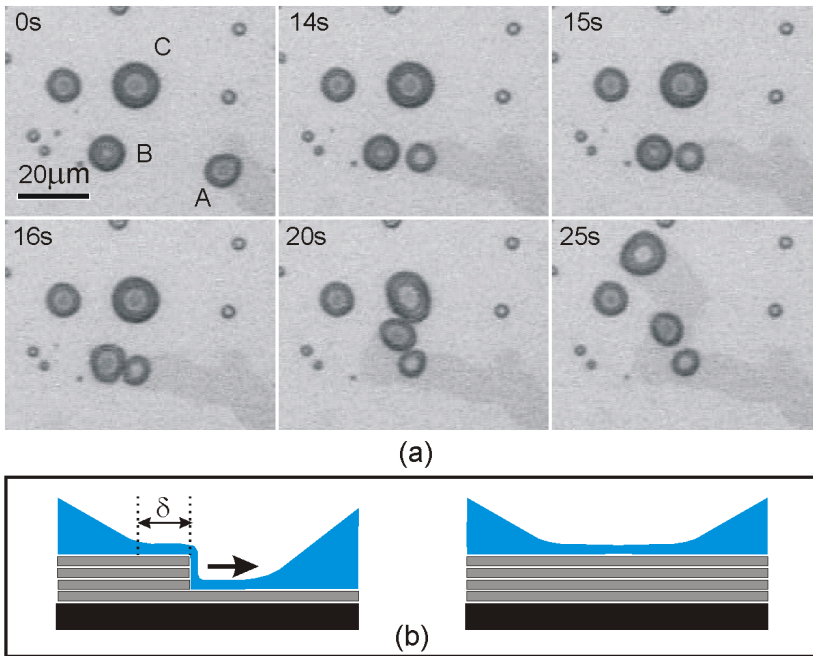


Figure 6.20. Sequence of optical microscopy images, showing the droplet-to-droplet triggering of movement during solidification of C_{36} on mica (a), and a possible mechanism explaining why the droplets do not coalesce (b). Note that the drops which move are distorted, i.e. their three-phase line does not have the usual (static) circular shape.

contact line (or in-between the front and rear contact lines) will grow very fast towards the leading front since there is plenty of undercooled liquid to supply the growth. On moving, the macroscopic contact line will always lag behind the solidifying front by a distance δ . Coming back to figure 6.20, when the distance between the solid front of a moving drop and the contact line of a static drop is small enough, the solidification front gets supply from both droplets leading to a faster advance of the solid front (left-hand side cartoon). As a result, the distance δ will increase and the first drop will slow down while the second will feed more and more the growth. Finally the second drop will start moving because the solid leading front is transferred to it while the first drop stops. The distance between the two drops will increase again and the droplets will not coalesce. If this mechanism is true, a question arises: why do the droplets move when the solid terrace exceeds the nominal area of the S-L interface underneath the drop? In other words, where is a asymmetric force field which drives the movement? A possible answer is that the liquid film in front of the drop is, on average, thinner (the solidifying front "sucks" molecules from it) than the one behind. As a result, the surface energy in front of the droplet is higher than the one behind.

This model allows us to estimate δ . A moving droplet will not detach from its leading solid terrace if the velocity of the macroscopic drop equals the velocity of the advancing solid terrace, i.e. the parameter δ is time independent (dynamic equilibrium, stationarity). The flux j supplying the growth and the velocity U of the advancing solid front are constant. Assuming a linear geometry, the flux (mass per unit time and unit length of the three-phase line) is related to the velocity of the droplets by

$$j = UH\rho_S = UNH_0\rho_S \quad (6.18)$$

where H and H_0 are the terrace thickness and the all-trans length of the molecule, respectively. If the transport is considered diffusional,

$$j = -D \frac{\Gamma_2 - \Gamma_1}{\delta} = \frac{DkH\rho_S}{\delta} \quad (6.19)$$

with D the diffusion coefficient, Γ_1 the surface concentration at the macroscopic contact line, Γ_2 the surface concentration at the growing front, and $k \equiv (\Gamma_1 - \Gamma_2)/H\rho_S$, (see also the equations A.28, A.29). Combining the equation 6.18 and 6.19 we get δ :

$$\delta = \frac{Dk}{U} = \frac{D_{app}}{2U} \quad (6.20)$$

The apparent diffusion coefficient, D_{app} was defined in the chapter 5 by the equation $(R_2 - R_1)^2 = D_{app}t$. For one monolayer and 0.3-0.5°C undercooling, the experimental value of D_{app} was $\approx 0.02 \mu^2/s$. In the case of running drops on mica, the thickness of the solid layer can be estimated to about 3ML and $D_{app,3ML} \approx 0.0067 \mu^2/s$. Thus, for the velocity of 1.5 $\mu m/s$, we get for δ a value of about 2.2 nm, i.e. about five repeat molecular spacings.

Qualitative analysis of the stability of the "running drop" regime with respect to the "terrace growth" regime

A qualitative model may consider two velocity functions $U(\delta, \Delta T, H)$ for the microscopic solidifying front velocity (U_1) and macroscopic contact line velocity (U_2). U_1 may depend on δ according to the following equation (see equation 6.20 in which $D_{app} \propto \Delta T/H$):

$$U_1 \propto \frac{\Delta T}{\delta H} \quad (6.21)$$

where H is the thickness of the growing solid terrace. A qualitative dependence of U_2 on δ can be obtained from the following considerations: (i) the velocity is proportional to the driving force; (ii) the macroscopic three-phase line can not move faster than the microscopic solidifying front, i.e. on decreasing δ there should be a value, $\delta = \delta_0$ for which the driving force is zero; (iii) for large values of δ the driving force decreases gradually to zero ($\delta \rightarrow \infty$ means symmetrical force field); (iv) in between the two limits the driving force reaches a maximum; (v) for any δ , the driving force increases with the magnitude of undercooling. To fit all these conditions, one can choose for instance the following relation:

$$U_2 \propto \Delta T \delta \exp(-a\delta) \quad (6.22)$$

where a is an adjustable parameter.

The graph (a) in figure 6.21 shows the qualitative dependence of the velocities U_1 and U_2 on δ for a terrace thickness of $2H$ and constant undercooling. Let us consider the two functions describing the growth of a $2H$ thick terrace (black solid and black dashed curves). The movement corresponds to a dynamic equilibrium (stationarity) if,

$$U_1 = U_2 \quad (6.23)$$

otherwise the system evolves increasing δ for $U_1 > U_2$ and $0 < \delta < \delta_A$ or decreasing δ for $U_1 < U_2$ and $\delta_A < \delta < \delta_B$. Hence, A is a (*meta*)stable point (stationarity).

6. Reversible (running) drops driven by the S-L phase transition

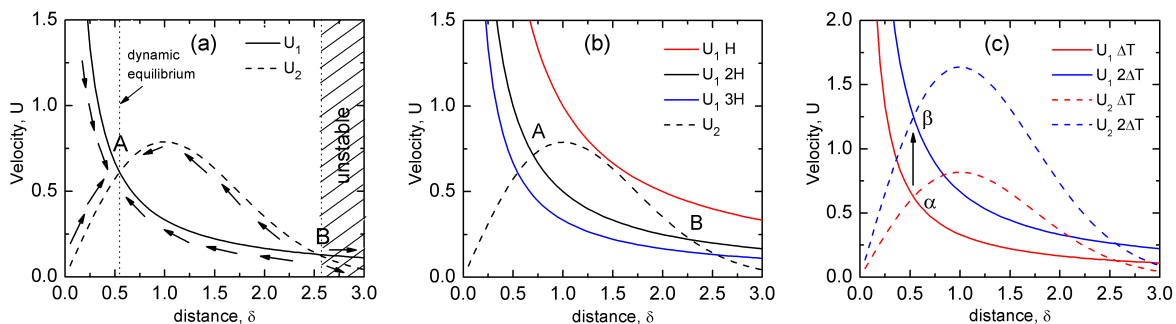


Figure 6.21. Velocities of the microscopic solidification front U_1 (solid lines) and of the macroscopic contact line U_2 (dashed lines) versus δ : (a) constant terrace thickness ($2H$, constant undercooling), (b) different terrace thicknesses (H , $2H$, $3H$, constant undercooling), and (c) constant terrace thickness ($2H$) at *different undercoolings*.

If $\delta > \delta_B$, the distance will increase and the system changes the behaviour from a "running drop" to a "spreading drop". The point B, although it fulfils the dynamic equilibrium condition, it describes an *unstable* regime since small fluctuations of δ may lead to either spreading regime or running regime of point A.

According to the equations for U_1 and U_2 considered above, U_1 (solid lines) decreases when the thickness H increases while U_2 is thickness independent. In graph (b) of figure 6.21 are plotted the velocity functions $U_1(\delta, H)$ for three thickness values H , $2H$, $3H$. In the case with terrace thickness H , U_1 and U_2 do not intersect each other and the droplet can solidify *only* by spreading. This may explain why solidifying running drops forming for instance only one solid monolayer were not observed.

In graph (c) of figure 6.21 are plotted two pairs of $U_1 - U_2$ curves for the same terrace thickness and two undercooling temperatures, ΔT (red) and $2\Delta T$ (blue). Since both U_1 and U_2 increase linearly with ΔT , the velocity describing the dynamic equilibrium ($U_1 = U_2$) increases linearly with undercooling, $U_B(2\Delta T) = 2U_A(\Delta T)$, as observed experimentally. The model does not explain why for a given thickness of the growing terrace, on decreasing temperature beyond a certain limit, the mechanism of solidification switches from the "running droplets" regime to the "terrace growth" regime. A further refinement of the model may consider the influence of pinning, droplet distortion, and solidification kinetics.

6.5. Discussion and conclusions

Long-chain alkane (C_{24} , C_{30} , C_{36}) droplets in contact with their own molecularly thin solid terraces can move on a planar solid substrate, as a result of an asymmetric force field. The movement is strongly temperature dependent and its direction can be reversed. Above the melting point droplets move consuming the solid whereas below T_{mp} they can recreate the solid structure. When only solid terraces are present, the melting starts from the terrace edge (step). The submicrometer-sized drops which nucleate at the edge move increasing their volume on the expense of the solid which is consumed. Both advancing and receding running drops move on the surface self-avoiding their own trails.

The velocity does not depend on the droplet size but increases linearly with both overheating tem-

perature and solid film thickness (number of molecular layers melting). This indicates that the driving force is the free energy gain upon melting or solidification. The driving force is balanced by viscous forces. Inertial forces do not play any significant role²⁰. Using the hydrodynamic model, the experimental slope of velocity vs. temperature can be translated into the slope of the driving force vs. temperature. The numerical result is in agreement with the value calculated considering the melting free energy as driving force. The same conclusion is confirmed quantitatively by analyzing droplets which are symmetrically stretched by the "melting force" given by the overheated solid film.

For the case when the droplets move consuming only part of the available solid layers, the results show that the position of the melting layer(s) with respect to the substrate surface is not important.

Defining a "reduced" velocity $\tilde{U} \equiv [U(\Delta T, N) - U_0]/N$, it was shown that all the data points, irrespective of terrace thickness, can be unified into a master curve with the equation $\tilde{U} = \tilde{s}\Delta T$.

The movement driven by *solidification* competes with *terrace growth* and therefore occurs only under specific conditions. A model based on the presence of the solid terrace underneath the moving drop has been proposed. The model explains qualitatively the features of solidifying running drops, especially the observed two orders of magnitude lower velocity²¹ as compared with melting-driven running drops, the non-coalescing of the drops which initiate the movement from one another and why moving drops forming only one molecular layer were not observed.

Within the experimental errors, the three studied alkanes do not reveal a systematic effect of the chain length.

²⁰Upon changing their moving direction, the initial velocity is extremely fast recovered i.e. the increase of velocity with temperature results from the increase of the driving force and not from acceleration.

²¹At the same absolute deviation from the melting point

7. Overheating aspects of solid alkane films of different thickness

7.1. Introduction

The previous two chapters presented the behaviour of long-chain alkanes close to the bulk melting temperature. Thin alkane terraces are not stable at temperatures slightly above the bulk melting point and can relax either by:

(i) the *dissolution of the terrace*, i.e. the reversed process of terrace growth; this occurs by alkane transport from the terrace edge to a macroscopic drop, via a thin "liquid-like" film present in-between, on top of the surface frozen monolayer (see sections 5.9 and 5.10 of the chapter 5), and

(ii) *running drops*, which travel on the area covered with the terrace and "eat" the solid on their way (see chapter 6).

In the previous chapters mainly the kinetic features were analyzed and different mechanisms of solidification/melting were proposed.

Some questions are still not completely answered: (i) why the solid, ordered alkane films melt (continuously) by either "dissolution of the terraces" or as "running droplets" (chapter 6) and not *entirely, all-over the surface at once*; (ii) how the system "chooses" between the two melting mechanisms and what are the relevant parameters?; (iii) what is the overheating limit (the maximum temperature at which the film is still solid).

This chapter analyzes the experimental evidence from another perspective, i.e. the overheating aspects (see section 2.5 of chapter 2).

It is unquestionable that, upon increasing the temperature, the system should change from a solid, ordered film of different thicknesses, which "wets completely" the surface frozen layer (equilibrium state below its melting point), to macroscopic, partially wetting drops (equilibrium state above the critical temperature)¹. The topology of three states are presented in figure 7.1. Both (thin) "completely wetting **Solid Monolayer** in contact with the **Vapour phase**" (**SoMoV**) and thick "completely wetting **Solid Multilayer** in contact with the **Vapour phase**" (**SoMuV**) initial structures experience a dilemma upon melting: to *dewet upon melting* or *melt into a film which afterwards dewets* the surface?

The main goal is to explain the relation of causality between *structure* \rightarrow *properties* \rightarrow *behaviour* (*the thermodynamics and kinetics aspects*). An interesting interplay between the two opposing thermodynamic forces (the melting free energy and capillary forces) is found as possible explanation for the evolution of the system above T_{mp} .

¹The term "equilibrium" describing partially wetting drops is not entirely correct since large drops can grow on the expense of the small ones (Oswald ripening) either via the vapour phase or via a molecular film present on the surface which allows the drops to "communicate". However, for the time scale of the experiments discussed here, such a process can be easily discarded.

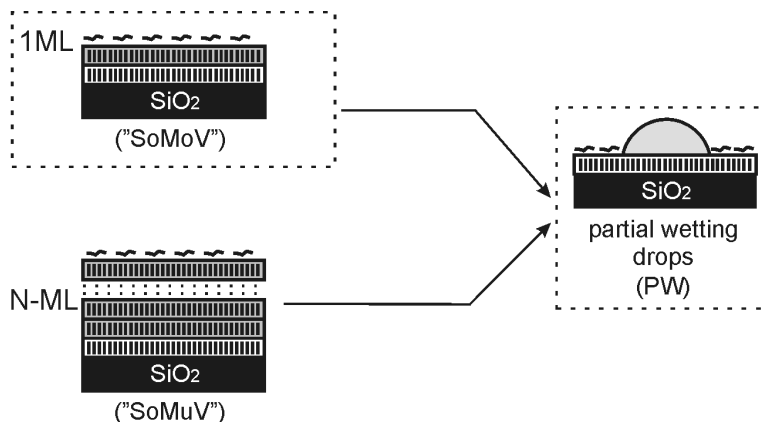


Figure 7.1. The melting process of alkane films implies the *phase transition* itself and the change of the wetting regime from "completely wetting" mono- and multilayer solid terraces to *partially wetting* (PW) drops. (SoMoV) stands for "completely wetting *Solid Monolayer in contact with the Vapour phase*". (the surface frozen layer not counted since it does not melt in the temperature range of interest) while (SoMuV) stands for "completely wetting *Solid Multilayer in contact with the Vapor phase*".

7.2. Thermodynamic considerations for melting of a monolayer thick solid terrace

Let us consider as reference states two of the equilibrium structures depicted in figure 7.1:

(i) a "completely wetting" solid monolayer in contact with the vapour phase (SoMoV), for temperatures below the melting point, and

(ii) partially wetting (PW) drops of *equal size* above the melting point. The size of the droplets is fixed to R_0 (radius of the circular three-phase line) which is set for simplicity to $\approx 5\mu\text{m}^2$. With this size the drops are considered in the following "macroscopic"³.

Furthermore, for all the states the *mean*⁴ molar surface concentration, Γ_m (= number of moles number per unit surface area of the substrate), is also fixed to a value Γ_m^{01} which corresponds to an almost⁵ complete solid monolayer⁶. By definition, this parameter does not distinguish between solid and liquid states. It can be calculated with the following formula:

$$\Gamma_m^{01} = \frac{H_0 \rho_S}{M} \approx 8.35 \cdot 10^{-6} \frac{\text{mol}}{\text{m}^2} \quad (\text{for } C_{30}) \quad (7.1)$$

All the numerical values will be calculated in the following using C_{30} as reference alkane.

As proper parameter describing the stability of different states is chosen the *Gibbs free energy per unit area of the substrate surface*. This intensive parameter denoted in the following by g contains

²The typical values of this parameter are in this order of magnitude for both types of experiments described in the previous chapters: the reversed process of terrace growth above the melting point and "running droplets".

³Although the interfacial contributions are not discarded, the intensive quantities describing this state like molar entropy, molar volume, molar enthalpy, etc. are similar to the bulk values.

⁴With the meaning of amount of alkane per unit area when the $\sqrt{\text{unit area}}$ is much larger than any relevant lateral sizes of the structures of interest.

⁵The layer is considered almost complete to allow the presence of steps.

⁶The surface frozen monolayer is not taken into account; Γ_m^{01} refers only to the excess alkane (monolayer terrace or partially wetting drops) on top of the surface frozen monolayer.

both *bulk* and *surface*⁷ contributions and refers *strictly* to the above specified amount of alkane per unit surface area of the substrate. Its definition is

$$g \equiv \frac{G}{A} = \left(\frac{\partial G}{\partial A} \right)_{T,p,\Gamma_m^{01}} \quad (7.2)$$

where G is the Gibbs free energy of the excess alkane⁸ with the fixed mean molar surface concentration Γ_m^{01} . A is the sample surface area. It is important to note that according to the conditions defined above, for each considered state, the variation of Gibbs free implies the variation of area and amount of alkane considered.

Any energetical contribution due to long or short range molecular interactions is completely ignored.

The melting point T_{mp}^* of the completely wetting solid monolayer terrace (SoMoV) into partially wetting drops of fixed size (PW) is defined⁹ as the temperature at which the Gibbs free energy per unit area g is the same for the two reference states,

$$g^{SoMoV}(T_{mp}^*) = g^{PW}(T_{mp}^*) \equiv g_0^{SV} \quad (7.3)$$

The superscript SV denotes the solid-vapour interface since both structures expose (mainly) solid surface to the vapour phase.

The diagram in figure 7.2 shows the theoretical variation of g with temperature for the different states. The line marked (i) describes the structure which is stable below T_{mp}^* , i.e. the solid monolayer, (SoMoV). Its equation is,

$$g^{SoMoV}(T) \approx g_0^{SV} - S^{SoMoV}(T - T_{mp}^*) \quad (7.4)$$

where S^{SoMoV} is the entropy of the solid monomolecular layer per unit area.

The line (ii) describes the temperature dependence of g for the state (PW) and has the equation:

$$g^{PW}(T) \approx g_0^{SV} - S^{PW}(T - T_{mp}^*) \quad (7.5)$$

where S^{PW} is the total entropy per unit area of the partially wetting liquid drops. Its value must be very similar to the bulk entropy, ($S^{PW} \approx S_L^{bulk}$) of the liquid alkane since the droplets are considered "macroscopic" (see footnote 3). The difference between equation 7.5 and equation 7.4 represents the temperature variation of the energy which drives the transition between the two states,

$$\Delta g^{SoMoV,PW} = -(S^{PW} - S^{SoMoV})(T - T_{mp}^*) = -\Delta S_{(i),(ii)}(T - T_{mp}^*) \quad (7.6)$$

Ocko et al. [102] found that the values of the entropy change upon formation of the surface frozen layer is very similar to the value associated with the transition *bulk rotator phase* \rightarrow *liquid*. Assuming

⁷The states discussed in the following may change the nature or shape of the interfaces; only the interfaces in which the considered amount Γ_m^{01} is part are relevant here.

⁸Excess has the meaning of the amount of alkane which is on top of the surface frozen layer.

⁹For bulk, the thermodynamic melting point is defined by the equality of free energy per molecule (chemical potential or molar Gibbs free energy) in solid and liquid phases, respectively. The case discussed here is special because the considered potential g contains energetical contributions from the interfaces.

that our solid film has similar properties as the surface frozen layer at the liquid/vapour interface, we can approximate the value of $\Delta S_{(i),(ii)}$ with the entropy change upon melting of the bulk rotator phase,

$$\Delta S_{(i),(ii)} \approx \Delta S_{SL}^{bulk} \approx \Delta S_{SF,L} = 1.72 \frac{mJ}{m^2 \cdot K} \quad (7.7)$$

The line describing the temperature variation of the g potential for a completely wetting (CW) film with the same Γ_m^{01} would be shifted relative to the line (ii) with the positive quantity

$$\Delta g^{CW}(T) = g^{CW}(T) - g^{PW}(T) \approx [1 - \cos\theta(T)]\gamma_{LV}(T) \quad (7.8)$$

where θ represents the equilibrium contact angle of the drops in the partially wetting state and γ_{LV} the surface tension of the liquid alkane. The approximation comes from the fact that the L/V and S/L interfaces are replaced almost entirely by the S/V interface (upon dewetting the areas of the S/L and L/V interfaces are much smaller than the newly created S/V interface). (A more detailed discussion of this approximation is presented in the section A.5 of the appendix). A further approximation,

$$\Delta g^{CW}(T) \approx [1 - \cos\theta(T_{mp}^*)]\gamma_{LV}(T_{mp}^*) = const. \quad (7.9)$$

discards the temperature variation¹⁰ of both γ_{LV} and θ since the temperature range of interest is very small. The numerical value of Δg^{CW} calculated for C₃₀ is ≈ 1.72 mN/m.

The line (j) corresponds to a monolayer solid film immersed in its own (bulk) liquid melt "completely wetting **Solid Monolayer in contact with (its own) Liquid phase**", (SoMoL). It runs almost¹¹ parallel but below the line (i) due to the replacement of S/V interface by S/L,

$$\Delta g^{IM}(T) = \gamma_{SL}(T) - \gamma_{SV}(T) = -\cos\theta(T)\gamma_{LV}(T) \approx -\cos\theta(T_{mp}^*)\gamma_{LV}(T_{mp}^*) \approx 26.3 \left[\frac{mJ}{m^2} \right] \quad (7.10)$$

which has the numerical value of ≈ 26.3 mJ/m². Due to the same reason, the line (jj) is shifted below (ii) with the same quantity. The temperature (T_{mp}^{**}) corresponding to the intersection (j) and (jj) defines the melting point of the *immersed* terrace, i.e. the transition from (SoMoL) to a completely¹² liquid film of the same amount per area, Γ_m^{01} (the dashed line in the cartoon represents a formal L-L interface which obviously does not cost any energy). T_{mp}^{**} must be T_{mp} , the melting temperature for bulk¹³. On the other hand, T_{mp}^{**} should be the same as T_{mp}^* since the lines (i) and (j) and (ii) and (jj), respectively, run parallel, and are shifted with the same quantity. Hence,

$$T_{mp}^* \approx T_{mp}^{**} \approx T_{mp} \quad (7.11)$$

This is as expected if long range forces are discarded!

The above relation comes to support the assumptions which were considered in the chapter 6 i.e.:

¹⁰The value of $\partial\gamma_{LV}/\partial T$ (≈ 0.1 mNm⁻¹K⁻¹ [100]) is much smaller than $\gamma_L(T_{mp})$ itself (≈ 28.6 mNm⁻¹ at the melting temperature), and barely varies with the chain length; it was observed experimentally that also the temperature variation of θ in the temperature range of interest is small.

¹¹The difference $\gamma_{SL} - \gamma_{SV} = -\gamma_{LV}\cos\theta$ contains the same ingredients as the Δg^{CW} line; hence, based on the same arguments its temperature dependence is discarded.

¹²Except the surface frozen monolayer.

¹³By replacing the SiO₂ substrate with a semi-infinite alkane solid the system will correspond to L(bulk)/S(bulk) interface.

(i) a solid terrace underneath the liquid drop is not thermodynamically stable above T_{mp} (section 6.3.5) and,

(ii) a solid terrace will be stable underneath the drop if the temperature is below T_{mp} (section 6.4.3).

7.2.1. The (absolute) thermodynamic limit of overheating, T^{MN}

The intersection between the line (i) describing the state (SoMoV), and line (cw) describing the complete wetting state (CW) gives the (absolute) thermodynamic limit of overheating, ΔT^{MN} . T^{MN} is derived from:

$$g^{SoMoV}(T) = g^{CW}(T) \quad (7.12)$$

which is equivalent to (see equations 7.6 and 7.9),

$$-\Delta g^{SoMoV,PW}(T) = \Delta g^{CW}(T) \quad (7.13)$$

The solution is:

$$\Delta T^{MN} = -\frac{\Delta g^{SoMoV,PW}}{\Delta g^{CW}} \approx 1^\circ C \quad (7.14)$$

This is consistent with the experimental evidence, i.e. the melting mechanism of 1ML terrace via running drops was not observed at higher overheatings than $\approx 0.9^\circ C$ (see section 6.3.3 in chapter 6)¹⁴.

7.2.2. Hierarchy of the melting mechanisms

Depending on ΔT ¹⁵, a hierarchy of three melting mechanisms of a monomolecular solid terrace has been observed experimentally. This hierarchy is consistent qualitatively and quantitatively with the thermodynamic approach. The figure 7.3 shows schematically these three melting mechanisms in a diagram which displays overheating temperature – degree of solid → liquid conversion (time). The sequence (a) → (b) → (c) describes the reversed process of terrace growth (terrace dissolution), the sequence (α) → (β) → (γ) describes the melting via running drops and (1) → (2) → (3) the sequence of "massive nucleation" and growth of the liquid phase followed by dewetting (i.e. the melting process is faster than dewetting). In the following are summarized the features of the three melting mechanisms.

Terrace dissolution (the reversed process of terrace growth)

Immediately above T_{mp} (see figure 7.2 but below T^{RD} (0 to $\approx 0.4^\circ C$ overheating) the monolayer terrace is not stable. The blue triangle describes by its y dimension the magnitude of the driving force of melting and by its x dimension the overheating range in which the system relaxes via terrace dissolution. Depending on whether a liquid drop is present¹⁶ or not on the surface, the system is *unstable* or *metastable*, respectively. In the first case the alkane molecules will travel from the terrace

¹⁴Or, terms of velocities, the maximum velocity of running drops does not exceed the dewetting velocity i.e. *running drops can not move faster than the dewetting front*, (sections 6.3.3 and 6.3.7 in chapter 6).

¹⁵As the equation 7.6 shows, the magnitude of the thermodynamic driving force for melting $\Delta g^{(SoMoV),(PW)}$ increases with the extent of overheating.

¹⁶This is the case for the experimentally observed (chapter 5) terrace dissolution mechanism.

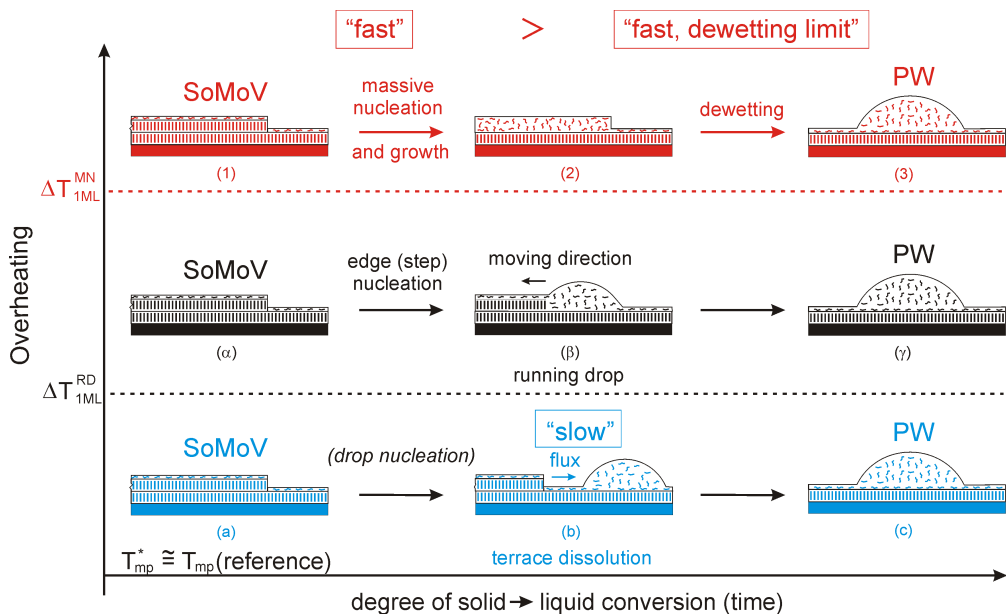


Figure 7.3. Three melting mechanisms observed and predicted by the thermodynamic considerations for melting of a solid alkane terrace (exemplified for the case of 1ML) in a diagram *overheating temperature vs. degree of solid \rightarrow liquid conversion (time)*: path (a) \rightarrow (b) \rightarrow (c) corresponds to the reversed process of terrace growth, path (α) \rightarrow (β) \rightarrow (γ) to "running droplets", and path (1) \rightarrow (2) \rightarrow (3) to (first) complete melting followed by dewetting.

edge to the macroscopic drop through the liquid film in between. The kinetics of this process is *slow* because the transport¹⁷ through the film is *not efficient*. The excess free energy is dissipated in the molecularly thin film.

The metastable case refers to the formation of an *external*, partially wetting, (macroscopic) drop. This process was not observed experimentally and can be explained by the high nucleation barrier of the formation of a liquid drop.

Running drops i.e. "solid dewetting"

As shown in chapter 6, this melting mechanism occurs in the overheating range $T^{RD} - T^{MN}$ (≈ 0.4 to $\approx 1^\circ\text{C}$). The thermodynamic driving force is higher in this temperature range than in the case of terrace dissolution and increases with overheating. This is reflected in the increase of running drop velocity with increasing temperature. The experimental value of the temperature corresponding to zero velocity¹⁸ of a running drop¹⁹ is not T_{mp}^* . This contradicts apparently the theoretical analysis because the drops are expected to move immediately above T_{mp}^* since by droplet movement the system decreases its free energy. Distortion and pinning may explain the shift of T^{RD} with respect to T_{mp}^* .

The initial stage of a running drop is the formation of drops attached to the step by accumulation of the liquid which wets the terrace step, a process similar to the Rayleigh instability. The formation

¹⁷The molecular flux depends on the distance between the terrace edge and the macroscopic drop.

¹⁸This value is estimated extrapolating the velocity of the running drops to 0 in the linear dependence velocity-overheating.

¹⁹The size of a running drops considered here is macroscopic i.e. the T^{RD} is not connected to a nucleation barrier.

of droplets attached to the terrace step is a nucleated process (see section 6.2 in chapter 6) and the nucleation barrier is overcome due to overheating. The melting via running drops is a *more efficient* way compared with the transport of alkane molecules via a molecularly thin film. The excess free energy is spent on viscous dissipation.

Massive nucleation and growth

Massive nucleation and growth of the liquid phase within the solid terrace is expected to occur above the thermodynamic limit, T^{MN} i.e. $\approx 1^\circ\text{C}$ overheating. The evolution of the system is expected to follow the sequence (1) \rightarrow (2) \rightarrow (3) in the figure 7.3 i.e., first melting and then dewetting.

In order to observe the massive nucleation and growth of the liquid phase, the system must be heated fast enough to reach the temperature ΔT^{MN} before the entire structure is melted via the running drops. One can estimate the minimal heating rate taking into account the average lateral size of the terraces, the slope of velocity vs. temperature and the minimal value of the temperature at which massive nucleation and growth takes place. The time τ needed to consume the entire solid structure via running drops is given by the condition:

$$\int_0^\tau U(t)dt = l_{terr} \Leftrightarrow \int_0^\tau s_1 r_h t dt = l_{terr} \Leftrightarrow \tau = \sqrt{\frac{2l_{terr}}{s_1 r_h}} \quad (7.15)$$

where l_{terr} is an average lateral size of the terraces (per nucleated drop), s_1 is the slope of the running drop velocity vs. temperature ($s \equiv \partial U/\partial T$) and r_h is the heating rate ($\equiv \partial T/\partial t$). The temperature at which the massive nucleation and growth occurs must be reached within a time shorter than τ . This condition,

$$\frac{\Delta T^{MN}}{r_h} < \tau, \quad (7.16)$$

gives a minimal rate of heating of

$$r_h > \frac{s_1 (\Delta T^{MN})^2}{2l_{terr}} \quad (7.17)$$

With the experimental values $s_1 = 1000 \mu\text{m}/(\text{s}^\circ\text{C})$, and $l_{terr} \approx 100 \mu\text{m}$ the minimal heating rate would be $\approx 5^\circ\text{C}/\text{s}$. This is consistent with experiments²⁰ where the samples (kept at temperatures between T_{mp} and T^{RD}) were illuminated with a electronic flash when the superficial heating rate is extremely high.

7.3. Overheating of thick terraces

Figure 7.4 shows a thick C_{24} terrace progressively melting on increasing temperature. The terrace thickness calculated from mass conservation is $\approx 240 \text{ nm}$. The melting starts from the stepped contour of the terrace forming an uniform liquid "stripe" which gets wider and wider on increasing temperature. On further heating, the liquid stripe eventually destabilizes forming two distorted droplets attached to the step. Regions with higher curvature of the step contour are preferred for the droplet

²⁰In the case of 1ML solid terrace, only the transition *solid* \rightarrow "normal" *dewetting liquid film* was observed, i.e. no running drops.

formation. The droplet increases its volume on expense of the melting solid and finally the entire solid becomes a liquid droplet. Detailed observation of the movement of such drops give evidence that extremely small changes of temperature near T_{mp} can generate advancing or receding droplet movement, driven by solidification or by melting. The direction of the movement can be reversed within a *much smaller temperature range* ($\approx 0.02^\circ\text{C}$) as compared with the case of droplets connected to a thin terrace of few molecular layers where a significant hysteresis of about 0.5°C can be observed.



Figure 7.4. Sequence of optical microscopy images showing the melting of a ≈ 240 nm thick C_{24} terrace ($10\mu\text{m}$ scale bar). In the first three images, the liquid stripe wetting the stepped perimeter (white contour) widens and then two distorted drops form in the regions of highest in-plane curvature. Finally the entire structure is molten.

The optical microscopy images in figure 7.5 present the evolution of a thick ($\approx 150\text{nm}$) C_{24} terrace upon heating. The corresponding overheating temperatures²¹ are shown for each image together with the elapsed time from the beginning of the experiment. In the first image (0.0012°C , 0 s)²² the solid terrace is in its initial shape. After 14.5 s, at about 0.0877°C above T_{mp} , the liquid stripe surrounding the terrace destabilizes forming a drop which moves consuming part of the terrace. The third image, (0.1100°C , 24 s) is a snap-shot of the droplet moving with a velocity of about $2.45\mu\text{m/s}$. In the next image (0.0973°C , 26 s) the drop was just stopped due to a slight decrease of the temperature. On further decrease of the temperature, 0.0940°C , 31.1 s, a tendency of movement backwards is observable but only the wetting line connected to the terrace moves and not the one on the SF monolayer. In this case the droplet seems to be "compressed" between the terrace-connected wetting line and the three-phase line on the SF layer which seems to be pinned. After the temperature is raised again (0.1118°C - 44 s), the droplet moves consuming the terrace with a velocity of about $2.5\mu\text{m/s}$. At 0.0899°C and 48.2 s the drop just started to move very slowly "backwards", re-creating the terrace. In the final picture, at 0.0652°C the velocity of the solidifying drop reached $3.2\mu\text{m/s}$. It is important to point out that the droplet can advance stepwise upon a stepwise *change* of the temperature, passing through static *metastable* configurations! In other words, to avoid melting²³ the entire structure it is not necessarily needed to decrease the temperature. These static states at slightly different temperatures can have a lifetime on the order of minutes.

Another important observation is that, in addition to the melting as a result of droplet advancement,

²¹The temperature was calibrated with respect to the melting point of a macroscopic, amorphous solidified drop; what is considered important in this experiment is not the accuracy of calibration but how extremely small temperature variations (relative values) influence the system.

²²This is of course not an absolute, correct number, it is only the number taken from temperature read-out (resolution) and reflects only the change. For instance $.0010 \rightarrow .0012$ means increase of the temperature.

²³At constant temperature, as soon as the drop attached at the terrace step becomes "macroscopic", based on simple thermodynamic considerations the entire solid is expected to melt.

thick terraces melt also at the terrace step, all along the contour of the terrace. The resulting liquid is "pumped" towards the drop through the liquid stripe surrounding the terrace which preserves a quasi-constant width. This second mechanism of melting of thick terraces can be clearly observed in figure 7.5. At the beginning of the experiment, the lower part of the terrace has a neck. By comparing the second and the third images, a decrease in area of the lowest part of the terrace can be observed. On decreasing temperature the process is stopped and restarted when the temperature increases again (see fifth and sixth images). The same effect leads also, on melting, to a depletion of the solid material (decrease of the terrace width) immediately ahead of the advancing droplet front. This second transport/melting mechanism is apparently non-reversible i.e. at lower temperatures when the drop moves solidifying, the liquid is not pumped back to solidify all-around the terrace. The non-reversibility can be explained by comparing the Laplace pressure (the most probable driving force) within the liquid stripe with the pressure inside the drop. Thus, p_L in the liquid stripe can be much higher (high curvature, in the order of H^{-1}) than its corresponding value in the drop while to pump back the liquid, the maximum available driving force is limited to the absolute value of p_L in the drop. A second effect which may explain the non-reversibility is that, by decreasing the temperature, the available section through which the liquid is transported decreases. Careful observations of the melting via the second mechanism revealed that regions having higher in-plane curvature melt faster. The transport through the liquid stripe which wets the terrace step is expected to occur also for terraces of few monolayers but the kinetics is much slower making the process negligible.

It is important to note the distorted²⁴ shape of the droplet when it is either stationary or moving. The distortion is higher when the drop moves. The extra free energy cost associated to the distortion acts as a *free energy reservoir* which, when the droplet moves, fuels the movement together with the free energy gain on melting/solidification. A second important observation is that the wetting line connected to the terrace has a much smaller curvature in the *sample plane* than anywhere else. A non-moving drop is characterized by the same Laplace pressure (p_L) everywhere inside the drop. Moreover, fast equilibration of p_L can be considered for drops moving at low velocities (in the order of $\mu\text{m/s}$). The Laplace pressure is proportional to the total curvature, $r_1^{-1} + r_2^{-1}$ where r_1 and r_2 are the two main radii. Let us consider the plane P_1 (see 7.7) defined by: (i) the z direction perpendicular to the sample plane intersecting the the surface of the droplet in its highest point and (ii) the direction of movement x , and associate to its intersection with the drop surface the main curvature r_1^{-1} . A second plane P_2 is perpendicular to P_1 intersects the droplet surface and defines the second main curvature r_2^{-1} . Since for our experimental conditions the Laplace pressure is position independent, for both static and moving drops at low velocity, the curvature r_1^{-1} must reach its maximum in the middle point of the wetting line connected to the terrace, while r_2 has in the same point a larger value. This observation is consistent with the tendency of the drop to *approach its equilibrium contact angle* everywhere along its contact line.

Forces which may play a role in the melting/solidification behaviour of thick terraces

Different forces affecting the melting/solidification behaviour may be considered:

- (i) **Melting force.**

²⁴With respect to the spherical cap shape which corresponds to lowest superficial free energy.

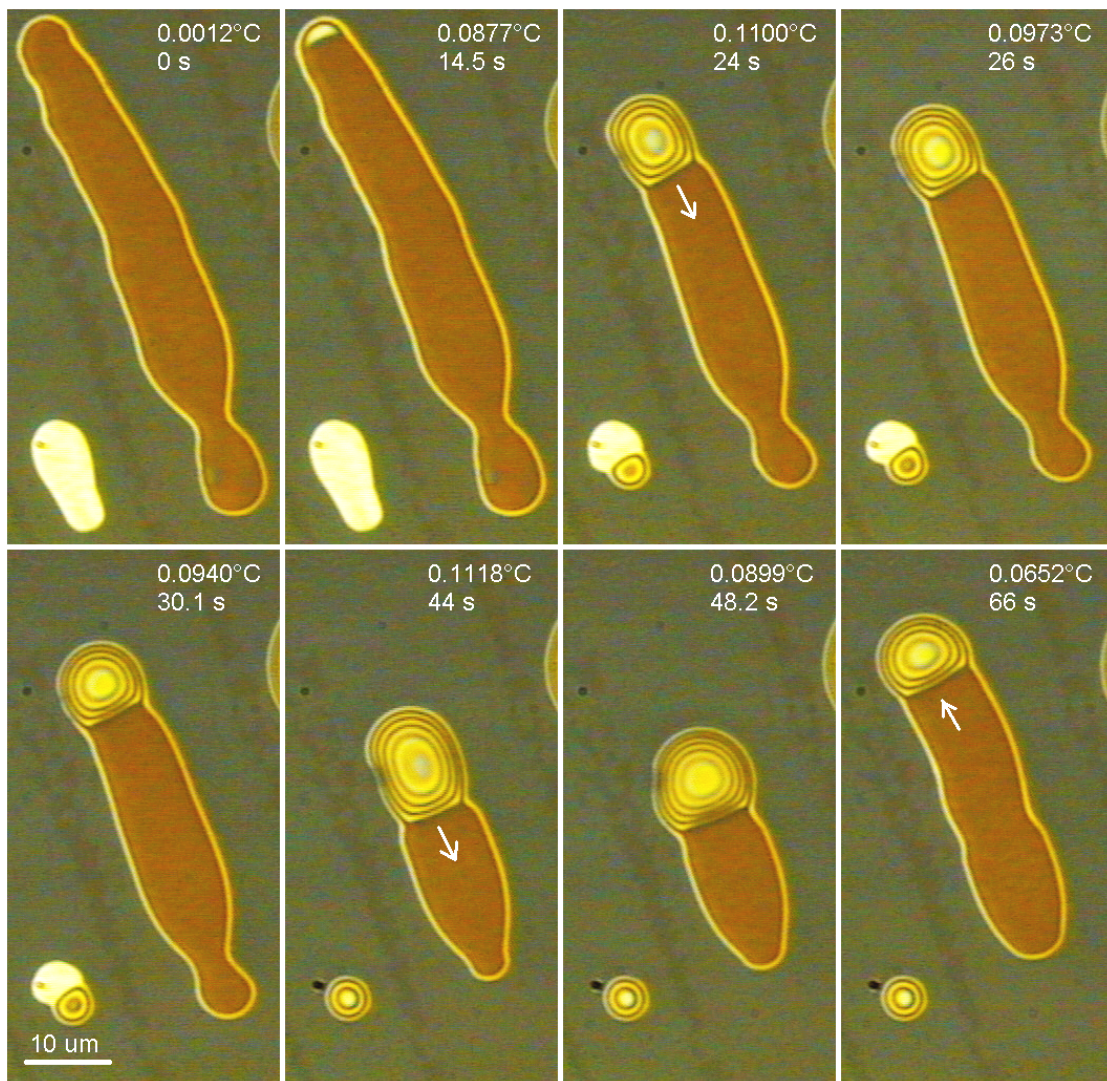


Figure 7.5. Reversible movement of a C_{24} droplet connected to a thick terrace when the sample is slightly heated and cooled within a temperature interval of about 0.03°C .

A melting/solidification force²⁵,

$$\Delta F_{adv,rec}(\Delta T)(\equiv \Delta \gamma_{fus}^N(\Delta T)) = \tau_{fus}^{1ML} \Delta T_{adv,rec} N \quad (7.18)$$

where $\Delta F_{adv,rec}(\Delta T)$ is the difference in force (per unit length) given by the free energy of melting/solidification which corresponds to ΔT , $\gamma_{fus}^N(\Delta T)$ is the melting/solidification "tension" as discussed in chapter 6, section 6.3.5, N the number of layers in the solid terrace and τ_{fus}^{1ML} the slope of the melting/solidification tension with temperature. With $\gamma_{fus}^{1ML,C24} \approx 1.4 \text{ mN}/(\text{m}^\circ\text{C}\cdot\text{ML})$, $H = 150\text{nm}$ ($\approx 47\text{ML}$), $\Delta T_{adv,rec} \approx 0.003^\circ\text{C}$ (the temperature difference which corresponds to the forth and fifth images in figure 7.5, i.e. between two static situations) we get $\Delta F_{adv,rec} \approx 0.2 \text{ mN}/\text{m}$.

(ii) **Pinning and distortion.**

In the graph (a) of figure 7.6 are plotted the approximate values of droplet contact angles θ_F (front), θ_R (rear). Note that the "front" and "rear" terms were chosen relative to the movement on solidification. The contact angle values are calculated from the height of the droplet (deduced from the number of interference rings), height of the terrace and the horizontal distances between the two contact lines and the droplet center, assuming circular shapes with different r_1^{-1} curvatures for the front and back parts of the drop. As reference, the average value of the contact angle in the same temperature range, on the same sample, for three spherical-cap shaped drops (without contacting a solid terrace) was $17.86 \pm 0.74^\circ$.

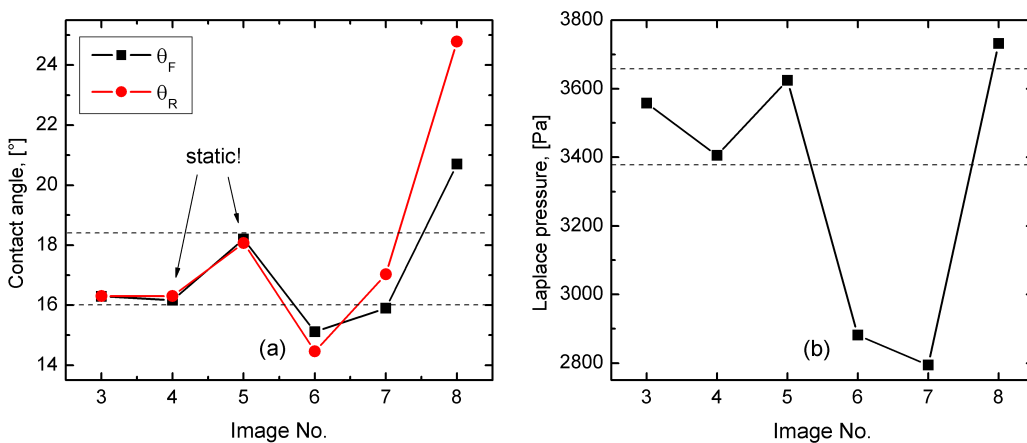


Figure 7.6. Estimates of "front" and "back" contact angles (a) and Laplace pressure values (b) corresponding to the images 3–8 of the figure 7.5.

The approximate values of θ_F and θ_R corresponding to the forth and fifth images allow us to estimate the values of the *pinning forces*. Thus, the change of the front (rear) contact angles when the drop is about to move consuming the terrace ($\approx 16^\circ$) and to move building it again ($\approx 18^\circ$) corresponds to a change in the horizontal force field (per unit length) of about $0.3 \text{ mN}/\text{m}$.

A comparison between the two results (melting/pinning forces) suggests that these two forces balance each other.

²⁵The solidification facet of the crystal acts as a piston driving the drop back and forth $\Delta F_{adv,rec}$ can be calculated in the same manner as for the thin terraces (see 6.3.5)

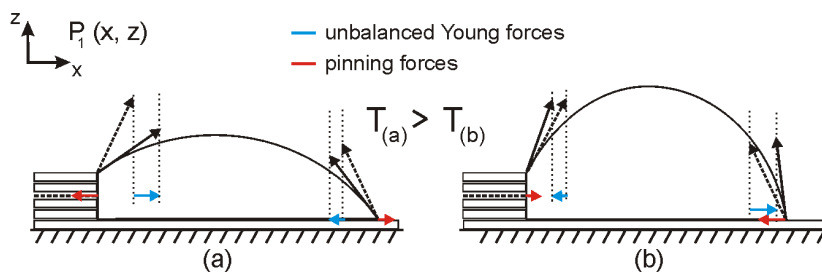


Figure 7.7. Lateral view (section) of a drop attached to a thick terrace showing the balance between *pinning forces* and *unbalanced Young forces*: (a) static situation when the terrace tends to melt (a) and to solidify (b).

”Step” force.

In section A.6 of the appendix is derived an expression of the unbalanced Young force which will drive a liquid drop sitting on a solid stepped structure towards the equilibrium configuration (attached to the solid step edge but without the solid underneath). Instead of a spherical cap shaped drop (3D) a cylindrical ridge (2D) is considered. The estimated force (per unit length) is ≈ 0.5 mN/m and does not depend on temperature. This estimate means that the drop would be attached to the step and not sitting (partly) on top of the terrace, i.e. the result supports the assumption that the moving drop at the edge of the solid alkane terrace does not have solid underneath.

The behaviour and the conditions for moving drops on *solidifying* are different whether the terrace which is formed is thin (i.e. few molecular layers), or thick (in the order of few tens of layers). The following features describing moving drops connected to a thick terrace suggest that the mechanism of movement is different compared to the one previously described for drops connected to thin terraces: (i) the contact angle at the wetting line connected to the terrace varies significantly for extremely small temperature changes; (ii) the temperature at which the movement occurs is closer to the melting point²⁶; (iii) the droplet can move with relatively high velocity. The previous scenario²⁷ can not account for all these differences. Most probably the difference consists in the position of the terrace step with respect to the wetting lines. In the case of thick terraces, the droplet is attached to the step²⁸ with its rear wetting line while in the case of thin terraces the solid is present under the liquid drop moving slightly ahead of the front wetting line.

Together with pinning effects, this configuration may explain why, a ”large” droplet (with a size much larger than the corresponding critical size) attached to an overheated thick terrace, can be manipulated and even stopped in different positions by slight changes in temperature (in this conditions the total free energy of the system is expected to decrease continuously until the entire solid is molten). Figure 7.7 presents schematically, for static situations, the balance between the pinning forces and unbalanced Young forces for the case of an elongated drop just before it moves driven by either melting (left cartoon) or solidification (right cartoon). Considering the pinning effects which are indeed observed experimentally (see the forth and fifth images of figure 7.5 which correspond to static configurations) it is possible to explain why the droplet stops although it is overheated.

(iii) Laplace pressure and the melting point (*Clapeyron equation*).

²⁶This comes to support the supposition considered for the case of *melting-driven* running drops eating thin terraces i.e. the terrace is not present underneath the drop.

²⁷See section 6.4.3 in chapter 6.

²⁸Other experiments showed that the solid terrace can be present in-between the front and rear wetting lines; in that cases, when the solidification front touched the front wetting line, the drop movement stopped.

According to the Clapeyron equation, the equilibrium melting point is changed when the pressure changes,

$$dT = \frac{\Delta V_{SL}}{\Delta S_{SL}} dp \approx 3 \cdot 10^{-7} dp [^{\circ}C] \quad (7.19)$$

where ΔV_{SL} and ΔS_{SL} are the molar volume and entropy change upon melting. With the values for C_{24} : $5 \cdot 10^{-5} \text{ m}^3/\text{mol}$ and $\approx 170 \text{ J}/(\text{mol} \cdot ^{\circ}C)$, $dT/dp = 3 \cdot 10^{-7} \text{ }^{\circ}C/\text{Pa}$. Graph (b) in figure 7.6 presents the Laplace pressure estimated from the two mean curvatures. An average Laplace pressure of $\approx 3200 \text{ Pa}$ shifts T_{mp} by less than $0.001^{\circ}C$; the relative change of p_L which is $\approx 200 \text{ Pa}$ has obviously a smaller effect (images fourth and fifth in figure 7.6). Based on these estimates we can discard the effect of Laplace pressure on the melting temperature.

7.4. Conclusions

Based on thermodynamic arguments, it is possible to explain the mechanisms of terrace melting (exemplified for the case of 1ML) which were described in the previous two chapters, i.e. "terrace dissolution", (chapter 5) "running drops" (chapter 6), and the overheating aspects of these processes. The approach takes into account to aspects of terrace melting: the *solid-liquid phase transition itself* and the *wetting transition* i.e. from a "completely wetting" solid to a partially wetting drop. These reference states are considered the equilibrium configurations below and above the melting temperature. An appropriate potential g (Gibbs free energy per unit area at constant coverage) is defined in order to describe the transition between the equilibrium states. This thermodynamic potential takes into account both "bulk" and interfacial energetical contributions. Long range van der Waals forces are ignored. The theoretical "phase diagram" g -temperature agrees reasonably well (including the numerical values) with the experimental findings.

A hierarchy (with respect to overheating temperature) of melting mechanisms is found: *terrace dissolution* \rightarrow *running droplets* \rightarrow *massive nucleation and growth* of the liquid phase into solid terrace followed by dewetting (melting faster than dewetting). Both thermodynamic and kinetic aspects are discussed in some details. A qualitative dependence between the degree of overheating and the kinetics of the corresponding melting mechanism is found: the higher the thermodynamic driving force the faster the rate of melting.

The second part of the chapter analyzes the melting mechanism of a "thick" (hundreds of nanometers) terrace. It is found that the melting process is continuous and reversible, i.e. by slight changes of the temperature the drop attached to the terrace step can advance (melt into the terrace) or recede (build again solid terrace). The influence of different types of forces which may influence the melting process are discussed. It is found (not surprisingly) that the driving force of the process is the melting/solidification free energy. Besides the "usual" viscous force which opposes the movement, pinning and distortion forced are relevant. They can explain why the droplet position can be controlled and fixed by slight changes of temperature.

8. Conclusions

In this work the behaviour of molecularly thin films of long-chain alkanes, tetracosane (C₂₄, triacontane (C₃₀), hexatriacontane (C₃₆)) at planar solid (SiO₂)/vapour interface was analyzed in detail.

Making use of optical microscopy, SAXR and AFM it was possible to explore both thermodynamic and kinetic aspects of the interplay between wetting behaviour and melting/solidification processes in molecularly thin alkane films.

Chapter 5 presents the growth of molecularly thin solid terraces starting from the three-phase line of partially wetting, undercooled drops ($T < T_{mp}$ = bulk melting point). It is shown that the main nucleation mechanism of terrace growth is *induction*, i.e. as soon as a solid terrace front touches the perimeter of an undercooled drop, this drop also starts to grow its "own" terrace. Via this "domino" effect, originating from the rear event of a single homogeneously nucleated terrace growth, eventually most drops grow solid terraces. The kinetics of growth is *diffusion-like*. The width (R) of the solid terrace surrounding the drops increases $\propto \sqrt{\text{time}}$. The experimentally accessible apparent diffusion coefficient defined as $D_{app} = R^2(t)/t$ (t = time) was found to decrease with increasing temperature. At T_{mp} , D_{app} is zero and above it the solid terrace material is transported back into the drop ("terrace dissolution"). In other words, the terrace can either grow or melt depending on whether the temperature is below or above T_{mp} , respectively. Solidified drops do not grow terraces under the same conditions as undercooled drops. By analyzing the layer-by-layer growth of terraces on top of each other it was possible to deduce the presence of a film of mobile alkanes everywhere on the sample "precursor film". This is the first experimental evidence for a precursor film coexisting with a partially wetting bulk phase. A model for the growth of the terraces considers as driving force the difference between two *local* chemical potentials, $\Delta\mu = \mu_{solid, edge} - \mu_{drop}$, i.e. between the terrace edge and the droplet perimeter.

The mechanism of melting/solidification of molecularly thin solid terraces via "running" drops is presented in chapter 6. It was found that upon small overheating (typically $< 0.3^\circ\text{C}$, the solid terraces melt via "terrace dissolution" (the reversed process of terrace growth by diffusion between terrace edge and bulk drop). At higher overheating, liquid alkane drops nucleate at the terrace edges (which act as defects). These droplets grow in size by moving into the solid terrace area, "eating" the solid and leaving behind an alkane-free trail. The drop velocity is size-independent, but increases linearly with both overheating and the thickness of the solid film (number of molecular layers melting). The droplet movement can be reversed. Under certain conditions (asymmetric force field = droplets in contact with solid alkane terraces of different height), below T_{mp} , the droplets move, leaving behind traces of solidified alkane layers. There are indications that in the case of solidifying running drops the terrace is present underneath the liquid while in the opposite case (melting-driven) not. The topologies and driving forces are discussed in some detail.

Based on the thermodynamic approach discussed in chapter 7 the experimentally observed hierarchy of melting mechanisms could be explained. The experimental results confirm for the first time a relation between overheating and wetting which has been suggested already a long time ago and

never proven. Usually solids can not be overheated because their melt wets its own solid and there is no nucleation barrier. The alkane melt is non-wetting, thus there is a barrier and overheating.

Figure 8.1 summarizes some findings of this work:

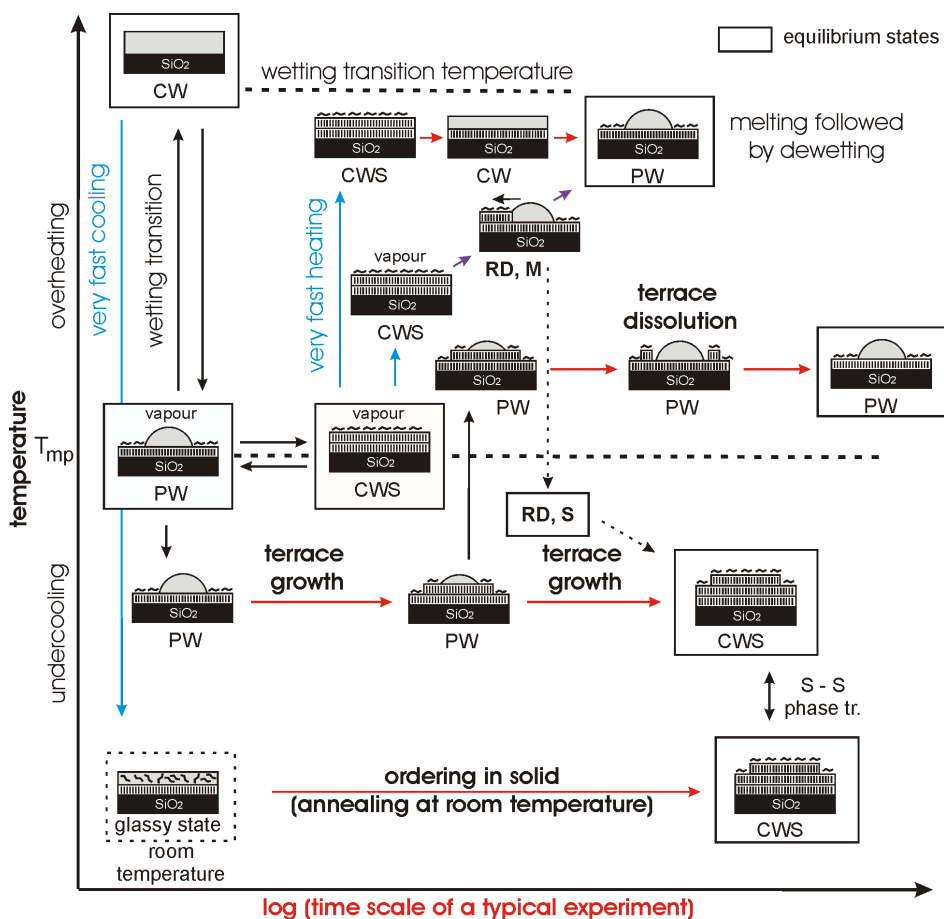


Figure 8.1. Schematic diagram showing the *thermodynamic states* (PW = partial wetting, CW = complete wetting, CWS = "completely wetting" solid) and some of the *melting/solidification mechanisms* (i.e. terrace growth – terrace dissolution, melting-/solidifying-driven "running droplets", MN = massive nucleation and growth of the liquid phase in a (overheated), molecularly thin alkane film) observed and analyzed in detail in this work. The system consists of long-chain alkanes (e.g. C₂₄, C₃₀ and C₃₆ at planar solid(SiO₂/vapor interface). The x coordinate denotes the log (typical time of a the experiment) and y the extent of undercooling/overheating.

Bibliography

- [1] H.-J. Butt, K. Graf, and M. Kappl. *Physics and Chemistry of Interfaces*. Wiley-VCH Verlag GmbH & Co. KGaA, Weinheim, 2003.
- [2] F. Brochard-Wyart, J. M. di Meglio, D. Quéré, and P. G. de Gennes. *Langmuir*, 7:335, 1991.
- [3] J. Israelachvili. *Intermolecular and surface forces*. Academic Press, London, 2nd edition, 1991.
- [4] B. V. Derjaguin, N. V. Churaev, and V. M. Muller. *Surface Forces*. Consultants Bureau, New York, 1987.
- [5] P. G. de Gennes, F. Brochard-Wyart, and D. Quéré. *Capillarity and Wetting Phenomena: Drops, Bubbles, Pearls, Waves*. Springer, New York, 2004.
- [6] J. F. Oliver and S. G. Mason. *J. Coll. Inter. Sci.*, 60:480, 1977.
- [7] R. Hoffman. *J. Colloid Interface Sci.*, 50:228, 1975.
- [8] L. H. Tanner. *J. Phys. D*, 12:1473, 1979.
- [9] P. G. de Gennes. *Rev. Mod Phys.*, 57:827, 1985.
- [10] R. G. Cox. *J. Fluid Mech.*, 168:169, 1986.
- [11] T. D. Blake and J. M. Haynes. *J. Coll. Inter. Sci.*, 30:421, 1969.
- [12] P. G. Petrov and J. G. Petrov. *Langmuir*, 8:1762, 1992.
- [13] T. C. Papanastasiou, G. C. Georgiou, and A. N. Alexandrou. *Viscous Fluid Flow*. CRC Press, London, 2000.
- [14] B. W. Cherry and C. M. Holmes. *J. Coll. Inter. Sci.*, 29:174, 1969.
- [15] W. V. Chang, Y. M. Chang, L. J. Wang, and Z. G. Wang. *Organic Coatings and Applied Polymer Science*. American Chemical Society, 1982.
- [16] W. D. Bascom, R. L. Cottington, and C. R. Singleterry. *Contact angle, Wettability, and Adhesion*. American Chemical Society, 1964.
- [17] A. Marmur and M. D. Lelah. *J. Coll. Inter. Sci.*, 78:262, 1980.
- [18] D. Ausserré, A. M. Picard, and L. Léger. *Phys. Rev. Lett.*, 57:2671, 1986.

- [19] W. Radigan, H. Ghiradella, H. L. Frisch, H. Schonhorn, and T. K. Kwei. *J. Colloid Interface Sci.*, 49:241, 1974.
- [20] H. Ghiradella, W. Radigan, and H. L. Frisch. *J. Coll. Inter. Sci.*, 51:522, 1975.
- [21] F. Heslot, N. Fraysse, and A. M. Cazabat. *Nature*, 338:640, 1989.
- [22] J. F. Joanny and P.G. de Gennes. *J. Phys. (Paris)*, 47:121, 1986.
- [23] F. Heslot, A. M. Cazabat, and P. Levinson. *Phys. Rev. Lett.*, 62:1286, 1989.
- [24] F. Heslot, A. M. Cazabat, and N. Fraysse. *J. Phys. Cond. Matter*, 1:5793, 1989.
- [25] F. Heslot, A. M. Cazabat, P. Levinson, and N. Fraysse. *Phys. Rev. Lett.*, 65:599, 1990.
- [26] R. Lucht and Ch. Bahr. 85:4080, 2000.
- [27] S.F. Burlatsky, J.G. Berberian, J. Shore, and W.P. Reinhardt. *Phys. Rev. E*, 54:1489, 1996.
- [28] J. Moon, S. Garoff, P. Wynblatt, and R. Suter. *Langmuir*, 20:402, 2004.
- [29] M.P. Valignat, N. Fraysse, A. M. Cazabat, P. Levinson, and M. Heslot, F. Cazabat. *Colloids and Surfaces A*, 83:193, 1994.
- [30] A. M. Cazabat, N. Fraysse, F. Heslot, P. Levinson, J. Marsh, F. Tiberg, and M. P. Valignat. *Adv. Colloid Interface Sci.*, 48:1, 1994.
- [31] P.G. de Gennes and A.M. Cazabat. *C. R. Acad. Sci. Paris, Ser. II*, 310:1601, 1990.
- [32] S.F. Burlatsky, G. Oshanin, A.M. Gazabat, and M. Moreau. *Phys. Rev. Lett.*, 76:86, 1996.
- [33] G. Oshanin, J. De Coninck, A.M. Cazabat, and M. Moreau. *Phys. Rev. E*, 58:R20, 1998.
- [34] J.A. Nieminen and T. Ala-Nissila. *Phys. Rev. E*, 49:4228, 1994.
- [35] S. Bekink, S. Karaborni, G. Verbist, and K. Esselink. *Phys. Rev. Lett.*, 76:3766, 1996.
- [36] D.B. Abraham, R. Cuerno, and E. Moro. *Phys. Rev. Lett.*, 88:206101–1, 2002.
- [37] E. Raphaël. *C.R. Acad. Sci. Paris IIB*, 306:751, 1988.
- [38] T. Ondarçuhu and M. Veyssié. *J. Phys. II France*, 1:75, 1991.
- [39] M. Chaudhury and G. M. Whitesides. *Science*, 256:1539, 1993.
- [40] S. Daniel, M. K. Chaudhury, and J. C. Chen. *Science*, 291:633, 2001.
- [41] W. Zisman. *Contact Angle, Wettability and Adhesion*,. Number 43. American Chemical Society, 1964.
- [42] C. Bain, G. Burnett-Hall, and R. Montgomerie. *Nature*, 372:414, 1994.
- [43] F. D. dos Santos and T. Ondarçuhu. *Phys. Rev. Lett.*, 75:2972, 1995.

- [44] D. W. Zheng, W. Wen, and K. N. Tu. *Phys. Rev. E*, 57:R3719, 1998.
- [45] A. K. Schmid. *Science*, 290:1561, 2000.
- [46] F. Brochard. *Langmuir*, 5:432, 1989.
- [47] D. M. Small. *The Physical Chemistry of Lipids: From Alkanes to Phospholipids*. Plenum Press, New York, 1986.
- [48] A. I. Kitaigorodskii. *Molecular Crystals and Molecules*. Academic Press, New York, 1973.
- [49] M. Dirand, M. Bouroukba, V. Chevallier, and D. Petitjean. *J. Chem. Eng. Data*, 47:115, 2002.
- [50] S. C. Nyburg and J. A. Potworowski. *Acta Crystallogr.*, B29:347, 1973.
- [51] E. B. Sirota and D. M. Singer. *J. Chem. Phys.*, 101:10873, 1994.
- [52] A. Müller. *Proc. R. Soc. London.*, A 138:514, 1932.
- [53] A. Craievich, J. Doucet, and I. Denicolo. *Phys. Rev. B*, 32:4164, 1985.
- [54] A. Craievich, I. Dinicolo, and J. Douchet. *Phys. Rev. B*, 30:4782, 1984.
- [55] J. Doucet, I. Denicolo, and A. Craievich. *J. Chem. Phys.*, 75:1523, 1981.
- [56] J. Doucet, I. Denicolo, A. Craievich, and A. Collet. *J. Chem. Phys.*, 75:5125, 1981.
- [57] I. Denicolo, J. Doucet, and A. Craievich. *J. Chem. Phys.*, 78:1465, 1983.
- [58] J. Doucet, I. Denicolo, A. Craievich, and C. Germain. *J. Chem. Phys.*, 80:1647, 1984.
- [59] G. Ungar. *J. Phys. Chem.*, 87:689, 1983.
- [60] G. Ungar and N. Masi. *J. Phys. Chem.*, 89:1036, 1985.
- [61] D. L. Dorset, B. Moss, J. C. Wittmann, and B. Lotz. *Proc. Natl. Acad. Sci.*, 81:1913, 1984.
- [62] D. L. Dorset. *EMSA Bull.*, 20:54, 1990.
- [63] D. L. Dorset, H.L. Hu, and J. Jager. *Acta Crystallogr. A*, 47:543, 1991.
- [64] E. B. Sirota, Jr H. E. King, D. M. Singer, and H. H. Shao. *J. Chem. Phys.*, 98:5809, 1993.
- [65] E. B. Sirota, D. M. Singer, and Jr H. E. King. *J. Chem. Phys.*, 100:1542, 1994.
- [66] E. B. Sirota, Jr H. E. King, H. H. Shao, and D. M. Singer. *J. Phys. Chem.*, 99:798, 1995.
- [67] J.C. Ernschaw and C.J. Hughes. *Phys. Rev. A*, A 46:R4494, 1992.
- [68] C. Merkl, T. Pfohl, and H. Riegler. *Phys. Rev. Lett.*, 79:4625, 1997.
- [69] A. V. Tkachenko and Y. Rabin. *Phys. Rev. Lett.*, 97:351, 1997.

- [70] R. W. Cahn. *Nature(London)*, 413:582, 2001.
- [71] J. G. Dash. *Rev. Mod. Phys.*, 71:1737, 1999.
- [72] Z. H. Jin, P. Gumbsch, K. Lu, and E. Ma. *Phys. Rev. Lett.*, 87:055703–1, 2001.
- [73] F. A. Lindemann. *Z. Phys.*, 11:609, 1910.
- [74] M. Born. *J. Chem. Phys.*, 7:591, 1939.
- [75] G. Tammann. *Z. Phys. Chem., Stoechiom. Verwandtschaftsl.*, 68:205, 1910.
- [76] B. Pluis, A. W. denier van der Gon, J. W. M. Frenken, and J. F. van der Veen. *Phys. Rev. Lett.*, 59:2678, 1987.
- [77] D.-M. Zhu and J. G. Dash. *Phys. Rev. Lett.*, 57:2959, 1986.
- [78] J. W. M. Frenken and J. F. van der Veen. *Phys. Rev. Lett.*, 54:134, 1985.
- [79] J. Daeges, H. Gleiter, and J. H. Perepezko. *Phys. Lett. A*, 119:79, 1986.
- [80] F. Banhart, E. Hernández, and M. Terrones. *Phys. Rev. Lett.*, 90:185502–1, 2003.
- [81] S.-N. Luo and D. C. Swift. *Phys. Rev. Lett.*, 92:139601–1, 2004.
- [82] K. K. Nanda, S. N. Sahu, and S. N. Behera. *Phys. Rev. A*, 66:013208–1, 2002.
- [83] F. G. Shi. *J. Matter Res.*, 9:1307, 1994.
- [84] Q. Jiang, L.H. Liang, and J. C. Li. *Vacuum*, 72:249, 2004.
- [85] P. Müller and R. Kern. *Surf. Sci.*, 529:59, 2003.
- [86] M. Tolan and W. Press. *Z. Kristallogr.*, 213:319, 1998.
- [87] J. Daillant and A. Gibaud. *X-ray and neutron reflectivity: principles and applications*. Springer, Berlin, 1999.
- [88] L. G. Parratt. *Phys. Rev.*, 1954.
- [89] G. Binning, C. F. Quate, and C. Gerber. *Phys. Rev. Lett.*, 56:930, 1986.
- [90] Hartmann U. *Ultramicroscopy*, 42:59, 1992.
- [91] W. Kern. *RCA Engineer*, 28, 1983.
- [92] W. Kern. *Semiconductor International*, 94, 1984.
- [93] B. F. Philips. *J. Vac. Sci. Technol.*, A1, 1983.
- [94] K. Graf and H. Riegler. *Colloid Surface, A* 131:215, 1998.
- [95] T.P. Russell. *Materials Science Reports*, 5:171, 1990.

- [96] H. Mo, H. Taub, U. G. Volkman, M. Pino, S. N. Ehrlich, F. Y. Hansen, E. Lu, and P. Miceli. *Chem. Phys. Lett.*, 377:99, 2003.
- [97] U. G. Volkman, M. Pino, and L. A. Altamirano. *J. Chem. Phys.*, 116:2107, 2002.
- [98] R. Köhler. *Personal Communication*.
- [99] H. Gau, S. Herminghaus, P. Lenz, and R. Lipowsky. *Science*, 283:46, 1999.
- [100] X. Z. Wu, B. M. Ocko, E. B. Sirota, S. K. Sinha, M. Deutsch, B. H. Cao, and M. W. Kim. *Science*, 261:1018, 1993.
- [101] A. J. Queimada, S. E. Quiñones Cisneros, I.M. Marrucho, J. A. P. Coutinho, and E. H. Stenby. *Int. J. Thermophys.*, 24, 2003.
- [102] B. M. Ocko, X. Z. Wu, E. B. Sirota, S. K. Sinha, O. Gang, and M. Deutsch. *Phys. Rev. E*, 55:3164, 1997.
- [103] M. Born and E. Wolf. *Principles of Optics*. Pergamon, Oxford, 1993.

A. Appendix

A.1. Definitions

Table A.1. List of some of the symbols used in this work.

Symbol	Meaning	Symbol	Meaning
R	radius of a circular wetting line	ν	mole number
r	spherical cap radius	m	mass (of a drop)
V	(spherical cap) volume	$\Xi(\theta)$	conversion function, $V \equiv \Xi(\theta)R^3$
A	surface area	h	height of the spherical cap / thickness
θ	contact angle	x	in-plane position, horizontal displacement
ρ_L (ρ_S)	liquid (solid) densities	H_0	monolayer thickness
N	number of molecular layers	H	film thickness

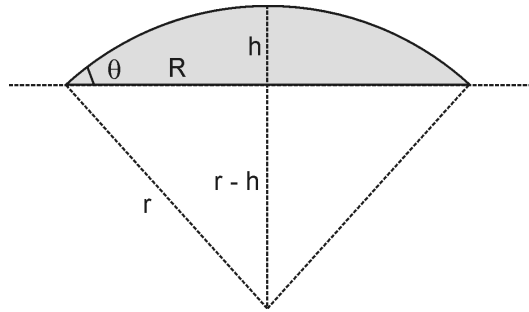


Figure A.1. Parametrization of a spherical cap drop.

A.1.1. Useful relations between different parameters describing spherical-cap shaped drops

Spherical cap volume as function of different parameters:

$$V(h, R) = \frac{\pi}{6}h(3R^2 + h^2) \quad (\text{A.1})$$

$$V(r, \theta) = \frac{\pi}{3}r^3(1 - \cos \theta)^2(2 + \cos \theta) \quad (\text{A.2})$$

$$V(R, \theta) = \frac{\pi}{3 \sin^3 \theta}R^3(1 - \cos \theta)^2(2 + \cos \theta) \quad (\text{A.3})$$

The parameter Ξ is defined by:

$$V(\Xi, R) \equiv \Xi R^3 \quad (\text{A.4})$$

Relation between Ξ and θ :

$$\Xi(\theta) = \frac{\pi}{6} \left[\frac{3}{\tan(\frac{\pi}{2} - \frac{\theta}{2})} + \frac{1}{\tan^3(\frac{\pi}{2} - \frac{\theta}{2})} \right] \quad (\text{A.5})$$

The inverse function, $\theta(\Xi)$ can be calculated by using the notation $x \equiv [\tan(\frac{\pi}{2} - \frac{\theta}{2})]^{-1}$ and solving the resulting third-order equation,

$$x^3 + 3x - \frac{6\Xi}{\pi} = 0 \quad (\text{A.6})$$

The (real) solution is

$$x_0 = - \left(\sqrt[3]{\frac{-3\Xi}{\pi} + \sqrt{1 + \frac{9\Xi^2}{\pi^2}}} + \sqrt[3]{\frac{-3\Xi}{\pi} - \sqrt{1 + \frac{9\Xi^2}{\pi^2}}} \right) \quad (\text{A.7})$$

$$\theta(\Xi) = \pi - 2 \arctan(x_0^{-1}) \quad (\text{A.8})$$

Interfacial surface area of a spherical-cap shaped drop

$$A_{SL} = \pi R^2 \quad (\text{A.9})$$

$$A_{LV} = 2\pi r^2(1 - \cos \theta) = 2\pi R^2 \left(\frac{1 - \cos \theta}{\sin^2 \theta} \right) \quad (\text{A.10})$$

A.2. Fresnel reflectivity

The reflected amplitude is obtained by writing down the boundary conditions at the interface, i.e., the continuity of the electric and magnetic fields at the interface. This leads to the classical Fresnel relations.

Let us consider an electromagnetic plane wave propagating in the xz plane of incidence, with its electric field polarized normal to this plane along the y direction. The interface between air and the reflecting medium which is located at $z = 0$ (as shown in figure A.2) will be assumed ideally smooth and sharp.

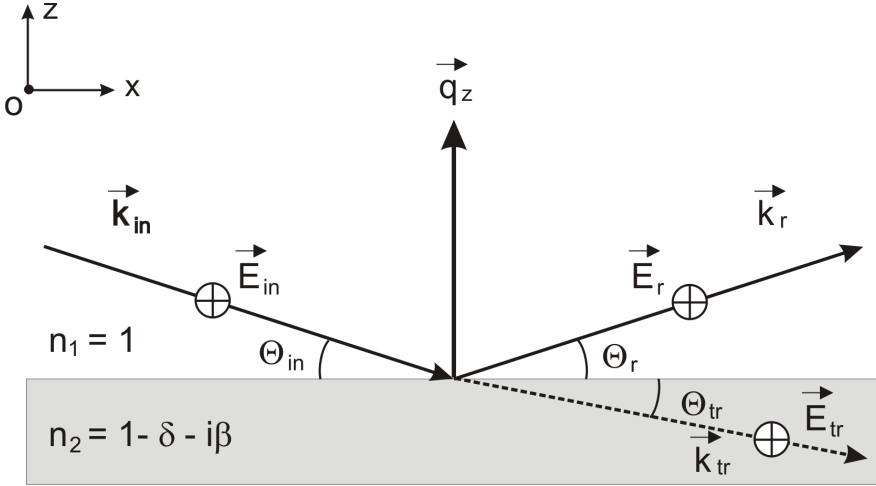


Figure A.2. Reflection and refraction of an incident wave polarized along y and traveling in the xz plane of incidence. $\theta_{in} = \theta_r = \theta$ and $\mathbf{q} = \mathbf{k}_r - \mathbf{k}_{in} = q_z$ (specular reflection).

By combining the expressions derived from Maxwell's equations for the electric field in a homogeneous medium, one can get the propagation equation of the electric field known as Helmholtz's equation:

$$\Delta \mathbf{E}(\mathbf{r}) + k_j^2 \mathbf{E}(\mathbf{r}) = 0, \quad (\text{A.11})$$

where $k_j = 2\pi/\lambda$ represents the wave vector \mathbf{k}_j in medium j . The electric field which is the solution of Helmholtz's equation is given for the incident (in), reflected (r) and transmitted (tr) plane waves by,

$$\mathbf{E}_j = A_j e^{i(\omega t - \mathbf{k}_j \cdot \mathbf{r})} \mathbf{e}_y \quad (\text{A.12})$$

with $j = \text{in, r or tr}$, $|\mathbf{k}_{in}| = |\mathbf{k}_r| = k_0 = 2\pi/\lambda$, $|\mathbf{k}_{tr}| = n_2 k_0$, and \mathbf{e}_y is the unit vector along the y axis. The components of the (in), (r), and (tr) wave vector are

$$\mathbf{E}_j = E_{0,j} e^{i(\omega t - \mathbf{k}_j \cdot \mathbf{r})} \mathbf{e}_y \quad (\text{A.13})$$

$$\begin{aligned} \mathbf{k}_{in} &= k_0(\cos \theta_{in}, 0, -\sin \theta_{in}) \\ \mathbf{k}_r &= k_0(\cos \theta_{in}, 0, +\sin \theta_{in}) \\ \mathbf{k}_{tr} &= k_0 n_2(\cos \theta_{tr}, 0, -\sin \theta_{tr}) \end{aligned} \quad (\text{A.14})$$

From the continuity of electric and magnetic fields at the interface (non-magnetic media) one gets the following relations between A_{in} , A_r and A_{tr} [87, 103],

$$A_{in} + A_r = A_{tr} \quad (\text{A.15})$$

$$(A_{in} - A_r) \sin \theta_{in} = n_2 A_{tr} \sin \theta_{tr} \quad (\text{A.16})$$

Defining the reflection coefficient, r , as A_r/A_{in} and the transmission coefficient, t , as A_{tr}/A_{in} and combining the two equations above, the reflection coefficients for (s) polarisation is found to be,

$$r_s = \frac{\sin \theta_{in} - n_2 \sin \theta_{tr}}{\sin \theta_{in} + n_2 \sin \theta_{tr}} \quad (\text{A.17})$$

For (p) polarisation, a similar calculation leads to,

$$r_s = \frac{n_2^2 \sin \theta_{in} - n_2 \sin \theta_{tr}}{n_2^2 \sin \theta_{in} + n_2 \sin \theta_{tr}} \quad (\text{A.18})$$

The relations above, (A.17) and (A.18), are known as Fresnel equations. Since n_2 is very close to unity, there is practically no difference between the (s) and (p) polarizations ($r_p \approx r_s \approx r$). Only (s) polarisation will be considered in the following.

Applying the Snell-Decartes' law, equation (3.4), and considering the approximations for the small incidence angles, $\cos \theta \approx 1 - \theta^2/2$, $n_2^2 \approx 1 - 2\delta \approx 1 - \theta_c^2$, equation (A.17) becomes,

$$r(\theta) = \frac{\theta - \sqrt{\theta^2 - \theta_c^2}}{\theta + \sqrt{\theta^2 - \theta_c^2}} \quad (\text{A.19})$$

The reflectivity which is the square of the modulus of the reflection coefficient, is given by,

$$R(\theta) = rr^* = \left| \frac{\theta - \sqrt{\theta^2 - \theta_c^2}}{\theta + \sqrt{\theta^2 - \theta_c^2}} \right|^2 \quad (\text{A.20})$$

Below the critical angle, the reflectivity is unity (incident radiation is completely reflected by the interface). A steep decrease of R occurs when $q = q_c$. When the wave-vector transfer is very large compared to q_c , i. e. $q \gtrsim 3q_c$, the following asymptotic behaviour is observed:

$$R = \frac{q_c^4}{16q^4} \quad (\text{A.21})$$

Rough interfaces considerably damp the specularly reflected intensity [86]. The missing intensity is diffusely scattered at exit angles $\theta_r \neq \theta_{in}$. Corrections of the specular scattering which take into account a continuous profile rather than a sharp interface are quite simple, at least for statistically rough interfaces with Gaussian height distribution. By introducing the height function $h(x,y)$, which describes the height of a point at a lateral location (x,y) with respect to the mean vertical position of the interface, it is possible to calculate the density profile $\rho(z)$ from its projection to the surface normal. Thus, for a rough interface, instead of a jump in the refractive index, a continuous variation must be considered.

The transition from a step-profile to a continuous function can be used to describe the transition from a perfect crystal with fixed atoms to a crystal with thermal motion. For phonons this is described in the harmonic approximation by a Debye-Waller factor. In the Born approximation, the Fresnel reflectivity R_F^{rough} of a rough interface with Gaussian height distribution is damped by a Debye-Waller factor too

$$R_F^{rough}(q_z) = R_F(q_z)e^{-q_z^2\sigma^2} \quad (\text{A.22})$$

where σ is the rms-roughness of the interface.

A.3. Home-made equipment, special set-up

The temperature controller, the heating stage and the temperature acquisition

For heating the samples under the optical microscope a home-made heating stage based on a Peltier element was designed and build. The temperature was controlled by a digital temperature controller (MR13, Shimaden Co. Japan).

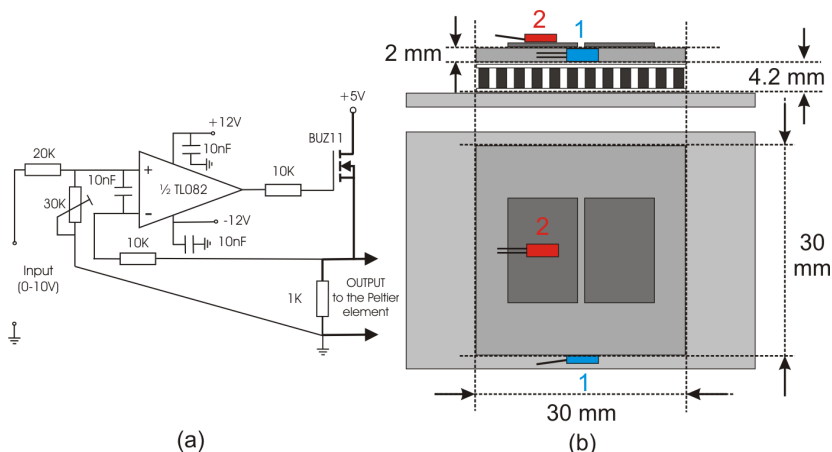


Figure A.3. The power stage electronics (a) and the heating stage based on a Peltier element (b); the two positions of the tiny temperature sensor are labeled 1 (lateral) and 2 (on top of the sample).

The output from the controller (0-10V) was used to drive a power stage presented in figure A.3, (a) whose output (0-5V, max. 5A) was connected to the Peltier element. Part (b) of the figure shows schematically the heating-stage with the two positions where tiny temperature sensors (Pt100 or Pt1000) were mounted: position 1 - glued with epoxy resin on top of a silicon wafer which was thermally connected with silicon oil to the metallic plate, simulating a real sample and position 2 - glued laterally on the aluminium plate. The temperature signal for the control loop was given by the temperature sensor mounted laterally (position 1). The "running drop" experiments required temperature ramps (heating rate in the range 0.3 to 0.8°C/s) and continuous temperature recording. For this purpose, in addition to the first temperature sensor (control loop, position 1), a second temperature sensor (Pt100 or Pt1000, either in position 1 or 2) connected via a proper amplifier to a data logger (Pico Technology Ltd., 10 bit) was used to record the temperature-time dependence. The temperature ramp was generated by a sudden change of the set temperature from typically 1–3°C below the alkane bulk melting point to 10° above it. This is equivalent to a constant power applied to the heater which corresponds to a constant heating rate within the small temperature range of interest (0 to 1°C overheating).

Stroboscopic illumination for optical microscopy

Some experiments required a stroboscopic illumination of the sample under the optical microscope. For this purpose, well-defined light pulses were generated with the set-up shown in figure A.4.

A pulse-shaped electric signal (a), from a function generator (AFG310, Sony-Tektronix) was driving a home-made current amplifier (b), which supplies a power LED (type LXHL-NW98, 180 Cd,

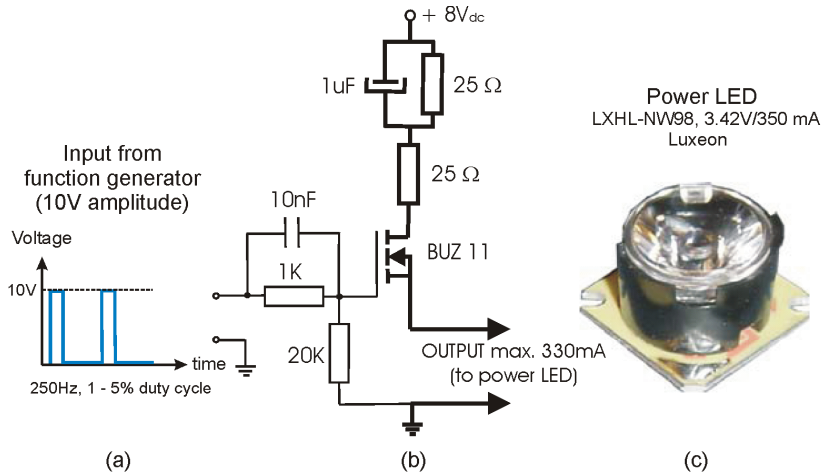


Figure A.4. Stroboscopic set-up: the electric signal (a) generated by the function generator drives the current amplifier (b) which supplies the power for the LED (c). The LED was mounted on the microscope instead of the original light source, using a mechanical adapter (not shown).

3.42V/350 mA, Luxeon, (c)). The electrical signal parameters were typically $10V_{pp}$ amplitude, 250 Hz frequency and 1 to 5% duty cycle. The LED was mounted on the optical microscope via a mechanical adapter, replacing the original light source.

A.4. Mechanism-dependent equations describing the growth kinetics of a thin solid film

A spherical-cap shaped liquid droplet creating a molecularly thin solid terrace by spreading onto a solid surface can be analyzed by recording the time evolution of three parameters, the in-plane radius of the central droplet, $R_1(t)$, and the terrace radius, $R_2(t)$, and the contact angle, $\theta(t)$, (see figure A.5).

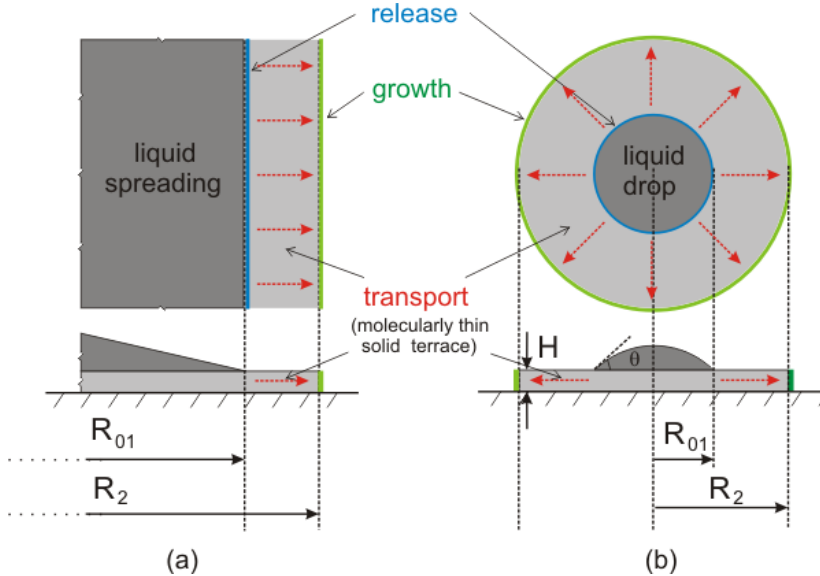


Figure A.5. Linear (a) and circular (b) spreading geometries (droplet not to scale).

For isothermal conditions the contact angle is constant and the central liquid droplet is completely described by $R_1(t)$ and θ . A further simplification is to consider the case of large droplets for which the amount of alkane in the spreading terrace is negligible compared to the amount of alkane in the central droplet and therefore $R_1(t) \approx R_{01}$, the initial value of the droplet in-plane radius. Under these considerations, the spreading can be described by a single variable $R_2(t)$ and two constants, θ and R_{01} .

In analogy with chemical reactions, the spreading kinetics can be analyzed in terms of speed-limiting steps. Thus, three steps can be considered: (i) the release of the molecules from the central drop, (ii) the transport of matter from the contact line to the growing front and (iii) the growth at the edge (front). In the following, the time evolution of the spreading process is discussed for two geometries (circular and linear) and three possible speed-limiting steps.

A.4.1. Release-limited, constant mass flux per unit length of contact line

Linear geometry

For linear geometry, a constant release rate per unit contact line length, j_R leads to the following front velocity

$$\frac{\partial R_2}{\partial t} = \frac{j_R}{\rho_S H} \quad (\text{A.23})$$

where j_R is the mass flux (amount released per unit length of the contact line), H is the thickness of the terrace and ρ_S is the solid alkane density in the terrace. Integrating the equation above gives the linear dependence of R_2 vs. time:

$$R_2(t) - R_{01} = \frac{j_R}{\rho_S H} t \quad (\text{A.24})$$

Circular geometry

The same consideration applied to a circular geometry gives

$$\frac{\partial R_2}{\partial t} = \frac{2\pi R_1 j_R}{R_2 \rho_S H} \quad (\text{A.25})$$

which becomes after integration

$$R_2^2(t) = R_{01}^2 + \frac{4\pi R_1 j_R}{\rho_S H} t \quad (\text{A.26})$$

A.4.2. Growth-limited, constant rate of solidification at the edge

If the speed-limiting step is the growth process at the terrace edge, the (geometry independent) kinetics is described by the same equations as in the case of release-limited, linear geometry, A.23 and A.24. The only difference is that j_R , the release rate per unit length, is replaced by the growth rate per unit length, j_G .

A.4.3. Transport-limited, "diffusion-like" transport

Spreading kinetics can be controlled by the transport process. It may, for instance, be diffusive. Fick's first law can be used to calculate the time dependence of R_2 . Supposing that the alkane concentration varies from a constant value Γ_1 near the contact line, to another constant value Γ_2 ($\Gamma_2 < \Gamma_1$) at the growing front, this causes a concentration gradient which drives the transport. This assumption is reasonable if the temperature is constant and the local concentration values at the contact line and the growth front, respectively, are the result of two fast dynamic equilibria which are barely influenced by the local amount of matter per unit time being taken from the contact line or coming to the growing edge. According to Fick's first law, the diffusive mass flux per unit length, j_D in any position between the contact line and the edge is

$$j_D = -D \frac{\partial \Gamma}{\partial R} \quad (\text{A.27})$$

where D is the diffusion coefficient in two dimensions, and $\Gamma(R,t)$ is the surface concentration of the liquid alkane in grams per unit surface area.

Linear geometry

The diffusional growth rate for linear geometry is proportional to the concentration gradient. Continuity considerations (steady-state) imply that the gradient $\partial \Gamma / \partial R$ is constant (i.e. $\partial^2 \Gamma / \partial^2 R = 0$)

everywhere between the contact line and the growing front at any moment of spreading. Thus, the front velocity is given by

$$\frac{\partial R_2}{\partial t} = -D \left(\frac{\partial \Gamma}{\partial R} \right) \frac{1}{H\rho_S} = -D \left(\frac{\Gamma_2 - \Gamma_1}{R_2 - R_{01}} \right) \frac{1}{H\rho_S} \quad (\text{A.28})$$

After integration, the following time dependence is obtained

$$(R_2 - R_{01})^2 = -2D \frac{(\Gamma_2 - \Gamma_1)}{H\rho_S} t = 2Dkt \quad (\text{A.29})$$

with the parameter $k \equiv (\Gamma_1 - \Gamma_2)/H\rho_S$ assumed constant for a given temperature and terrace thickness.

Circular geometry

The concentration gradient in case of circular geometry depends on position. The concentration profile $\Gamma(R)$ from R_{01} to R_2 , is needed in order to calculate the diffusional flux supplying the growing edge. Making use of the equation of continuity, i.e. the total amount of alkane passing through an arbitrary circle with the radius r ($R_{01} < r < R_2$) per unit time does not depend on position, one can write

$$J_D = 2\pi r j_D = -2\pi r D \frac{\partial \Gamma}{\partial r} \quad (\text{A.30})$$

Integrating the equation above gives the expression of total flux J_D

$$J_D = -2\pi D \frac{\Gamma_2 - \Gamma_1}{\ln(R_2/R_{01})} \quad (\text{A.31})$$

On the other hand, the total flux J_D is related to the velocity of the growing edge by

$$J_D = 2\pi\rho_S H R_2 \frac{\partial R_2}{\partial t} \quad (\text{A.32})$$

The equality of the two fluxes leads to a differential relation between R_2 and t . By integration, one obtains:

$$R_{01}^2 \left[\frac{R_2^2}{2R_{01}^2} \left(\ln \frac{R_2}{R_{01}} - \frac{1}{2} \right) + \frac{1}{4} \right] = Dt \frac{(\Gamma_1 - \Gamma_2)}{H\rho_S} \quad (\text{A.33})$$

The left side of the above equation is a function of R_{01} and R_2 having a linear dependence versus time. Taking into account the k parameter defined in the equation A.29 this relation can be rewritten as

$$Y(R_{01}, R_2) = \frac{R_2^2}{2} \left(2 \ln \frac{R_2}{R_{01}} - 1 \right) + \frac{R_{01}^2}{2} = 2Dtk \quad (\text{A.34})$$

If the difference $R_2 - R_{01} \equiv \varepsilon \ll R_{01}$, the $\ln(R_2/R_{01})$ can be approximated by $\varepsilon/R_{01} - \varepsilon^2/(2R_{01}^2)$ (the first three terms of the Taylor expansion). This leads to the following expression for $Y(R_{01}, R_2)$

$$Y(R_{01}, R_2)_{\varepsilon \ll R_{01}} \approx \varepsilon^2 - \frac{\varepsilon^4}{2R_{01}^2} \approx \varepsilon^2 \quad (\text{A.35})$$

meaning that we recover the diffusional time dependence for linear geometry, $(R_2 - R_{01})^2 \propto \text{time}$ (see equation A.29). In figure A.6 are plotted the three possible time dependencies of R_2 , having as reference a linear dependence of Y (i. e. the ideal case - diffusional transport, circular geometry). In conclusion, the Y function can be well approximated by $(R_2 - R_{01})^2$ if the ratio R_2/R_{01} is not much larger than 1.

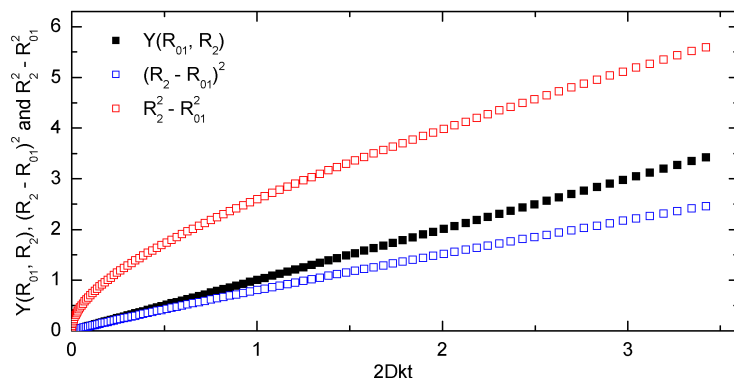


Figure A.6. $(R_2 - R_{01})^2$, $Y(R_{01}, R_2)$ and $R_2^2 - R_{01}^2$ functions vs. time, for the ratio R_2/R_{01} in the range of 1 to 2.57. One can observe that, at short times, the function $(R_2 - R_{01})^2$ is a very good approximation of the ideal function $Y(R_{01}, R_2)$ and that $R_2^2 - R_{01}^2$ function has non-linear time dependency.

A.5. Free energy gain upon spontaneous dewetting

The Gibbs free energy cost per unit area Δg^{CW} associated to the change of the wetting state from partially wetting drops (PW) to an uniform, completely wetting film (CW) is the negative of the free energy gain upon spontaneous dewetting,

$$\Delta g^{CW} = -\Delta g^{DW}. \quad (\text{A.36})$$

The value of Δg^{DW} depends on the initial thickness H (see figure A.7) and on the size of partially wetting drops¹ resulting from the dewetting process and the equilibrium contact angle, θ . Let us consider that all the (spherical-cap shaped) partially wetting drops which result from dewetting have the same size R (the radius of their circular three phase line). Further on, we assume that the surface area from which one drop collects the material upon dewetting is A . One can calculate the Δg_{DW}

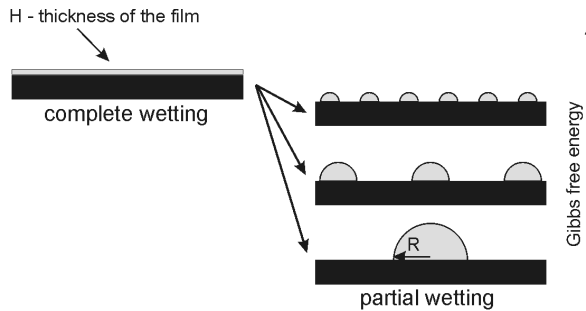


Figure A.7. Schematic representation of a spontaneous dewetting process. The associated Gibbs free energy gain depends on the thickness H of the completely wetting film and the size R of the drops resulting from the process.

from the difference between the surface free energy of the equilibrium state (partial wetting) and the surface free energy of the completely wetting film:

$$\Delta g^{DW} = \frac{1}{A} \left[(A - \pi R^2) \gamma_{SV} + \pi R^2 \gamma_{SL} + 2\pi R^2 \frac{(1 - \cos \theta)}{\sin^2 \theta} \gamma_{LV} - A \gamma_{LV} - A \gamma_{SL} \right] \quad (\text{A.37})$$

The first three terms are the surface free energies of the S/V, S/L and L/V interfaces, respectively, and the last two describe the completely wetting film. Considering the Young equation, $\gamma_{SV} = \gamma_{SL} - \gamma_{LV} \cos \theta$, the equation above becomes:

$$\Delta g^{DW} = \frac{1}{A} \left[(A - \pi R^2) \cos \theta - A + \frac{2\pi R^2}{\sin^2 \theta} (1 - \cos \theta) \right] \gamma_{LV}. \quad (\text{A.38})$$

Volume conservation gives the relation between A and R :

$$AH = \Xi(\theta) R^3, \quad (\text{A.39})$$

with $\Xi(\theta)$ the coefficient converting R^3 into the volume of the spherical cap. Combining A.38 and A.39 we get:

¹Or equivalently, their number per unit area

$$\Delta g^{DW} = \left[\left(1 - \frac{\pi H}{\Xi(\theta)R} \right) \cos \theta - 1 + \frac{2\pi H}{\Xi(\theta)R} \left(\frac{1 - \cos \theta}{\sin^2 \theta} \right) \right] \gamma_{LV}. \quad (\text{A.40})$$

In the particular case of a liquid film of C₃₀ with a coverage corresponding to one up-right solid monolayer the thickness H (of the liquid film) is ≈ 4.6 nm. Considering a typical size R of a partially wetting drop of ≈ 5 μm , a contact angle of 20° and $\gamma_{LV} \approx 28.6$ mJ/m², the value of the ratio $\pi H/(\Xi R)$ is ≈ 0.01 . Hence, the value of the dewetting free energy can be approximated as

$$\Delta g^{DW} \approx (\cos \theta - 1) \gamma_{LV} \quad (\text{A.41})$$

and has, for the considered case the value of -1.72 mJ/m² (the relative deviation from the exact value is smaller than $+1.6\%$).

A.6. Instability of a droplet wetting the step region

Let us consider a solid substrate consisting of two semi-infinite horizontal solid surfaces separated by a step of height H . We analyze the stability of a tiny drop (smaller than the capillary length) which covers the step region wetting a finite area of both terraces and the vertical step facet. In terms of wetting properties, the horizontal surfaces are partially wetted by the liquid giving the same equilibrium contact angle θ_e whereas the vertical wall is completely wetted. The lateral view of such a geometry is shown schematically in figure A.8, (a). For simplicity, we consider that the liquid shape is a ridge (1D problem), having in section a circular shape of the L/V interface (minimization of interfacial energies at constant volume). For reasons which will become clear later, the two contact angles are denoted as θ_R in the rear part of the drop (left side) and θ_F in the front (right side).

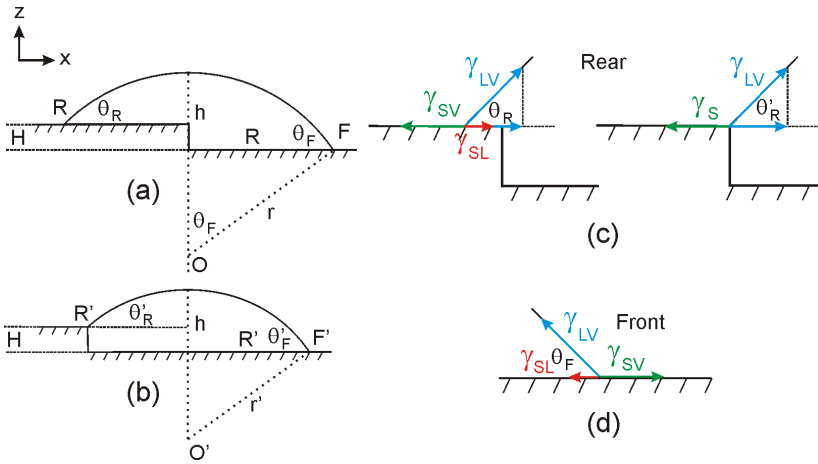


Figure A.8. Ridge wetting the step region between two horizontal terraces at different z positions: (a) initial configuration, (b) final state, (c) and (d) forces acting at the rear and front contact lines, respectively.

This configuration can be stable only if the two angles correspond to their equilibrium values according to Young equation ($\theta_R = \theta_F = \theta_e$) and the shape of L/V interface is circular (i.e. no Laplace pressure gradient within the liquid drop). These two conditions can not be *both* fulfilled due to the height difference between the two terraces. As a result, the droplet will move towards the lower terrace (right).

We find the direction of movement by considering the following initial geometry: (i) circular-shaped L-V interface and (ii) one of the angles takes its equilibrium value. For instance, if $\theta_F = \theta_e$, θ_R will be smaller than θ_e generating an *unbalanced Young force* at the rear contact line of the droplet. This force points towards right, the positive direction of x axis. As a result of the unbalanced Young force, the droplet will move and the two contact angles will take their dynamic values. For small velocities, the shape of the L/V interface will preserve its circular shape (same Laplace pressure within the liquid) and, if the step height H is much smaller than the droplet height h , the angle $\theta_{F,d}$ will be slightly larger and $\theta_{R,d}$ slightly smaller than θ_e . The deviations of the two values from θ_e will result from the condition of equal velocities of the two contact lines, $U_F = U_R$ ². Hence, at each

²This condition is not entirely correct because, on movement, the radius of the circle describing the L/V interface decreases as a result of the solid volume which leaves the control area defined by the circle of radius r .

contact line, the driving force will be balanced by the viscous dissipation:

$$\gamma_{LV}(\cos \theta_{R,d} - \cos \theta_e) = 3\eta L \frac{U_R}{\tan \theta_{B,d}} \quad (\text{A.42})$$

$$\gamma_{LV}(\cos \theta_e - \cos \theta_{F,d}) = 3\eta L \frac{U_F}{\tan \theta_{F,d}} \quad (\text{A.43})$$

Combining the two equations and considering $U_F = U_R$, we get

$$\tan \theta_{R,d}(\cos \theta_{R,d} - \cos \theta_e) = \tan \theta_{F,d}(\cos \theta_e - \cos \theta_{F,d}) \quad (\text{A.44})$$

For small values of the contact angles, the previous equation becomes:

$$\theta_{R,d}(\theta_e^2 - \theta_{R,d}^2) = \theta_{F,d}(\theta_{F,d}^2 - \theta_e^2). \quad (\text{A.45})$$

On the other hand, due to the circular geometry, the values of the two dynamic angles obey the following equations:

$$h = R \tan \frac{\theta_{F,d}}{2} \quad (\text{A.46})$$

$$h - H = R \tan \frac{\theta_{R,d}}{2}. \quad (\text{A.47})$$

Coming back to the most simple approach (i.e. to assume $\theta_F = \theta_e$, $\theta_R \neq \theta_e$) we are interested to estimate the magnitude of the unbalanced Young force (per unit length) which drives the drop towards the final state. In this case the two equations above become:

$$h = R \tan \frac{\theta_e}{2} \quad (\text{A.48})$$

$$h - H = R \tan \frac{\theta_R}{2}. \quad (\text{A.49})$$

Combining A.48 and A.49 we get:

$$\theta_R = 2 \arctan \left(\tan \frac{\theta_e}{2} - \frac{H}{R} \right) \quad (\text{A.50})$$

Considering the above equation, the force driving the drop towards right is

$$F_D(\gamma_{LV}, H, R) = \gamma_{LV} \left\{ \cos \left[\arctan \left(\tan \frac{\theta_e}{2} - \frac{H}{R} \right) \right] - \cos \theta_e \right\} \quad (\text{A.51})$$

The numerical value of F_D for $\gamma_{LV} = 28$ mN/m, $\theta_e = 20^\circ$, and $H = 150$ nm, and $R = 5$ μ m is ≈ 0.5 mN/m.

B. Acknowledgments

The work presented in this thesis was done at the Max Planck Institute of Colloid and Interfaces (Golm, Germany). I would like to express my gratitude to all people who have contributed to it.

Prof. Dr. Helmuth Möwald is gratefully acknowledged for the excellent working conditions and helpful scientific discussions, and for offering me the unique opportunity to work in the Department of Interfaces. Thank you for showing how a scientist should be, I still have a lot to learn from you.

I thank to my supervisor, Priv.- Doz. Dr. Hans Riegler, for our long scientific (and not only) discussions, for its positive criticism and rich ideas which helped me to go forward with this work. The discussions with you were always a bubble of oxygen which fueled the progress of this work and helped me to overcome many inherent problems and uncertainties.

This work had been financially supported by *Max-Planck International Research School on Biomimetics*. Dr. Angelo Valleriani, the Coordinator of the School, is gratefully acknowledged for the excellent organization, and for the interesting set of lectures which the School offered to the students.

My former colleague Dr. Hauke Schollmeyer introduced me in the field of X-ray scattering and AFM. Thanks for sharing your knowledge with me and for your patience.

Ralf Köhler, proved to be an excellent colleague and friend. I was really happy when he joined our group. He always succeeded to create an excellent working environment with his optimistic views. Thank you for everything.

I acknowledge Dr. Daniel Rapoport. Our discussions (for instance during the lectures about intermolecular forces) improved a lot my knowledge. You were a real "professor" to me.

Anneliese Heilig helped me with the AFM measurements. Thank you for your kindness and support. Many thanks to the MPI technical staff for their efficiency and kindness. In particular, because some experiments required special equipment, I would like to acknowledge Monika Scholz, Dipl. Ing. Wolfgang Stein, and Dipl. Ing. Henryk Pitas (Electronic shop) and Dipl. Ing. Günter Haseloff, Wolfgang Nierenz, and Andreas Kretschmar (Mechanic Shop) for being always ready to fulfil my imagination. For computer assistance, Ingo Fiedler and Michael Born are also gratefully acknowledged.

To my friends: Romeo and Beatrice Anghelache (*a proper mixture of coffee, cigarettes and science is always welcome, oder?*), Mihaela and Viorel Rusu (*n-am uitat că datorită vouă am ajuns în Germania, vă mulțumesc*), Sandra Rocha and Simone Calogero (*muito obrigado pela vossa amizade, ajuda e suporte*), Lucia Neure (*îți mulțumesc pentru incurajari*), Ana-Silvia Nița (*mulțumesc, m-ai ajutat când mi-a fost mai greu*), Ana Cordeiro (*obrigado por tudo*), Chrystelle Egger (*merci beaucoup*) and Narayan Mishra (*anek dhanyabad*). Many thanks also to: Liying Wang, Henning Kraß, Marc Schneider, Marc Nolte, Patrik Kölsch, and many others for being such a nice colleagues to me.

I thank Constanța Cacula for standing by me with patience, for her continuous encouragements and help (*então, consegue dormir agora?*). Last but not least "un Mulțumesc frumos" to my Mother and all my professors from Romania who contributed to my education, especially to Prof. Dr. Valerică Dumitrescu (University of Bucharest).